# Evolution of the Laurentide Ice Sheet in north-central Ontario from subglacial sediments

by

Robin Taves

A thesis
presented to the University of Waterloo
in fulfillment of the
thesis requirement for the degree of
Master of Science
in
Earth Sciences

Waterloo, Ontario, Canada, 2024

## Author’s Declaration

I hereby declare that I am the sole author of this thesis. This is a true copy of the thesis, including any required final revisions, as accepted by my examiners.

I understand that my thesis may be made electronically available to the public.

# Abstract

Reconstructing the Laurentide Ice Sheet's (LIS) evolution is essential to improve our understanding of the long-term behavior of ice sheets, and how they responded to past climate change and other Earth systems change around them. During the last glacial maximum (LGM), about 21 ka before present (BP), the Hudson and James Bay Lowlands (HJBL) was largely under the Quebec-Labrador (Q-L) Sector of the LIS. Northward movement of the Q-L Sector center caused a northwest ice flow direction to shift through to the southwest. The Albany Bay, Winisk, and James Bay Ice Streams were late-stage ice streaming events. The Albany and James Bay Ice Streams existed to the south and far east of the study area, whereas the Winisk Ice Stream (WIS) is central to the study area. The WIS extent has two components, a northern and southern. Its northern portion began at the Winisk River near the Hudson Bay coast and flowed south along the HJBL boundary. Multiple phases of ice flow with abundant sediment supply have resulted in extensive subglacial till units throughout the HJBL, which have become exposed along river incisions. Erosion and re-entrainment of pre-existing tills during production of new till typically leads to compositional blends. This thesis aims to reconstruct ice flow phases from the depositional record studied in an area centered over Ogoki Post to integrate into existing glacial frameworks to improve understanding of the evolution of subglacial environments during late LIS deglaciation and the WIS.

There is one interglacial sediment unit correlated to a regionally known interglacial bed (Fawn River and Webequie Sediments) and 6 till units identified using the analysis of sediment characteristics, till matrix geochemistry, clasts lithology counts, particle size analysis, and clast fabric measurements. Till 1 is a spatially limited but geochemically independent phase of till associated with either the Rocksands or earlier till phase that has since been weathered. Till 2 and 3 can be correlated to Sachigo and Severn Tills respectively (Thorleifson et al., 1993) and a late LIS ice flow phase. The Winisk Till in regional studies is observed as three phases in this study, recording a transitional till during early WIS development, through the main phase, to a local late surge with geochemical variation from the first and second WIS phase.

The three late LIS and three WIS tills can be correlated to regional studies with further distinction in the Winisk Till given its central location within the boundaries of the WIS. The presence of three pervasive till phases deposited across the HJBL during the LIS and up to three WIS phases locally highlights the complexity of the HBJL stratigraphic record and the local impacts of the WIS on material dispersal.

# Acknowledgements

This thesis contains information licensed under the federal Open Government License – Canada and provincial Open Government License – Ontario. This includes background data such as drainage, provincial boundaries, and national and provincial DEMs.

The research area is located within the territory of the Ogoki Post First Nation. The community is thanked for permitting access to the region.

Thank you Martin Ross for the guidance and wisdom throughout the many versions and years of this project. Dr. John Johnston and Dr. Sam Kelley are thanked for being my committee members and their contribution. An extended thank you to the Quaternary research group at the University of Waterloo and all the individuals who supported various stages. The larger HJBL Quaternary community is acknowledged for the knowledge sharing and symposiums through the years. And to Tyler Hodder of the Manitoba Geological Survey for sharing his insights into the HJBL.

De Beers Exploration Canada is thanked for both the field execution of the project and the in-kind support afterward, allowing me to take on this masters work in addition to my full-time duties. Of note are Charley Murphy and Natasha Oviatt. Thank you for the support, jokes, questions, and example you both set. Anglo American colleagues were also a huge support while I continued mastering during job changes, including the final wrap up while with my Teck Resources colleagues.

My family and friends - thank you for supporting me through schooling and life in the past 3+ years. You are my foundation when the house is shaking.

# Table of Contents

# List of Figures

# List of Tables

# Chapter 1. Introduction

## 1.1 Scientific Rationale

Reconstructing the evolution of the Laurentide Ice Sheet (LIS) is essential to improve our understanding of the long-term behavior of ice sheets and how they responded to past climate change. Reconstructions of the LIS largely rely on landform analysis and ice margin retreat history during the last deglaciation (Dyke et al., 2002; Batchelor et al., 2019; Dalton et al., 2020, 2023). Despite attempts to constrain the LIS prior to the last glacial maximum (LGM) (Dyke et al., 2002; Dalton et al., 2016; Chandler et al., 2018; Margold et al., 2018; Dalton et al., 2020, 2023) the pre-LGM ice flow phases remain poorly constrained, even more so for pre-Wisconsinian glaciations. Stratigraphic investigations that incorporate till composition studies are essential to constrain glacial dynamics in thick drift regions. One region of great interest for this type of research is the Hudson and James Bay lowlands (HJBL) due to its position in the interior of the LIS during the LGM. The HJBL is a vast wetland region located in far northern Ontario with peripheral regions extending into Quebec and Manitoba (**Figure 1**). It blankets approximately a quarter of Ontario at 250 000 $km^2$ with peat accumulation (muskeg) ranging in thickness from 1 m to more than 3 m (Riley, 2011). This extensive wetland cover limits access to Quaternary sediments, for both research and mineral exploration, to incised fluvial corridors. These fluvial corridors are geologically recent and likely do not represent all deglacial drainage paths meltwater would have used, especially during large meltwater drainage events (Harrison et al., 2018; Thorleifson, n.d.). Underneath the muskeg is a nearly continuous cover of unconsolidated, mostly glacial sediments from the late Quaternary Period with some inter and post glacial material.

During the last glacial maximum (LGM), about 21 ka before present (BP), the HJBL was largely under the Quebec-Labrador (Q-L) Sector of the Laurentide Ice Sheet (LIS). To the northwest is the Keewatin Sector, which had complex but limited influence to the far northwest HJBL as it flowed southward from a center in Nunavut (Dyke et al., 2002; Margold et al., 2018). The Q-L Sector was centered on the Quebec highlands and shifted northward after the LGM (Veillette et al., 1999; Clark et al., 2000). Northward movement of the Q-L ice center caused the initial northwest ice flow direction in the HJBL to shift through to a southwest direction (Dyke and Prest, 1987; Parent et al., 1995). In addition, there were three late-stage ice streaming events (**Figure 1**); from oldest to youngest they are the Albany Bay, Winisk, and James Bay Ice Streams (Veillette et al., 2017). The Albany Bay Ice Stream extended from James Bay to Lake

Superior passing north of the town of Hearst. The Winisk Ice Stream (WIS) extent and sediment dispersal patterns have been largely studied through landform interpretation (Thorleifson et al., 1993; Veillette et al., 2017) and has two components. Its main northern extent began at the Winisk River near the Hudson Bay coast and flowed south along the HJBL boundary. A gap in WIS landforms exists before it deflects to the east near the town of Hearst (Veillette et al., 2017). Then the final James Bay Ice Stream occurred down the modern James Bay depression, resulting in the late glacial Cochrane Surges. The Albany Bay Ice Stream and early WIS were inter-ice sheet ice streams while the late WIS and James Bay Ice Stream likely existed as ice margin ice streams as well.

The multiple generations of ice flow combined with high sediment supply have resulted in thick, discontinuous, stacked tills, which have become exposed along many river sections due to river incision caused by glacioisostasy and normal fluvial erosion (Skinner, 1973; Thorleifson et al., 1993; Dredge and McMartin, 2011; Riley, 2011; Dubé-Loubert et al., 2013; Veillette et al., 2017; Dalton et al., 2018). The till units have variable characteristics typically described using clast fabrics and clast lithology, matrix texture and colour, as well as matrix geochemistry. Erosion and re-entrainment of pre-existing tills during production of new till typically leads to compositional blends in the lower portion of till units (Thorleifson et al., 1993). In addition to blends due to till mixing, differences in bedrock geology along till transport path, as well as changes in shifting ice-flow directions introduce considerable variability in the composition of tills (Hodder et al., 2017). This includes lateral variations within the same till unit and stratigraphically through multiple till units. Nonetheless, methods exist to decipher these complexities and establish sediment provenance, which is needed to constrain ice flow history associated with the till stratigraphic record to improve ice sheet reconstructions and provide key insights into the subglacial conditions associated with different ice flows. This knowledge is critical for improving paleo-ice sheet models. To add to the complex glacial history and till stratigraphy, the region contains a sediment record deposited across multiple glaciations, which is evidenced by the presence of organic-bearing units within the stratigraphic record that were deposited during interstadials and/or interglacial periods that have been identified across the HJBL (Thorleifson et al., 1993; Dredge and McMartin, 2011; Dalton et al., 2018). This includes the Nelson and Gods River sediments in Manitoba (Dredge and McMartin, 2011; Dredge and Nielsen, 1985), the Fawn River Sediments in northern Ontario (Thorleifson et al., 1993), sediments along the Albany River in northeastern Ontario (Dalton et al., 2018), and the Friday Creek and Missinaibi sediments in southeastern Ontario (Skinner, 1973). The sediments have been interpreted to have been deposited in a variety of depositional environments including

fluvial, glaciofluvial, lacustrine and glaciolacustrine. Correlating, dating, and identifying new non-glacial sequences has been a challenge and continues to be an area of active research (Dalton et al., 2018, 2016; Gao et al., 2020; Hodder et al., 2023).

This thesis aims to reconstruct ice flow phases from the depositional record studied in an area centered over Ogoki Post (Marten Falls) to integrate into existing glacial frameworks to improve understanding of the evolution of subglacial environments during late LIS deglaciation.

Ogoki Post is located at the confluence of the Ogoki River into the Albany River in northern Ontario and is situated near the center of the WIS (**Figure 2**). Ogoki Post has an airport and winter road, but there is no permanent infrastructure outside of the community given consistent organic cover in proximity to the community extending ~40 km to the west. Logging roads extend well north of Nakina but cease at the edge of the HJBL. The Victor diamond mine is to the northeast and the Ring of Fire chrome deposit is to the north.

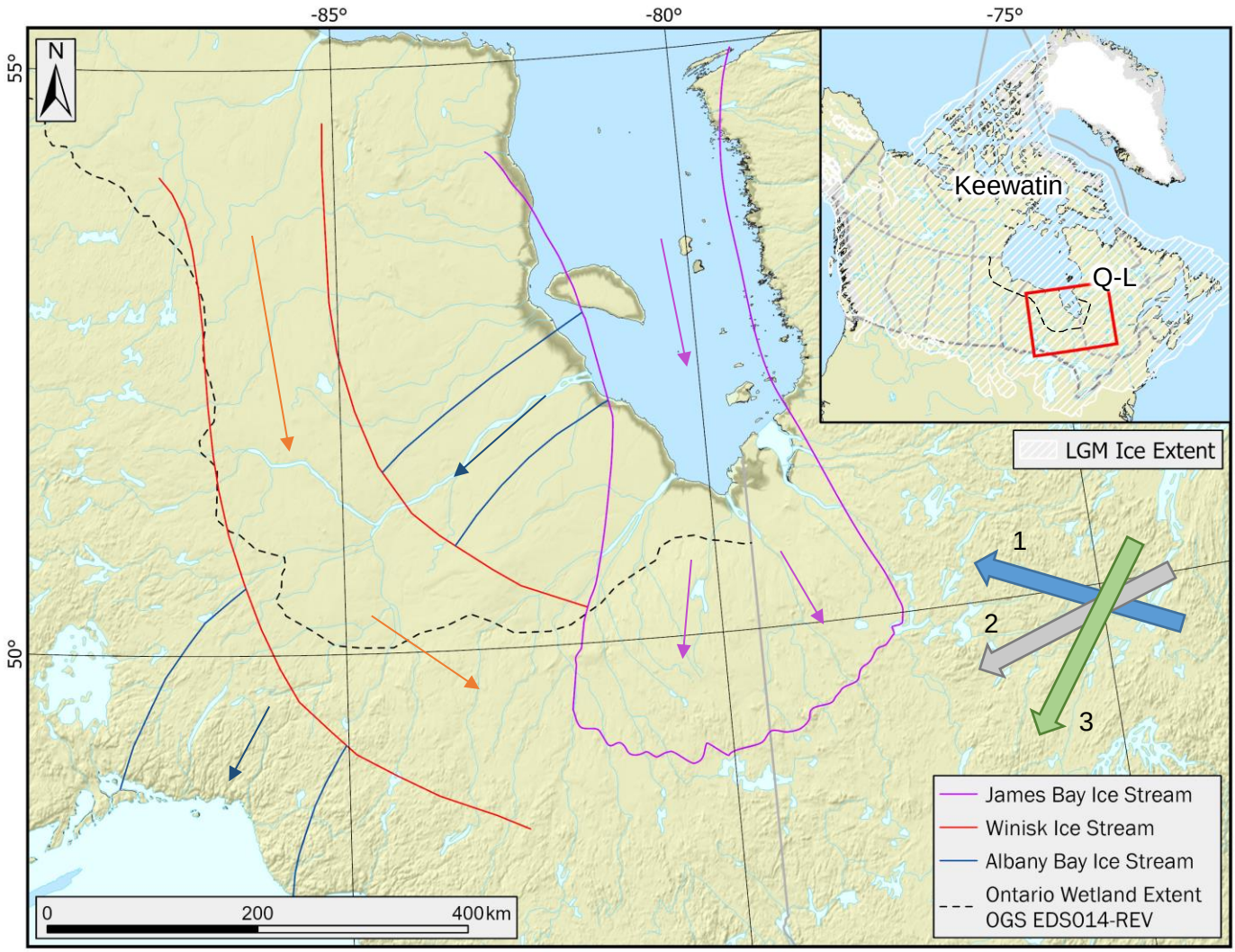


**Figure 1: Dominant ice flow phases, deglacial ice streams (Veillette et al., 2017), HJBL extent (Ontario Geological Survey, 1997), and Canadian DEM (Natural Resources Canada, 2023). Ice flow radiated from the Quebec-Labrador (Q-L) Sector towards the northwest through to southeast (arrows 1, 2, 3). Deglacial ice streams occurred in the order of Albany Bay, Winisk, and James Bay Ice Stream. Inset shows extent of the HJBL, ice extent at the LGM (Dalton et al., 2023), and the approximate centers of the Keewatin and Q-L Sectors.**

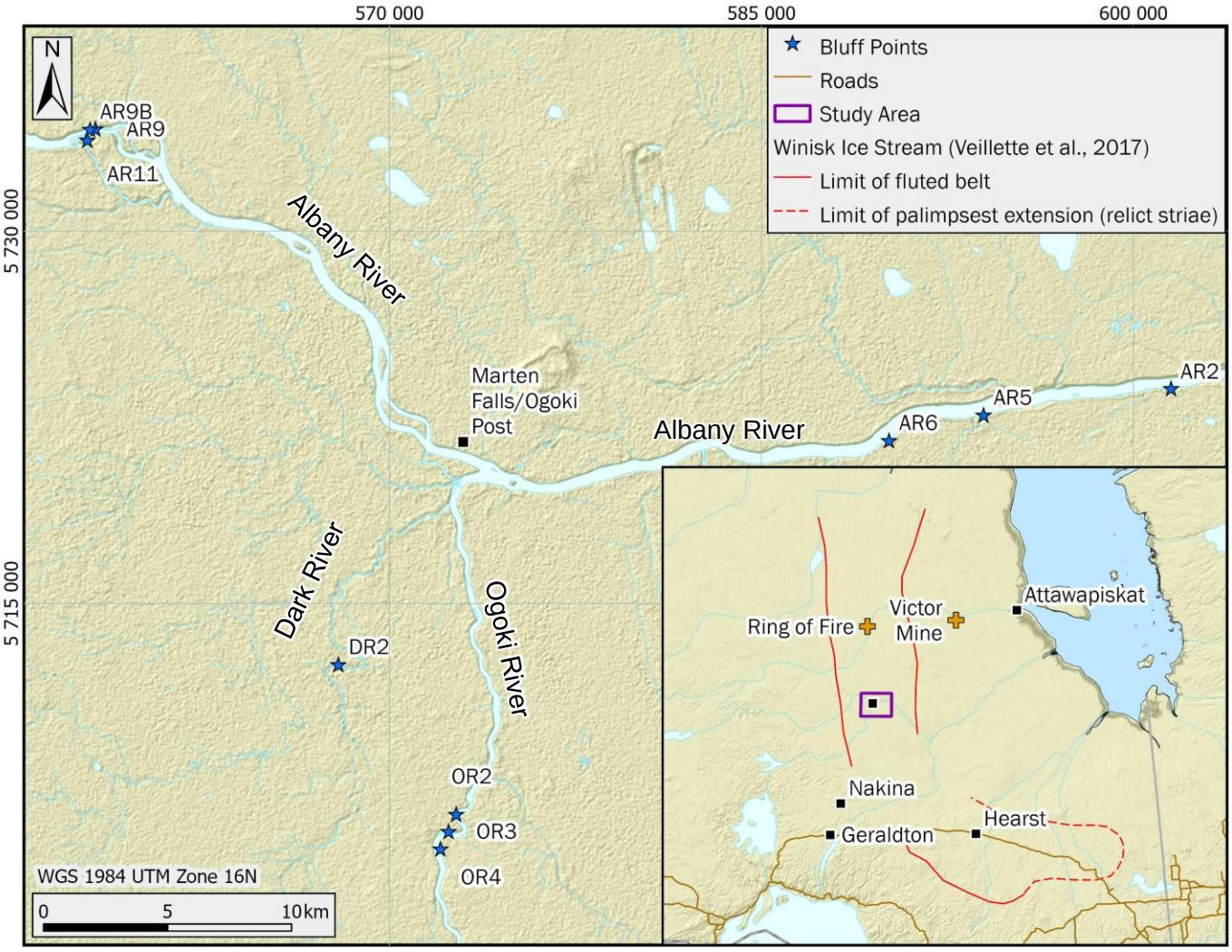


**Figure 2: Bluff locations within the upper part of the Winisk Ice Stream (red) as delineated by Veillette et al. (2017). The bluffs are in proximity to Ogoki Post, the Ring of Fire, and Victor Diamond Mine.**

### 1.2 Geologic Setting

Topography in the HJBL is remarkably flat with elevations generally below 200 m asl (Ontario GeoHub, 2023). The average elevation increases from the Hudson and James Bay coast up to the 200 m asl at approximately 350 m inland is about ~0.6 m/km, aside from the steeper area south of James Bay (**Figure 3**).

**Figure 4** shows the bedrock of the HJBL and Hudson Bay consisting of Archean and Proterozoic (Precambrian) rocks of the Superior Province dominated by foliated tonalites, granodiorites to granites, and belts of mafic to ultramafic rocks (United States Geological Survey, 2005; Ontario Geological Survey, 2011). Precambrian rocks are unconformably covered by Phanerozoic sedimentary strata of dominantly carbonates (limestones and dolostones) and

shales of the Paleozoic era (Ordovician to Devonian periods) within two basins, the Hudson Bay and Moose River basins (Sanford et al., 1968). There are infrequent Precambrian inliers in the Paleozoic cover with the most prominent being the Sutton Inliers on Cape Henrietta, coincident with the divide in Paleozoic basins (Sanford et al., 1968; Thorleifson et al., 1993). The rise in topography and change in substrate at the Precambrian shield rock influenced ice flow, particularly on the late stage Winisk Ice Stream (Veillette et al., 2017), when ice was thinner.

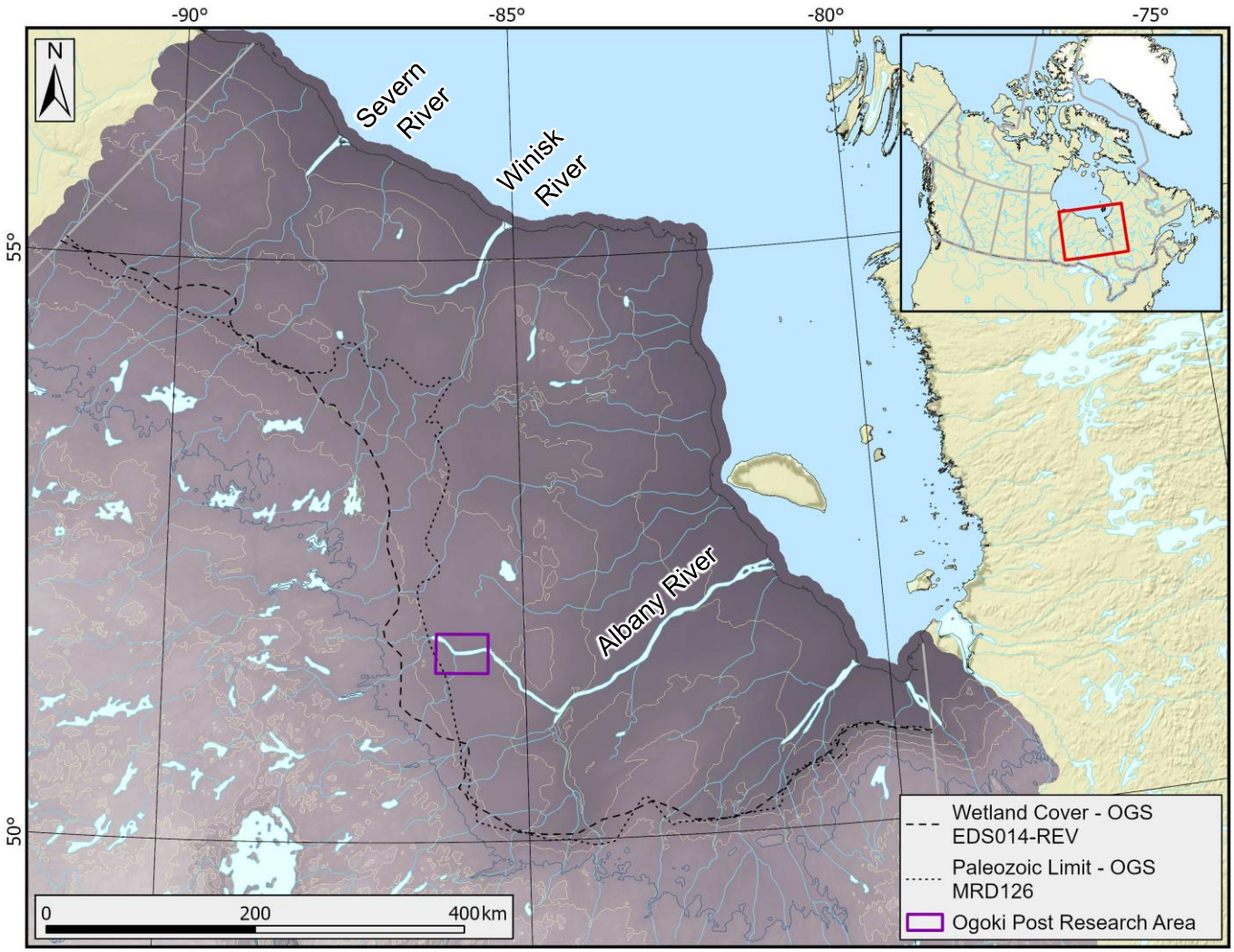


**Figure 3: Provincial digital elevation model (DEM) (2023) with 50 m contours in yellow (250 m in blue) showing the low gradient topography in the HJBL aligning with the occurrence of Paleozoic bedrock and wetland cover in northeastern Ontario.**

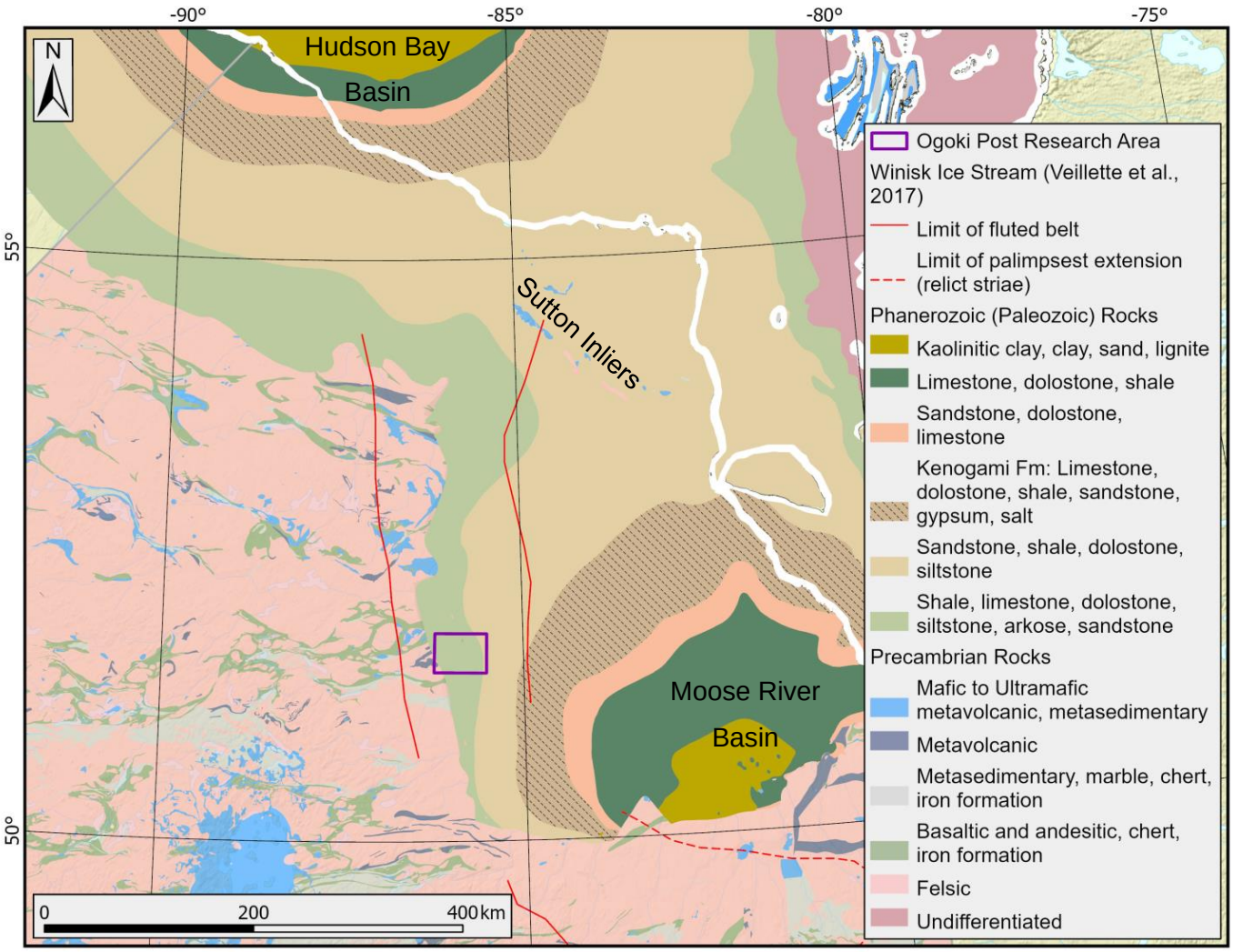


**Figure 4: Bedrock geology of North America and Ontario (United States Geological Survey, 2005; Ontario Geological Survey, 2011) showing extensive Paleozoic sedimentary rocks in the HJBL with the Precambrian Sutton Inliers on Cape Henrietta. Under the Paleozoic sedimentary cover are the Precambrian rocks of the Canadian Shield.**

Quaternary cover in the HJBL is largely organic material with infrequent bedrock, till, fluvial, and marine material exposed (**Figure 5**). Off the margin of the HJBL is more extensive till cover and then bedrock with till veneer and zones of glaciomarine and glaciofluvial material. The boundary of flat, wetland cover is roughly coincident with 200 m asl and the transition from Paleozoic sedimentary rock cover to Precambrian shield rocks (**Figure 4**), discussed below. As ice retreated, proglacial lake Agassiz-Ojibway deposited glaciolacustrine material. Then as the ice sheet collapsed, the flat nature of the Paleozoic cover and overlying till and glaciolacustrine sediments allowed marine waters of the Tyrrell Sea to inundate a large swath of land, depositing a layer of glaciomarine material, preventing effective drainage (Dredge and Cowan, 1989;

Vincent, 1989). Organic cover developed above the glaciomarine sediment cap once the HJBL isostatically rebounded and marine waters retreated. Throughout deglaciation and isostatic rebound, it is anticipated that the smooth topography would have prevailed given the relatively short time frame since the LGM.

The study area is within the HJBL near the transition from Paleozoic bedrock with extensive wetland cover onto the Precambrian shield with an overlying till veneer.

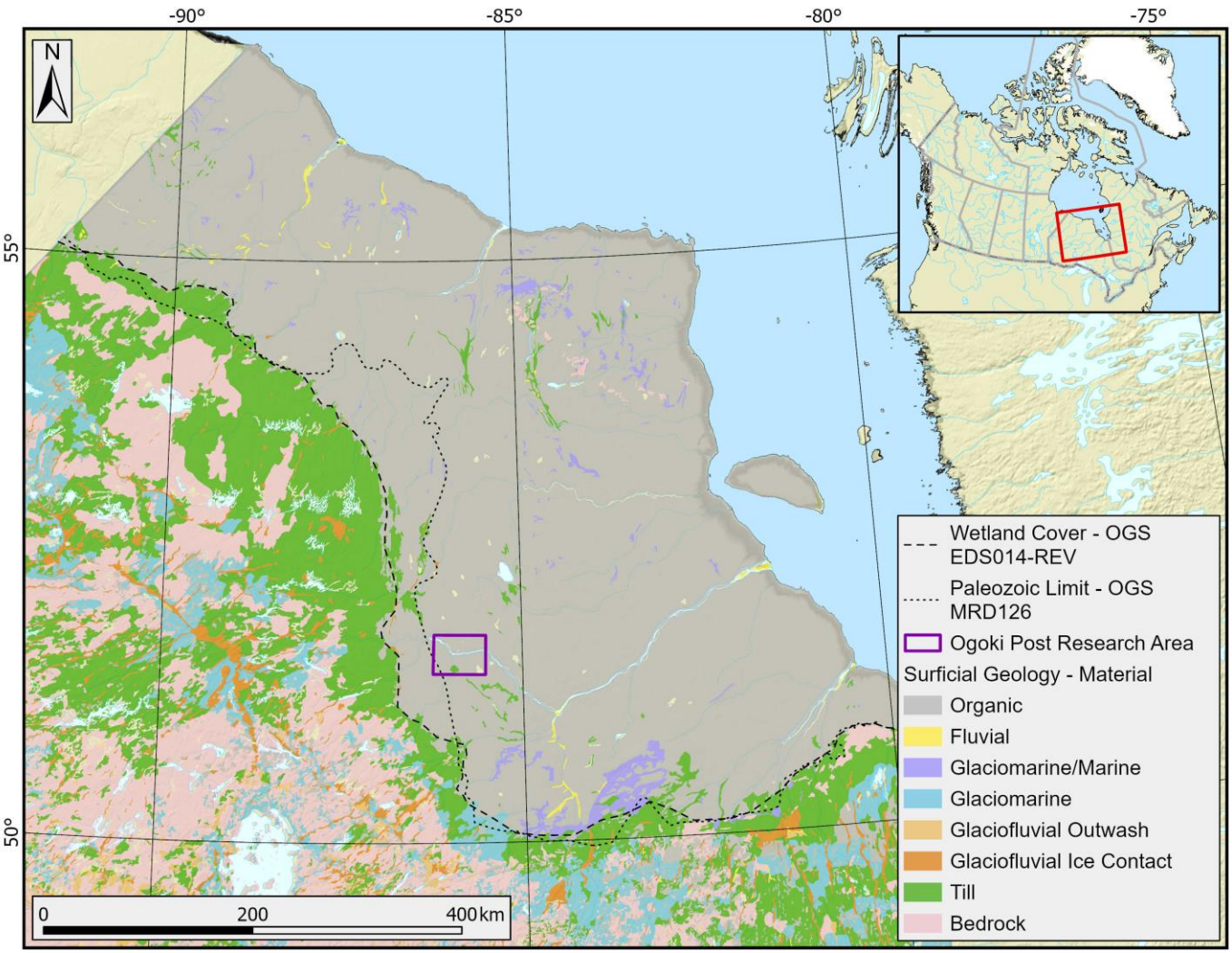


**Figure 5: OGS EDS014 (Ontario Geological Survey, 1997) at 1:500 000 scale showing surficial material type across northern Ontario with extensive wetland cover.**

### 1.3 Regional Quaternary Stratigraphy

There have been many stratigraphic studies of exposures along the main rivers and correlations across the expansive HJBL (**Figure 6**). Studies have used principles of lithostratigraphy, chronostratigraphy, biostratigraphy, and ice-flow indicators (e.g., landforms, striae) in a variety

of combinations to make local and/or broad correlations. Research began in earnest during Operation Winisk, a government survey that traversed the entire HJBL in 1967 (McDonald, 1969). Skinner (1973) did extensive stratigraphic research in the Moose River Basin, southwest of James Bay, along with Shilts (1982). Manitoba studies notably include Dredge and Nielsen (Dredge and Nielsen, 1985; Dredge and McMartin, 2011; Wang, 2018) and Klassen (1986) with extensive, ongoing research by the Manitoba Geological Survey (Hodder et al., 2017; Gauthier et al., 2019, 2021, 2022). Along the Hudson Bay coast in Ontario, Thorleifson et al. (1993) studied several prominent river bluffs along the Severn and Winisk drainage basins and made correlations to units identified and described in the prior mentioned studies. Veillette et al. (2017) used erosional ice-flow indicators and landform to interpret the ice-flow history south of the HJBL on the shield at the far southern reaches of the Winisk Ice Stream (WIS). As part of a predictive mapping field validation study, Gao et al. (2015) visited several bluff locations within the WIS and correlated units to regional knowledge. Dalton et al. (2018), with a focus on organic-bearing sediments, have interpreted bluff stratigraphy along the Albany River close to the James Bay coast. Most recently, Gao et al. (2020) have identified a new subtill non-glacial bed on the Winisk River. Regardless of study location, a complex stratigraphic record consisting of stacked glacial (till) and nonglacial (sorted and organic-bearing) sediments has been documented.

The many studies over decades have led to a complex and often fragmented regional framework with ongoing, incremental adjustments. Although no geochronology work is planned as part of this study, understanding the development and status of the existing framework will be instrumental in interpreting the stratigraphic sequences. However, given the extensive area and complexity of the HJBL, this thesis will focus on more proximal Ontario studies along the Winisk River (Thorleifson et al., 1993; Gao et al., 2020) and Albany River (Gao et al., 2015; Dalton et al., 2018).

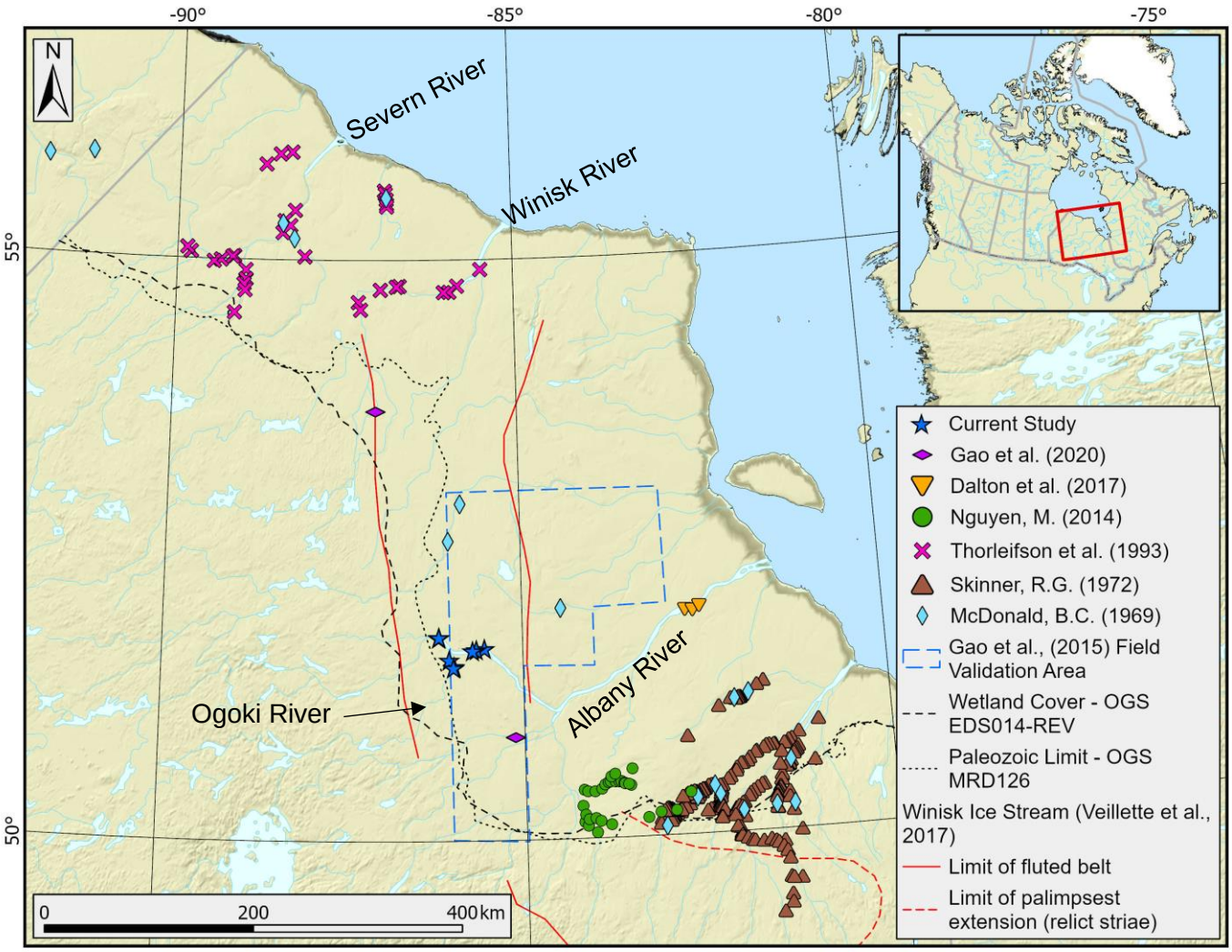


**Figure 6: Key bluff stratigraphy studies in the HJBL including this study (Bluff Locations 2019). The extent of the Winisk ice stream is in red (Veillette et al., 2017) and the field validation work from Gao et al. (2015) is outlined with a blue polygon.**

**Table 1** presents a summary of the main stratigraphic frameworks developed in the large region of the HJBL of northern Ontario. Thorleifson et al. (1993) attributes the lower till in the HJBL, the Shagamu Till, to an Illinoian ice flow event with a southeasterly flow originating from the Keewatin dome based on clast content and stratigraphic location. Gao et al. (2015) attributed interglacial sediments to the Missinaibi Formation (Skinner, 1973) with an underlying till therefore correlated to the Illinoian event, both stratigraphic correlations. Underneath another interglacial unit, Dalton et al. (2018) observed one or two units with striations on boulder pavements indicating a north-northwest ice flow direction and extremely low dolomite geochemistry from an early LIS center on the Quebec highlands. This potentially correlates to the Rocksand Till seen by Thorleifson et al. (1993), which could also be the bottom till observed

by Gao et al (2015) as this correlation is based on stratigraphic position. Above interglacial sediments (amino acid dating on marine shell to Marine Isotope Stage 5 (MIS 5)), Thorleifson et al. (1993) determined a counter-clockwise shift of ice in two till units from west (Sachigo Till: clast fabric and lithology, straie) through to southwest (Severn Till: flutes, clast fabrics, boulder striae). This was followed by a southeast ice flow event (WIS: surface flutes, fabrics) constrained by elevated Precambrian Shield to the west. The Sachigo Till is correlated to the Long Spruce Till in Manitoba (Nielsen et al., 1986) and Adam Till in Ontario (Skinner, 1973), while the Severn Till is correlated to the Sky Pilot Till (Nielsen et al., 1986) and Kipling Till (Skinner, 1973). Thorleifson et al. (1993) observed an interglacial unit, the Fawn River Sediments, between the Rocksand and Sachigo Tills. Thorleifson et al. (1993) initially considered the Fawn River Sediments younger than the Missinaibi Sediments given correlations by Skinner (1973) of the Missinaibi to the Bell Sea, which is pre Rocksand Till. Thus, the sequence suggested by Thorleifson et al (1993) is Missinaibi Sediments, Rocksands Till, Fawn River Sediments, then Sachigo, Severn, and Winisk Tills (**Table 1**).

Dalton et al. (2018) and Gao et al. (Gao et al., 2020, 2015) observed three till units above interglacial sediments in their studies. Dalton et al. (2018) proposed a stratigraphy that includes a non-glacial bed with two till units below and two till units above, with a potential third given a change in ice flow direction (boulder straie). A third unit is at odds with the two expected till units given the study location outside of the WIS (Sachigo and Severn Till) and is indicated to potentially be a late, upper extent of the second unit impacted by high subglacial meltwater pressure (presence of Nye channels and finer material). Within the WIS along the Albany and Kenogami Rivers, the sequence proposed by Gao et al. (Gao et al., 2020, 2015) is a potential Illinoian unit, interglacial sediments attributed to the Missinaibi by stratigraphic sequence, and three till units. The three overlying till units correlate with the Sachigo, Severn, and Winisk Tills respectively (Thorleifson et al., 1993). The lower and middle tills above the interglacial sediments are correlated to the Adam and Kipling Tills respectively (Skinner, 1973) with no correlation to the Winisk Till expected outside of the study region.

Importantly, age discrepancies exist for many of the intertill nonglacial beds throughout the HJBL (Hodder et al., 2023) and this complicates relying on geochronology to correlate nonglacial units over large distances. Thorleifson et al. (1993) did not have a site with both the Rocksand Till and Fawn River Sediments to constrain the relationship. A variety of time frames were proposed for the Bell Sea, Prest Sea, and Rocksand Till based on various dating methods with different implications on the age of the Fawn River Sediments. For instance, due to lack of

stratigraphic control, Thorleifson et al. (1993) mentioned the possibility that Rocksand Till could be equivalent to the Illinoian Amery Till (Nielsen et al., 1986) in Manitoba. This situation further complicates correlation of till units along the Albany River to the Rocksand Till (Dalton et al., 2018). Dalton et al. (2018) conducted optically stimulated luminescence (OSL) on quartz indicating that there are possibly two non-glacial units attributed to MIS 3 or 4 and MIS 5a, or alternatively they are both MIS 5a. If the upper non-glacial is MIS 3 or 4 the underlying till showing ice flow direction comparable to Rocksand Till (Dalton et al., 2018) could be MIS 4. After being questioned, the OSL method for ages of MIS 3 are now considered to be a minimum age, and MIS 5 for both non-glacial beds is likely the correct scenario (Miller and Andrews, 2019; Gao et al., 2020; Hodder et al., 2023). Non-glacial beds on the Winisk River and within the WIS, the Webequie Non-glacial Beds, have been dated to 5e based on OSL dating of K-feldspar grains with three overlying till units (Gao et al., 2020).

There were three late glacial ice streaming events in the HJBL, the Albany Bay, Winisk, and James Bay Ice Streams (Stokes et al., 2016; Veillette et al., 2017; Margold et al., 2018). The southern extent of the James Bay Ice Stream resulted in the ice-marginal Cochrane surges. The Cochrane surges were complex with multiple events advancing into proglacial lakes Agassiz and Ojibway, which largely ended by 8 ka with lake drainage into Hudson Bay (Roy et al., 2011). Thorleifson et al. (1993) state that the Cochrane surges did not extend into the west HJBL but concentrated south of the Moose River Basin on shield rock. Further studies on the crosscutting relationships between Winisk region fluted landforms and Cochrane landforms (flutes and iceberg scours) suggest that the WIS predated and outlasted the Cochrane surges (Veillette et al., 2017).

Postglacial sediments overlie the late Pleistocene sediments described above (**Table 1**) and predominantly include sediments of glacial Lake Ojibway and the Tyrrell Sea. Deglaciation of the study area (**Figure 7**) occurred approximately between 9.0 and 8.5 ka BP (Dalton et al., 2023). Proglacial Lake Agassiz-Ojibway discontinuously deposited silt and clay varved sediments along the receding ice margin which are seen to transition upward to marine silts and clays of the inundating Tyrrell Sea where the two waterbodies overlapped, predominantly in the west HJBL (Gao et al., 2015). Dalton et al. (2018) also observed Tyrrell Sea sediments, but Lake Agassiz-Ojibway sediments do not extend as far east as their study area (**Figure 6**).

**Table 1: Simplified Ontario Quaternary stratigraphy from Thorleifson et al. (1993), Gao et al., and Dalton et al. (2018). Note that Dalton et al. (2018) and Gao et al. (2020) did not make regional correlations in their publication but correlations are made here by the author. Nielsen et al. (1986) and Skinner et al. (1973) included for regional reference.**

| MIS | Nielsen et al. (1986) Manitoba | Thorleifson et al. (1993) Winisk River | Gao et al. (2015) Albany River region | Gao et al. (2020) Winisk, Little Current Rivers | Dalton et al. (2018) Albany River | Skinner et al. (1973) Ontario |
|---|---|---|---|---|---|---|
| 1 | Postglacial | Postglacial Sediments | Postglacial Sediments | Postglacial Sediments | Postglacial Marine Sediments | |
| 2 | | Winisk Till: brown, in east only, on boulder pavement, N-S flutes and ice flow indicators<br>Amino acid (shells) | Till 3<br>Fabric and lineations: S | Upper Till: 0.3-2 m thick, clayey silt, brownish, high red carbonate clast content, N-S surface flutes | Till 4/5: Nye Channels, finer than below, W-NW ice flow indicators | |
| 2 | Sky Pilot Till | Severn Till: grey, moderate Proterozoic, high red carbonate clasts, SW ice flow (flutes, fabrics, boulder straie)<br>Amino acid (shells) | Till 2<br>> 2 m thick<br>Fabric: SW | Middle Till: 1.5-2 m, yellowish to light brown, sharp lower unconformable contact with sand. S-SW ice flow (intermediate clast lithology) | Till 4: light grey-brown, massive, low clay content, stratified sediments throughout S-SW flow (striated boulder to 204°) | Kipling Till |
| 3/4 | Long Spruce Till | Sachigo Till<br>Upper is red, SE ice flow (red carbonate clasts)<br>Lower is grey, E-W ice flow (fabric, boulder straie, Proterozoic clasts) | Till 1<br>> 2 m thick<br>Fabric: West<br>Lower Contact: Sharp, erosional | Lower Till: 6 m thick, dark grey, compact, SE flow (high proterozoic argillite and greywacke clasts and jasper ironstones) | Till 3: dark grey-brown, heavily lensed, high clay content | *Adam Till?* |
| 5e | Nelson River Sediments | Fawn River Sediments*<br>Paleo-ecological correlation | Non-Glacial Stratigraphic correlation | Webequie Non-glacial Beds<br>OSL on K-feldspar and radiocarbon on wood.<br>Chronostratigraphic correlation | Non-glacial Sediments<br>$^{14}C$ and OSL on Qtz give MIS 3, now attributed to MIS 5 (Hodder et al., 2023) | Abitibi River Sediments |
| 6 | Amery Till | Rocksand Till*: grey, NW-SE (fabric), WNW (striae, landforms), Proterozoic rich, red carbonate clast poor<br>Amino acid (shell), TL - now negated | | | Till 1/2 (Rocksands?): dark grey-brown, S-SW flow (high limestone/dolomitic clasts), high base metals | *Adam Till?* |
| 6/7 | Sundance Till | Shagamu Till: SE ice flow (red carbonates, therefore not Rocksands Till) | Basal Till<br>Stratigraphic correlation (could be Rocksands) | | Till 1 (Rocksands?): dark grey, clay/silt rich, N-NW flow (low dolomite/calcite, stone lines, boulder striae), high base metals | Pre-Missinaibi Interglacial Tills |

*no stratigraphic control between Rocksands Till and Fawn River Sediments

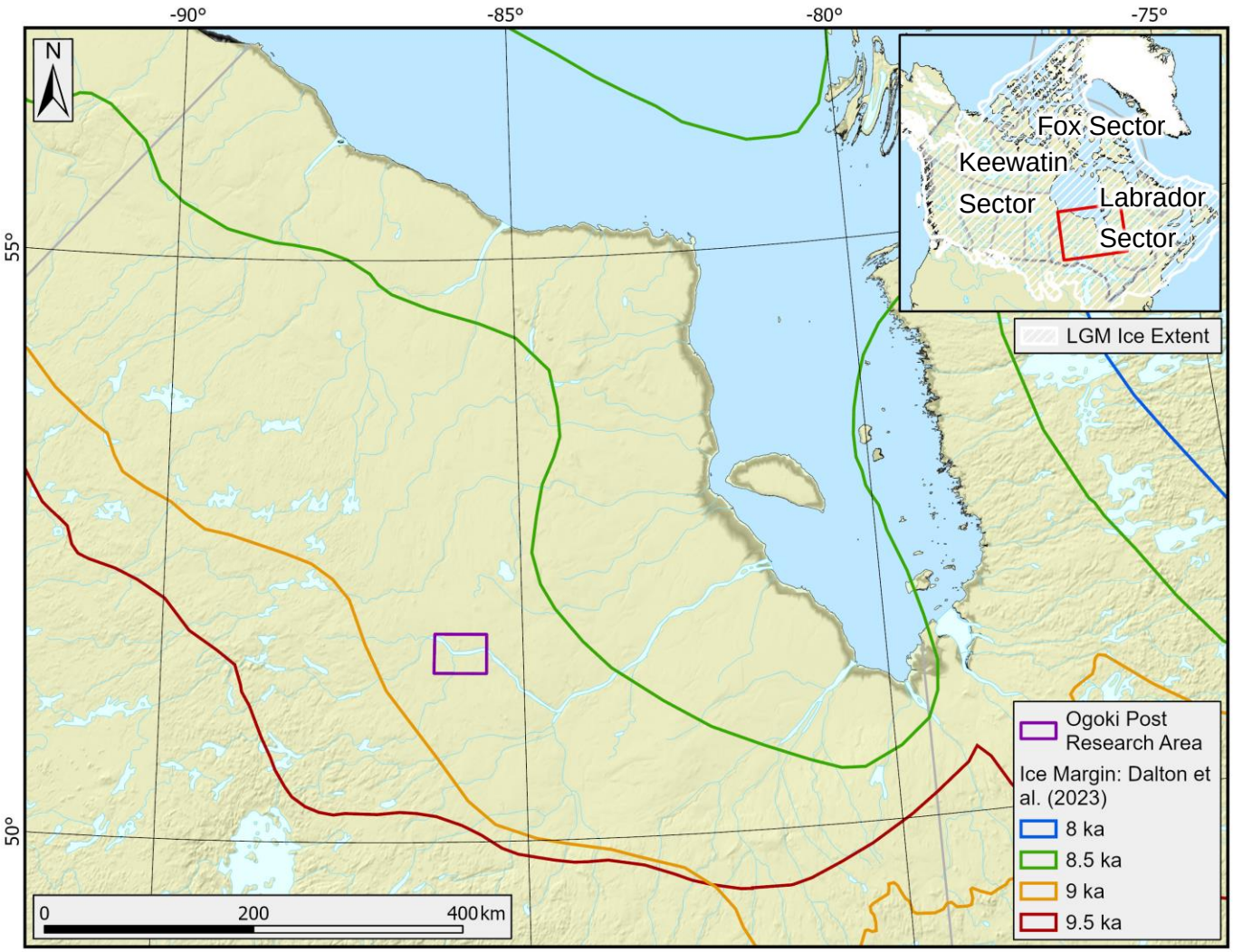


**Figure 7: Deglaciation across the HJBL started shortly after 9 ka and was complete before 8 ka (Dalton et al., 2023).**

### 1.4 Knowledge gaps

Stratigraphic sections mainly occur as river bluffs and ravines along the main rivers incised into HJBL Quaternary sediments. Detailed studies on numerous closely spaced sections have been done in northeastern Manitoba, far northern Ontario, and along the Moose River in Ontario, but limited studies have been done in the southwestern part of the HJBL (**Figure 6**). This gap in the spatial coverage of stratigraphic sites in the southwest challenges unit correlations at the regional scale. The lack of bluff sections in this area impedes interpretations and overall understanding of the WIS. More recent research along the reaches of the Albany River (Gao et al., 2015; Dalton et al., 2018; Gao et al., 2020) have advanced our understanding of the non-glacial events and regional ice flow phases, but important uncertainties and knowledge gaps remain for a large area within the HJBL. A detailed investigation of stratigraphic sections in the

understudied central region between the previously explored sites will benefit the regional ice flow interpretation, till stratigraphy and provenance, and our overall understanding of past glacial dynamics of this vast region. This project is also in an ideal location to study the WIS given its central location to the interpretated boundaries and the east-west path of the Albany River cutting a natural transect perpendicular to ice movement.

### 1.5 Research Objectives

Our knowledge of the LIS evolution and late glacial ice streaming events and how the subglacial dynamics impacted sediment dispersal in the region remains limited. This study's location proximal to the Albany River, within the HJBL and the WIS, is an ideal area to document the till stratigraphy and provenance which will provide important insight into the regional glacial history and genesis of glacial sediments (entrainment, transport, and deposition mechanisms). The research objectives are as follows:

1) Determine the nature and style of glacial sediment production and deposition during the multiple ice flow phases by detailing sediment characteristics (i.e. compaction, colour, particle size, clast fabric and striae) and composition (i.e. till-matrix geochemistry, clast lithology counts). Define the relationship between ice flow phases and subglacial sediment characteristics.

2) Reconstruct ice flow phases around the middle reach of the Albany River in north-central Ontario. This includes determining the number, relative age, and direction of the main ice flow phases to develop a Quaternary stratigraphic framework from the depositional record of the LIS preserved in stratigraphic sections in the study area (**Figure 6**). Then compare with the existing regional ice flow interpretations from proximal and recent regional studies.

The development of a model of sediment provenance and dispersal will provide insights into the glacial dynamics through time.

These objectives will be achieved through the study of 10, river-incised bluffs to gather data on ice flow history, provide insights to subglacial dynamics, and to determine glacial sediment provenance. The following data was collected for comparison, integration, and correlation with the existing regional ice flow and stratigraphic framework: stratigraphic logs, clast fabrics (measurements of the a-axis orientation of clasts entrained in matrix-supported till), clast striae, particle size analysis, clast lithology counts, till matrix geochemistry, sediment characteristics

and features (i.e. clastic dikes), and landform mapping from satellite imagery and digital elevation models (DEMs).

Subglacial conditions will be inferred from sediment characteristics and features such as compaction, till fissility, brittle and soft deformations, and post-depositional structures. Combining directional indicators (clast fabrics and striae) with sediment geochemistry (ICP, ICP-MS, calcium magnesium ratio), particle size analysis (PSA), and sediment characteristics will contribute to reconstructing ice flow directions and subglacial conditions during different ice phases.

The following chapters begin with using sediment characteristics to develop a foundational stratigraphic sequence (Chapter 2). Chapter 3 discusses the composition (till matrix geochemistry and clast lithology count data) to introduce provenance interpretations to the stratigraphy. Finally, Chapter 4 integrates and summarizes all data into a stratigraphic framework to be correlated into the regional stratigraphic framework (Chapter 5) of the HJBL glacial history.

# Chapter 2. Sediment Characteristics and Glacial Indicators

## 2.1 Introduction

This chapter discusses the methods and results of sediment characteristics encountered including colour, particle size, compaction, and fissility. An initial stratigraphic sequence for the study area (objective 1) is developed by combining glacial characteristics, such as clast fabric and striae data, boulder pavements, and pipe flow features prior to integrating geochemistry and clast count analysis, which is the subject of Chapter 3.

## 2.2 Methods

### 2.2.1 Stratigraphic Logging

Stratigraphic logging at 10 river-incised bluff exposures along the Ogoki, Albany, and Dark Rivers **(Figure 2)** allowed for the identification of distinct beds using standard stratigraphic and sedimentological field methods (Evans and Benn, 2004; McMartin and Paulen, 2009; Dalton et al., 2018). At each site, an approximately one-meter width was cleared from the top of the bluff down into slumped material with contacts measured from the top of the bluff. Full stratigraphic columns were drawn at each location and digitized with each's bluff's angle accounted for to derive true thicknesses (Appendix A: Detailed Stratigraphic Columns). Two bluff angles were not measured in the field. The average bluff dip of 46˚ was used at DR2 but no dip was applied at AR9B as measurements were approximate and corrections likely less accurate than field noted thicknesses.

Most identified units were sampled once, or twice if sediment characteristics changed or the unit was particularly thick, resulting in a total of 46 diamicton and 2 sand/gravel samples. Each sample was screened in the field with a 20 mm mesh to a final weight of approximately 20 kg. Clast fabrics were collected at many sample sites as clasts within till can become imbricated and thus indicate ice flow direction. Clast striae were measured where available. **Table 2** contains bluff details as well as sample and clast fabric counts.

Multi-faceted, subrounded clasts (with or without striae) within a diamicton are characteristic of subglacial traction till (Evans et al., 2006). In addition, high compaction and the presence of boulder pavements were used to identify material as till. These diagnostic characteristics were not included in the stratigraphic column descriptions for till units as they are common throughout, except boulder pavements. Pipe flows and other glacial features were noted if present. Tills were further divided into groups based on sediment characteristics. The field

categorization is not absolute but rather a primary guide for further interpretation. If analytical characteristics indicated a sample deviated from the till group attribution, field photos and notes were reviewed and a case was made to either maintain or change the designation for the final interpretation.

**Table 2: Stratigraphic section codes with count of samples and clast fabrics. The calculated true thickness is of exposed stratigraphy only and approximate.**

| Bluff Name | Dip | True Thickness (m) | Sample Count | Clast Fabric Count | NAD83 UTM 16N Coordinates |
|---|---|---|---|---|---|
| AR11 | 55˚ | 8.6 | 4 | 3 | 557809E 5733679N |
| AR2 | 50˚ | 9.1 | 9 | 5 | 601518E 5723671N |
| AR5 | 50˚ | >4.8 | 4 | 2 | 593954E 5722602N |
| AR6 | 48˚ | 3.7 | 4 | 4 | 590141E 5721578N |
| AR9 | 46˚ | 7 | 4 | 2 | 558138E 5734130N |
| AR9B | ^ | 5.8 | 2 | 3 | 557927E 5734116N |
| DR2 | **46˚ | 3.6 | 4 | 4 | 567937E 5712549N |
| OR2 | 36˚ | >3.1 | *6 | 5 | 572686E 5706513N |
| OR3 | 37˚ | 5.6 | *7 | 6 | 572377E 5705821N |
| OR4 | 43˚ | 5.8 | 4 | 5 | 572049E 5705116N |
| Total | | | 48 | 39 | |

* Indicates a sand/gravel sample present **Dip averaged from all sites ^ No dip correction

### 2.2.2 Sample Processing

Samples were received from the field at the De Beers Sudbury Sample Treatment Centre (SSTC) and processed according to De Beers' internal standards (De Beers Group, 2019). Prior to SSTC processing, a 250 g geochemistry grab sample was taken from each sample, dried, and sent to Saskatchewan Resource Council (SRC) in late 2019 for till matrix geochemistry analysis and particle size analysis. An additional 500 g grab archive was taken, dried, and sent to the University of Waterloo where the munsell colour of each sample was determined from the dry material.

### 2.2.3 Particle Size Analysis

No field duplicates were collected or standards submitted, but during analysis the lab completed three standards (SSC0219) and two lab duplicates. This results in ~10% QA/QC material in the sample set which is low but within the recommend 5 – 20% by Piercey (2014).

#### Standards

The analytical precision (reproducibility and repeatability) was reported as relative standard deviation (%RSD) and accuracy (trueness of a value) as the percent relative difference (%RD) of the three standard analyses according to Piercey (2014) and Jenner (1996).

The particle size results had a %RSD of 0.46%, 0.45%, 0.35%, and an %RD of 1.4%, 1.3%, and 0.7% for sand, silt, and clay respectively. This is all well below the 10% threshold for accuracy and precision so the results are acceptable (Piercey, 2014; McCurdy and Garrett, 2016).

#### Duplicates

The average coefficient of variation ($CV_{avg}$(%)) was calculated on the two duplicate samples to determine precision (Piercey, 2014). The $CV_{avg}$(%) for the PSA was 1.8%, 0.2%, and 1.9% for the sand, silt, and clay respectively. This is well below the threshold of 5 – 7.5% for analytical duplicates (Piercey, 2014).

#### Analysis in ioGAS

Particle size results were analyzed using ioGAS 7.4.2. The weight percent was used to generate a ternary plot as well as box plots. Box plots were also performed on a centered log ratio transformation with comparable results to the weight percent box plot. The number of k-means clusters was established at three based on a scree plot of the sum of squares distances from the centered-log ratio (CLR) data using the 'elbow' method. A principal component analysis (PCA) was performed but not used herein.

### 2.2.4 Clast Fabrics

Subglacial shear stress tends to align the long axis of elongate pebbles entrained in matrix-supported till parallel to ice flow direction (Holmes, 1941; Hicock et al., 1996; Evans et al., 2006; McMartin and Paulen, 2009). The orientation of elongated clasts can thus be used to infer the direction of shear stress, which is often interpreted to represent paleo-ice flow direction. The trend and plunge of the long (a-) axis of clasts in till was collected for clast fabric analysis to interpret the ice flow direction of identified till units. Fabrics were foregone if other flow indicators were present (boulder pavement containing flat-topped boulders with parallel striations). A total of 39 fabric sets were collected (**Table 2**) consisting of ~50 measurements each for a good sample population (Benn, 2007). Each measurement includes the trend and plunge of an elongated clast. Elongation is defined as the length (a-axis) to width (b axis) ratio and a minimum of 2:1 was used in accordance with other studies (McMartin and Paulen, 2009). A

knitting needle was used to extrapolate the plunge of the a-axis from the section face and increase measurement accuracy. A 2019 regional declination of 11.5˚ west was accounted for in all compass measurements.

A python script modified (Ross, 2022) was used to plot equal area stereonets, to visualize the fabric and determine if a certain ice flow direction is apparent from the 3D orientation of clasts. Eigenvalues and eigenvectors were calculated to indicate the strength and orientation of the principal components. Eigenvalues were normalized to sample size with S1 being greater than S2, which is greater than S3 (i.e., S1>S2>S3) and summing to 1. Fabrics with S1 ≥ 0.54 were deemed useful for paleo-ice flow determination (Benediktsson et al., 2016), of which only 14 in this study were (36%). Clast fabrics can vary with factors such as clast size (Carr and Rose, 2003), shear plane inclination (Iverson, 2017), and local pressure regime variations (McMartin and Paulen, 2009). As such, they are best used in conjunction with other ice flow indicators (Hicock et al., 1996; Benn, 2007). During field collection, there was some discrepancy between recording up vs down plunge during measurements which may not have been accurately corrected. As such and in addition to natural factors that can cause variation and up-ice plunge, the $V_1$ + 180˚ guide to produce ice flow direction was used with caution if the direction was counter to regional ice flow understanding.

## 2.3 Results

### 2.3.1 Material Classification and Stratigraphy

Sorted units were identified at the top of most bluffs and at or near the base of three sections, overlain by till. These units are laminated fines to moderately sorted gravels and interpreted as glaciolacustrine (with or without drop stones) or glaciofluvial respectively. **Figure 8** shows a selection of the sorted units and their characteristics.

There were four till groups identified during field logging based on visible sediment characteristics. The predominant characteristic of these groups was colour and they are named accordingly; Grey, grey-brown, brown, and red. Although stratigraphic variation exists and is discussed further below, the dominant sequence begins with a grey till at the base, which is overlain by a grey-brown till, then a brown till, and finally with a red till being the uppermost till observed. An example of each till facies is shown in **Figure 9**.

#### Grey Till (Lower)

The grey till is lowest in the till sequence (i.e., sorted units excluded) of nine sections. This till is highly compact with coarse fissility and jointing and disintegrates in blocky chunks. Clastic dikes

related to post-depositional hydrofracturing were seen in four bluffs, exclusively in the grey till, which indicate high basal pressures in a subsequent flow event (**Figure 10**). Sand lensing is common throughout the sections but is rarely seen in the grey till. Boulder pavements were observed at the upper contact of four grey till units, with an additional pavement within one grey unit. At two sections the grey till is observed above a unit of grey-brown till, but never above a brown or red till.

### Grey-Brown Till (Lower Middle)

The grey-brown till is observed at five sections. At three of these sections a boulder pavement separates the grey-brown and grey tills. At AR2 there is a thick grey-brown unit with lensing of sand throughout. At OR3, the grey-brown till is very thin (~20 cm) between two beds of sorted sediment, both bounded by grey till. Grey-brown till is comparable to the grey till with high compaction, coarse fissility, and a blocky nature. Deviation from this is in the two prior mentioned units with the thin unit bounded by sorted material being weakly compacted and the sand lensed unit having increasing compaction up-bluff. Like the grey till, the grey-brown till is never observed above a brown or red till. Its only sequence variation is with the grey till.

### Brown Till (Upper Middle)

The brown till has variable characteristics and is present at all but one section. Fissility is generally fine to medium with moderate compaction and much less blocky than the grey and grey-brown tills. The relationship of brown till to other units is variable, but it was not observed below the grey or grey-brown till. The brown till in sharp contact with the underlying grey till at four sections, one defined by a boulder pavement. At three sections it is underlain by the grey-brown till, two of these contacts are gradational. Gradational contacts are only seen at these two sites or between units of red till. At two sections it is situated above the red till, in one case with a silt lens separating the two tills. However, at the other three sections that have both red and brown till, the brown till is below the red till. As it is seen below the red at three of five sites and has a gradational contact with grey-brown till at two sites, it is generally considered to be below the red till.

### Red Till (Upper)

Like the brown till, the red till also has variable sedimentological characteristics. Fissility ranges from fine to coarse, but in general is less blocky than other till units. Red till is commonly associated to silt layers in the stratigraphy and has silt lensing throughout. Red till was not seen below grey or grey-brown till and its variable relationship to brown is discussed above. The

spatial occurrence of red till is restricted to west half of the study area, with the eastern three bluffs lacking any red till.

A stratigraphic column (example **Figure 11**) summarizing descriptions, lithocodes, PSA, clast count (Section 3.3.1), and other details were generated for each bluff and can be found in the appendices (Appendix A: Detailed Stratigraphic Columns).

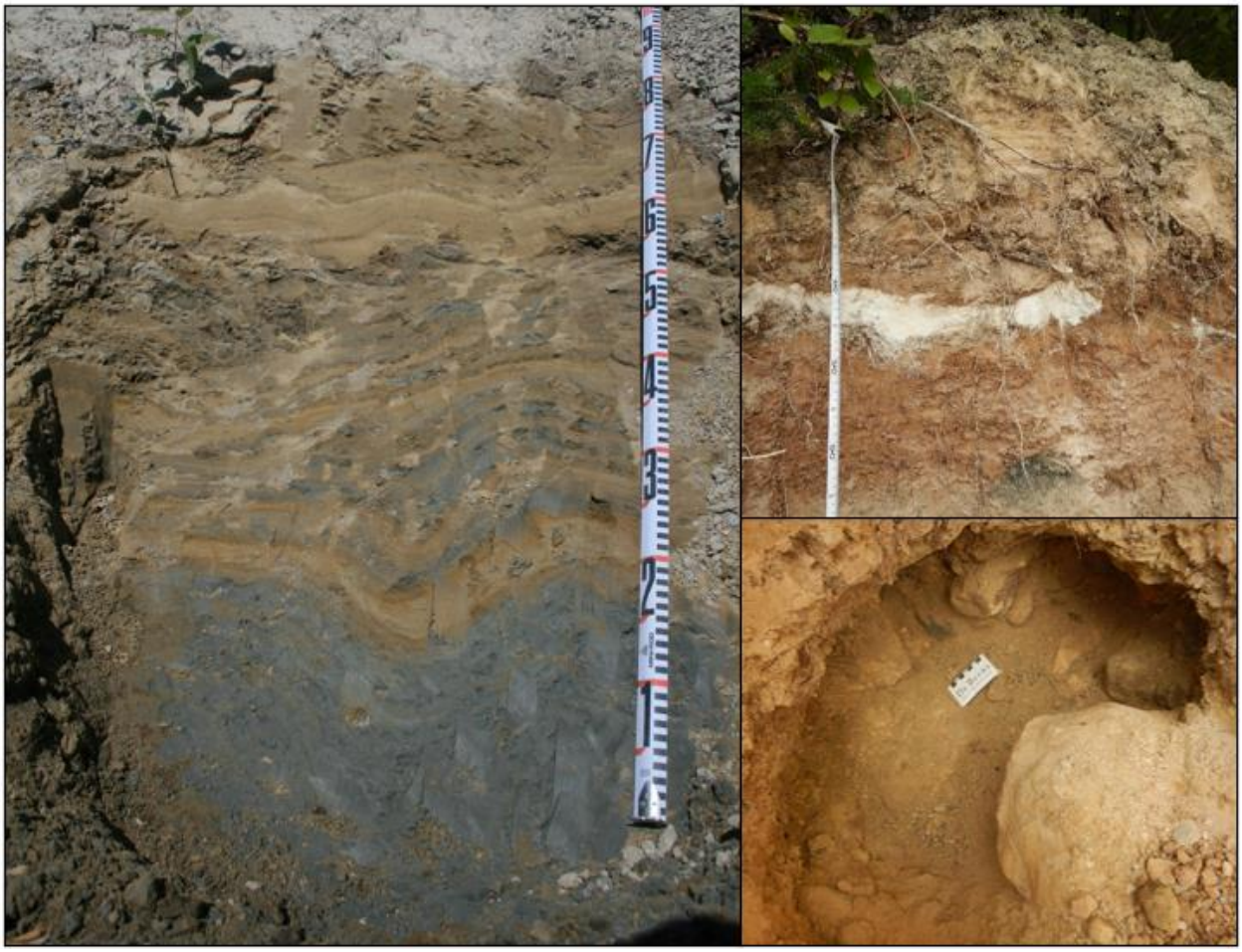

**Figure 8: Left: Laminated and deformed silts and clays coarsening upwards at the base of AR9 and AR9B. Top Right: tan varves at the top with a silt lense at the contact with red varves above a sharp contact with till at AR6. Bottom Right: Massive, matrix-supported coarse gravel to boulder unit at OR2.**


**Figure 9: Example of different till units observe in the study area: (a) red, (b) brown, (c) grey-brown, and (d) grey.**


**Figure 10: Post-depositional, vertical, moderately-sorted, fine to coarse sand layers related to hydrofracturing at AR5 (left) and DR2 (right). The feature at DR2 has a soft, ductile, deformation style suggesting it was syn-depositional.**

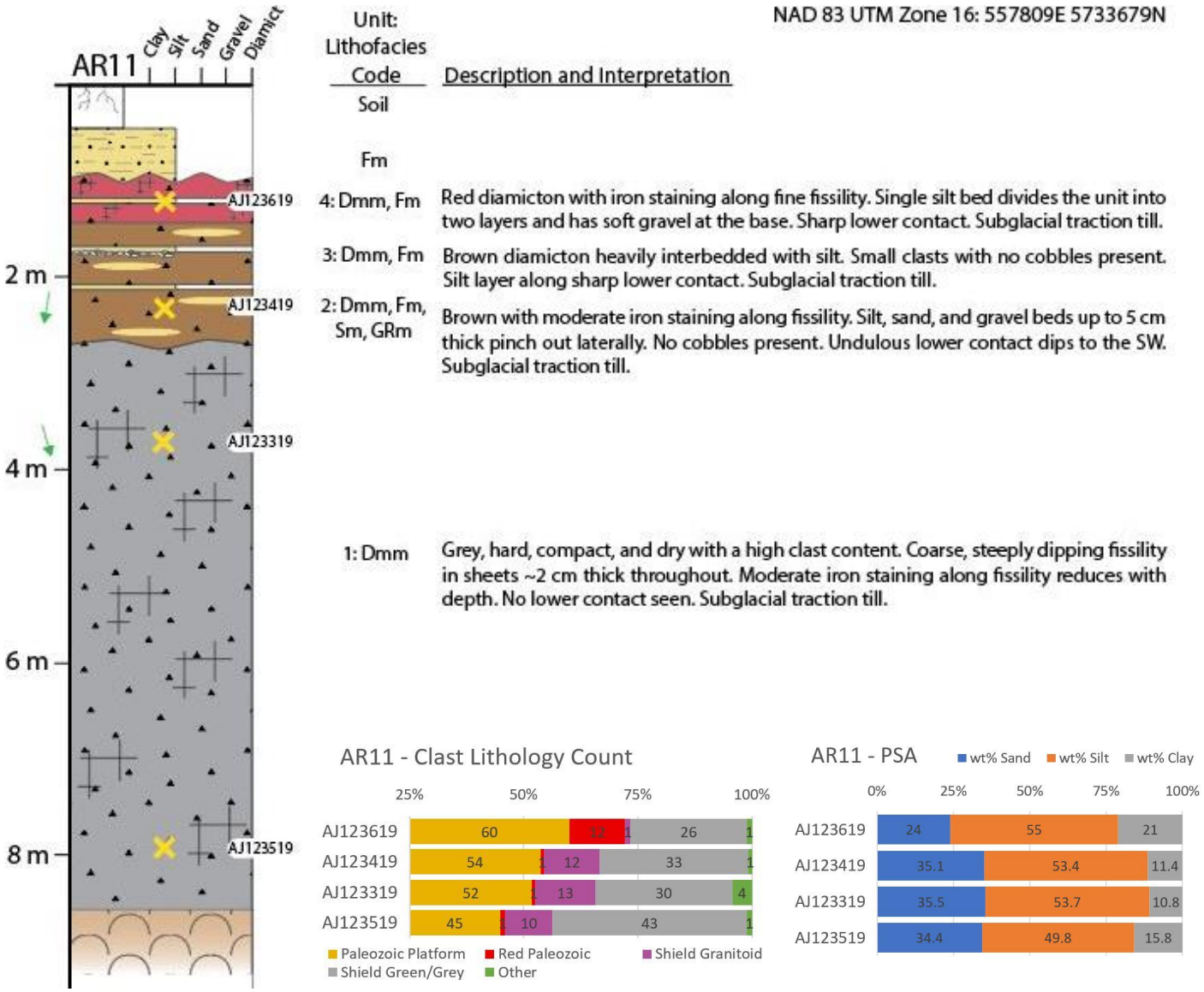


**Figure 11: Example stratigraphic column (AR11) generated for each bluff with slump displayed as brown with curves at the base**

### 2.3.2 Particle Size Analysis

Analysis of the Particle Size Analysis (PSA) defined three clusters. Cluster 1 is defined by sand while Cluster 3 is dominated by Clay, Cluster 2 lies in between the two other clusters with a closer association to Cluster 1. **Figure 12** plots the weight percent (wt %) of the PSA analysis on a scale adjusted ternary plot to demonstrate the clay/sand control between clusters and lack of silt control. Cluster 2 and 3 have a clear boundary at 16 – 18 wt % clay whereas the boundary between Clusters 1 and 2 is tight at 10.9 wt %.

**Figure 13** plots the PSA cluster results by field observed till colour. Red till dominates Cluster 3 with high clay compared to other till colours, likely indicating a Paleozoic platform material source. Grey-brown till is exclusively in Cluster 2 while grey is in both Cluster 1 and 2. Grey-brown till's closer association with grey till supports its location as the lower transition till. The higher sand content clusters likely have a more prominent Precambrian shield material source. Brown till is spread across all clusters including the red till dominated Cluster 3, supporting its stratigraphic location as the upper transition till and blending Precambrian and Paleozoic material provenance. Incorporation of sand and gravel lenses/beds could also increase grain size of some samples.

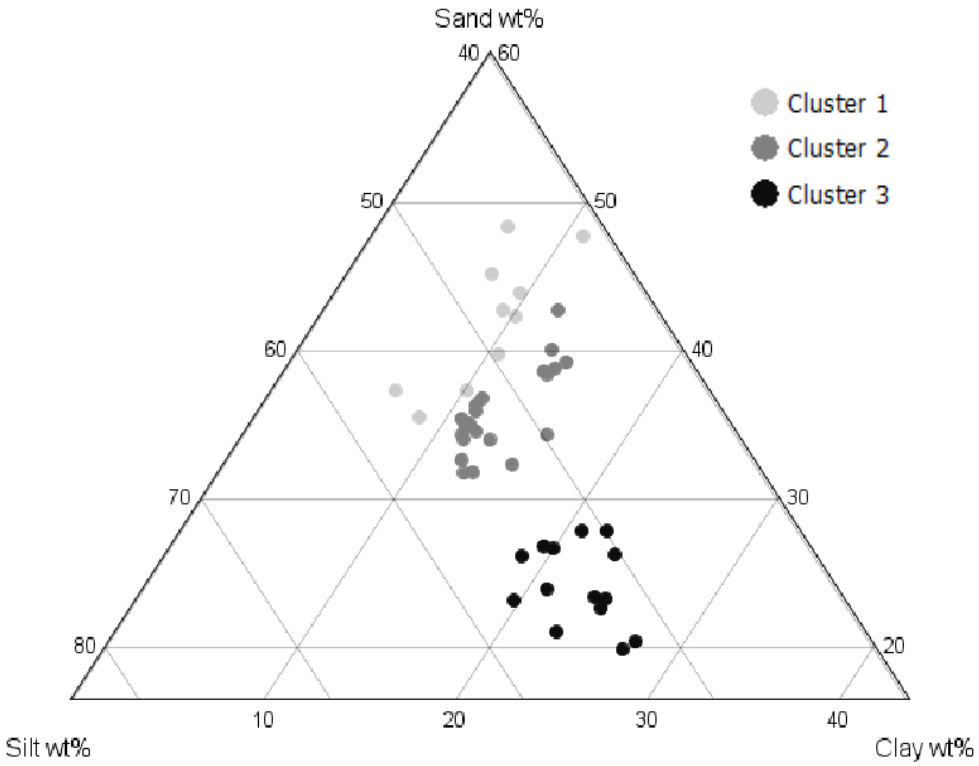


**Figure 12: Scale adjusted ternary plot of PSA using weight % showing the distribution of PSA clusters. The clay threshold between Clusters 2 and 3 is wide from 16 – 18 wt %, between Clusters 1 and 2 is tight at 10.9 wt % with two samples inverted.**

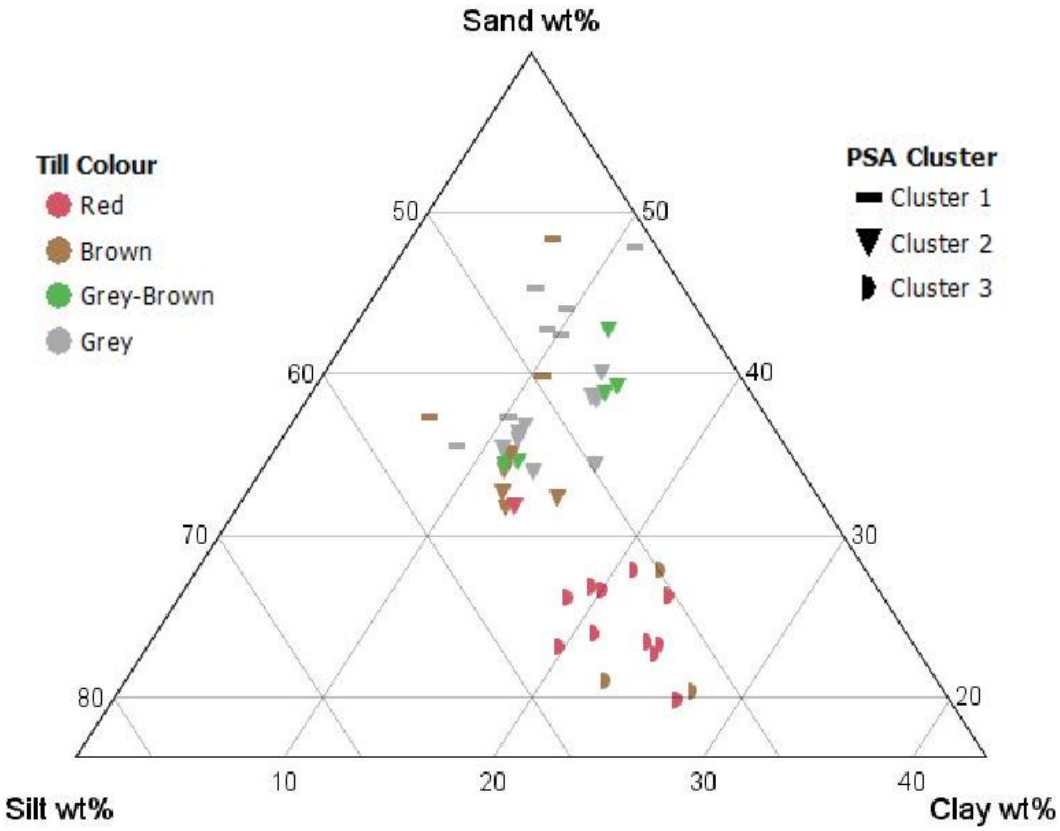


**Figure 13: Scale adjusted ternary plot with PSA results by colour and cluster. Red till dominates Cluster 3 with high clay. Grey-brown till is exclusively in Cluster 2 while grey is in both Cluster 1 and 2. Grey-brown till's closer association with grey till supports its location as a lower transition till. Brown till is spread across all clusters including the red till dominated Cluster 3, supporting its stratigraphic location as an upper transition till.**

### 2.3.3 Clast Fabrics and Striae

A total of 14 clast fabrics were deemed to have a clear preferred orientation (strong fabric) as discussed in section 2.2.4. See **Clast Fabrics** for tabulated statistics of the clast fabric data. **Table 3** tallies the count by till colour in relation to the number of fabrics completed and striae found on boulders within till units and on basal pavements. Basal pavement clast striae were present across three pavements at two bluffs, one for each colour. Boulder striae were found at four different bluffs distributed across several units. **Figure 15** compiles all striae and fabric data by till colour. Broad trends include an up-bluff increase in fabric strength and a down-bluff increase in boulder striae with pavement striae limited by the presence of pavements. Some fabrics indicate a northward flow. This is believed to be the reverse of the actual paleo ice flow direction (discussed in section 2.2.4).

Limited interpretation is made on striae or fabric data as it is inconsistent in distribution with a dominance of pavements in the lower tills and clast fabrics in the upper. However, a slight shift

is seen from grey, through grey-brown, to brown till, and finally a range from SE to SW in red till fabrics. This is consistent with the shift in glacial ice movement on a regional level as discussed in Chapter 1, with the late Winisk Ice Stream moving southward and here represented by the red till.

**Table 3: Count of fabrics by till colour increasing upward in the stratigraphy.**

| Till Colour | Clast Fabrics Completed | Clast Fabrics with S1 ≥ 0.54 | Boulder Striae | Basal Pavement Clast Striae |
|---|---|---|---|---|
| **Red** | 12 | 5 | 0 | 0 |
| **Brown** | 11 | 6 | 1 | 3 |
| **Grey-Brown** | 6 | 2 | 2 | 4 |
| **Grey** | 10 | 1 | 4 | 3 |

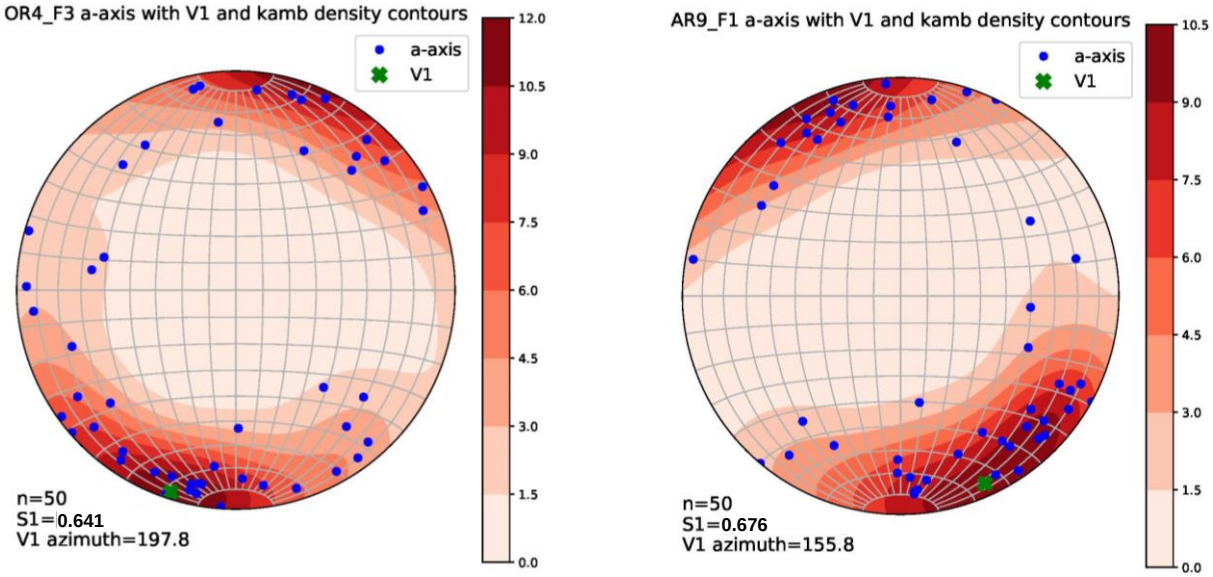


**Figure 14: Stereonets with V1 and kamb density contours from a red till (left, OR4) and brown (right, AR9) showing a clear preferred orientation.**

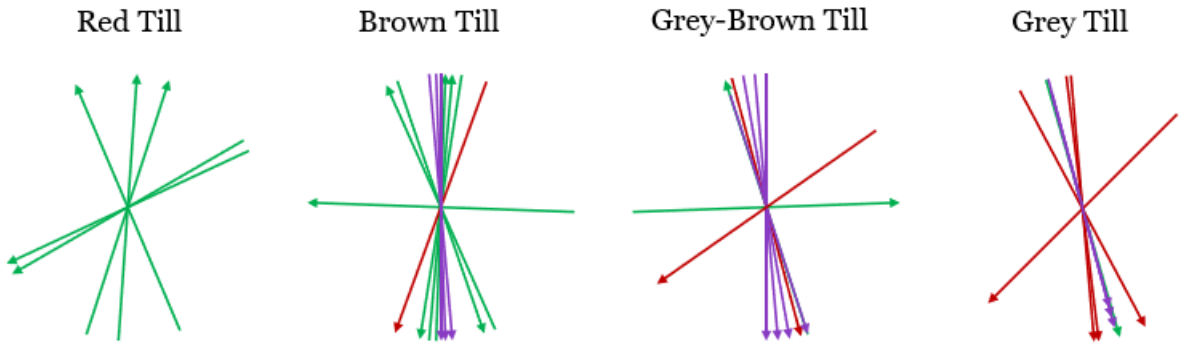


**Figure 15: All direction indicators organized by till colour. Clast a-axis fabrics are in green, mid unit clasts are in red, and striae on clasts within pavements are in purple. Several fabrics show a northward flow which is interpreted to be reverse of actual.**

**Figure 16: Striated clasts (left) and boulder pavements at the top of grey units (right, marked by black arrows) at AR5.**

### 2.4 Summary

From sediment colour, the stratigraphic sequence from bottom up is grey, grey-brown, brown, and topped by red till. Grey till is the lowest till with a strong association to the sandier Cluster 1 and 2 from the PSA and the most south-eastward striae indication. Grey-brown is the next till in sequence with an exclusive presence in the middle grain size, transitional Cluster 2. The middle grain size cluster is closer to the sand cluster than the clay end member. This supports the many characteristic commonalities between grey and grey-brown till such as high compaction, blocky fissility, and lower stratigraphic position, as well as striae direction toward the SSE. Brown till is spread across all grain size clusters supporting its upper middle position and transitional sediment characteristics that appear intermediary between the lower grey/grey-brown tills and upper red till. Finally, the red till is distinct in both its loose compaction, upper position, high clay content, and common silt lensing.

# Chapter 3. Till matrix geochemistry and clast lithology counts

## 3.1 Introduction

This section will summarize the methods and results of till matrix geochemistry and clast lithology count analysis that are essential to interpret sediment provenance. This will be integrated with the initial sequence discussed above based on sediment characteristics, completing objective 1 by developing a stratigraphic framework and glacial history interpretation for the project area. This will then be summarized and integrated with the regional stratigraphic framework and glacial understanding (objective 2) in Chapter 5.

## 3.2 Methods

### 3.2.1 Clast Lithology Counts

#### Lab Processing

From the SSTC processing discussed in section 2.2.2, a ~250 g extraction was taken from the ≥8.0 mm fraction for clast lithology counts. If 250 g of material was not available in the ≥8.0 mm fraction the difference was collected from the ≥1 - <8.0 mm fraction. Sieve weights for the upper size class were only recorded as a total ≥1.0 mm fraction without a separate ≥8.0 mm weight recorded. For till samples, 250 g was on average 7.8% of the ≥1.0 mm fraction with a minimum of 3.2% and maximum of 16.8%. The average for the two sand/gravel samples was 5.2% with minimum and maximum values of 1.3% and 9.1% respectively.

#### Grouping and Provenance Implications

Variations in clast lithologies between till samples indicates material dispersal from different bedrock sources, which can be useful for determining provenance. Clast lithology counts were completed on the ~250 g clast extraction from the ≥8.0 mm fraction for all samples. Excluding glaciofluvial samples, there was a total raw clast count range of 87 – 219 with an average count of 146. Given the bedrock setting, the proportion of Precambrian/Shield and Paleozoic rocks is the simplest starting point for provenance analysis. However, specific subgroups of the shield and Paleozoic lithologies provide more provenance clues than others throughout the HJBL (Dredge and McMartin, 2011; Hodder et al., 2017; Gao et al., 2020). **Table 4** summarizes the grouping of different lithologic classes into simplified categories while **Figure 18** shows the bedrock provenance of the various lithologies.

Subgroups of the Precambrian lithologies are predominantly granitoids (Shield Granitoids (SG)), greywackes, and greenstones. Metasediments and greenstone lithologies dispersed through this study area are likely derived from the Paleoproterozoic Belcher Group or Sutton Inlier to the northeast (Stott et al., 2010; Gao et al., 2020) or greenstone belts within the Canadian Shield to the southeast or northwest. However, there are inliers of pillow basalts that exist to the north of the study area as close as 8 km to the NE of Ogoki to the upper reaches of the Ekwan River (Sanford et al., 1968). These outcrops are small and likely produced minor clasts entrained in till. Given the unreliability in distinguishing greywackes and greenstones with a limited ability to infer provenance from them, a class of “undifferentiated greenstones and greywackes” (UGG) (Hodder et al., 2017; Gauthier et al., 2019) was used unless a clear lithology could be identified. On average, 6% of fine-grained dark shield rocks could be identified per sample so were grouped with UGG in final processing. Of note are red oolitic jasper ironstones or other ironstones, originating from the Kipalu Formation in the Belcher Group (Jackson, 2013) and exposed in the Sutton Inlier as well (Stott et al., 2010). Ironstones are distinctive with a known source but are only present in 11 samples with an average of one clast. In post processing they were grouped with UGG as they indicate a comparable provenance from the northeast.

Subgroups of the Paleozoic platform rocks are important to identifying till provenance, especially the red lithologies. The middle member of the Silurian Kenogami River Formation has red lithologies of carbonates and sand/siltstones (Sanford et al., 1968; Gao et al., 2020). Green Paleozoic clasts are also from the middle member of the Kenogami Fm and have a red mottling appearance, however only 10 clasts were identified from 8 samples. Green Paleozoic clasts were grouped with other Paleozoic platform rocks. Given the specific provenance link of the red lithologies (Red Paleozoics (RP)) and enough present, they remain ungrouped with other Paleozoic Platform (PP) lithologies. There are two occurrences of Kenogami FM at surface, distally to the northwest along Hudson Bay and proximal to the east.

Unknown and other lithologies (schists, cherts, quartzites, etc) were sorted but no distinctive erratics were identified. They are of minor percent overall with an average of 0.8% per sample, no further work or grouping was investigated in this category (Other).

**Table 4: Major groupings and detailed sub-lithology classes for till clast counts.**

| Major Group | Subgroups |
|---|---|
| Paleozoic Platform (PP) | Carbonates |
| | Green Sandstones (Green/Red Mottled) |
| Red Paleozoic (RP) | (with or without fossils) |
| Shield Granitoids (SG) | |
| Undifferentiated Greenstones and Greywackes (UGG) | Greenstones |
| | Greywackes/Metasediments |
| | Mafic Intrusives |
| | Ironstones |
| Other | Chert |
| | Conglomerate |
| | Sandstone & Quartzite |
| | Schist |
| | Unknown |

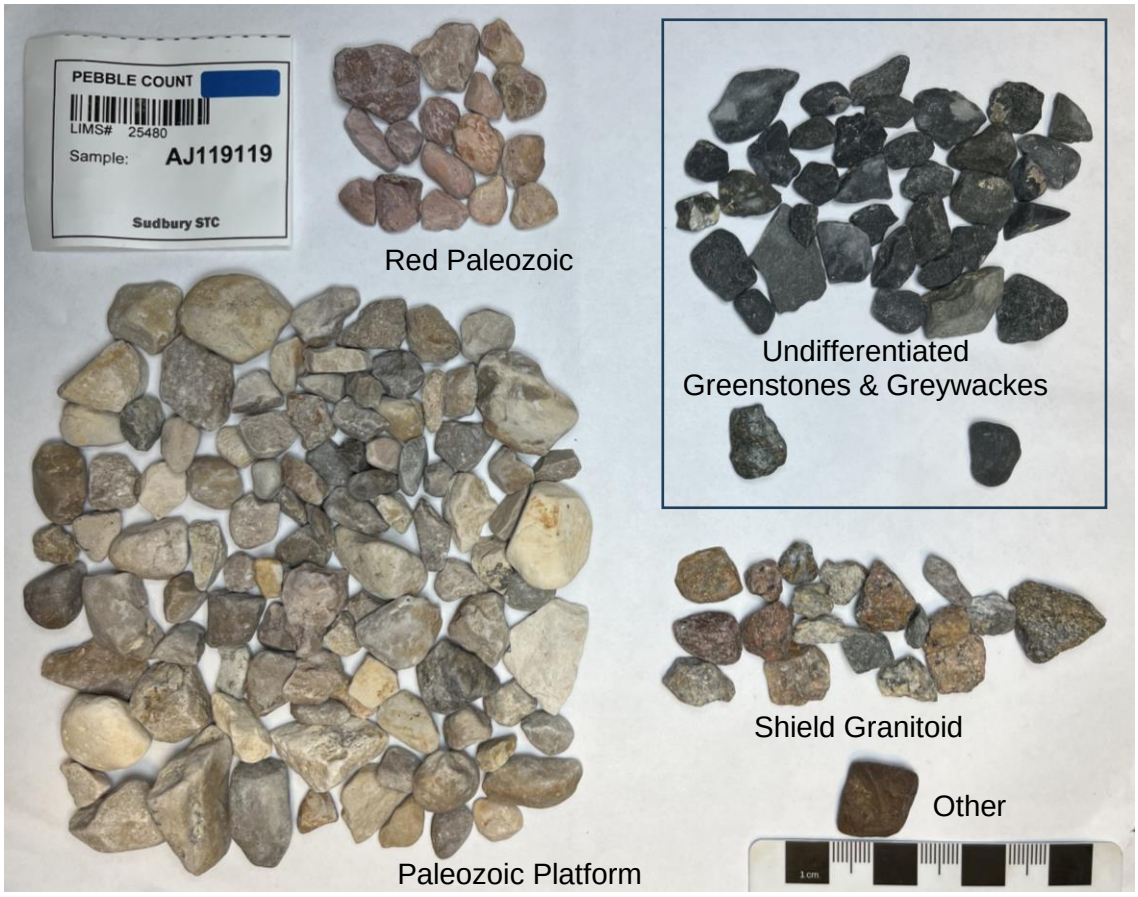


**Figure 17: Clast lithologies typically seen in a clast lithology count with groups attributed.**

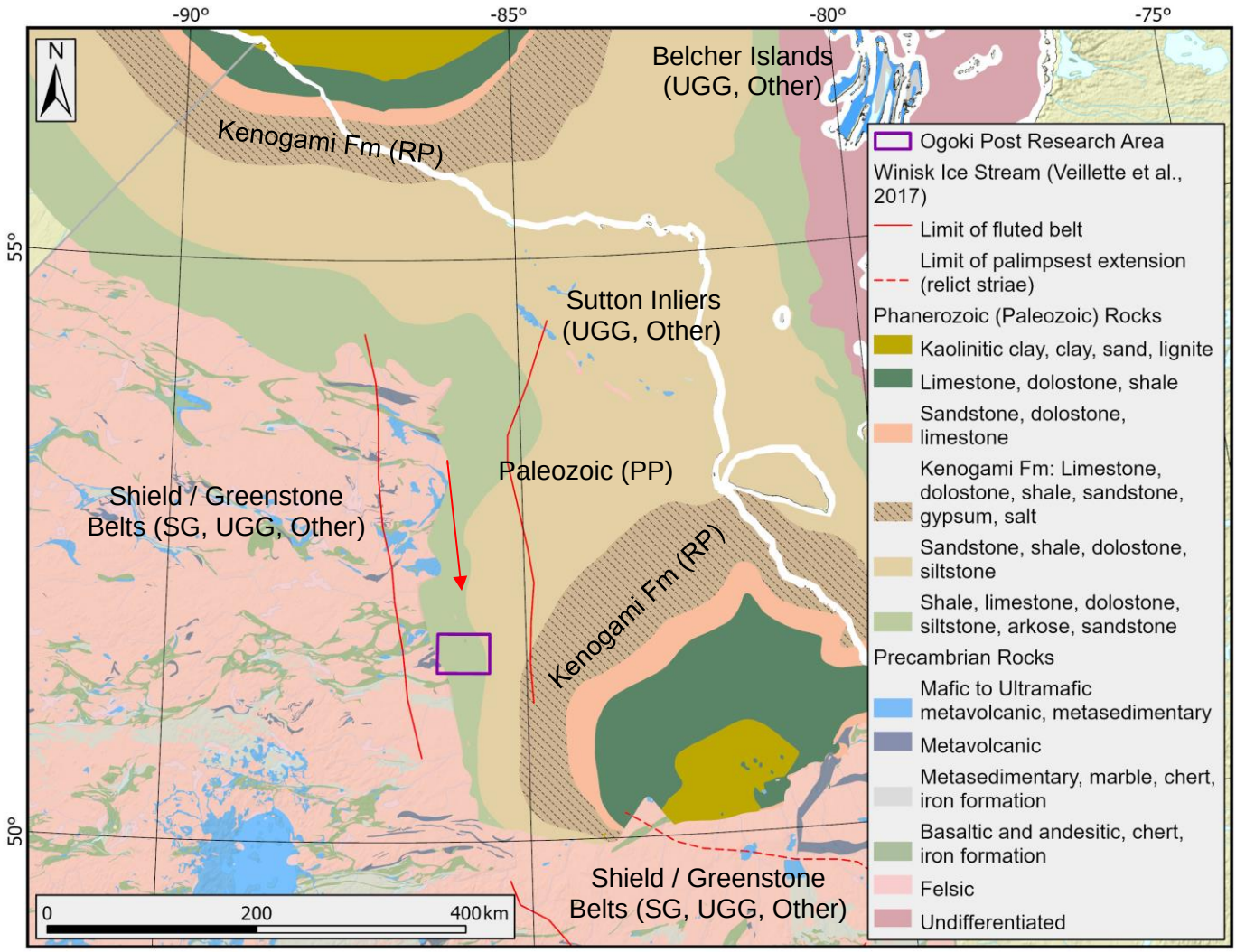


**Figure 18: Bedrock geology of North America and Ontario (2005; 2011) with the provenance of key lithologies marked. The source of PP clasts is restricted to the platform. The Belcher Islands, Sutton Inliers, and greenstone belts and Precambrian Shield will be potential sources for UGG and Other, Precambrian Shield for most SG, and the Kenogami Formation for RP clasts.**

### Analysis in ioGAS

Clast counts were analyzed using ioGAS 7.4.2. Counts of zero were replaced with 0.65 before a CLR transformation was done in ioGAS prior to PCA analysis. The number of K-means clusters was determined from a scree plot of the sum of squares and delta from the CLR data. Results are analyzed using biplots and box plots. The results of the PCA have been scaled using the RQ-mode approach (Grunsky, 2010). This allows plotting scaled PC scores (e.g., PC1 becomes RQ1) and PC elemental loadings in the same space on the same figure.

### 3.2.2 Till Matrix Geochemistry

The SRC conducted four analyses on the samples; Ca/Mg, ICP Total Digestion, ICP-MS Total Digestion, and ICP-MS Partial Digestion (Appendix D: Laboratory Results). Ca/Mg digests 0.5 g of pulp overnight in 2 ml of HCl at room temperature (SRC, 2024). Total Digestions for ICP and ICP-MS heat 0.125 g of pulp in ultrapure $HF/HNO_3/HClO_4$ until dry and then dissolves it in dilute, ultrapure $HNO_3$ (SRC, 2024). Finally, ICP-MS Partial Digestion digests 0.5 g of pulp for one hour in 2.25 ml of ultrapure HNO3:HCl (8:1) at 95˚C (SRC, 2024). No field duplicates were collected, or standards submitted, but during analysis the lab completed three standards (DCB01) and two lab duplicates. This results in ~10% QA/QC material in the sample set which is low but within the recommend 5 – 20% by Piercey (2014).

#### Standards

The analytical precision (reproducibility and repeatability) was reported as relative standard deviation (%RSD) and accuracy (trueness of a value) as the percent relative difference (%RD) of the three standard analyses according to Piercey (2014) and Jenner (1996).

Till matrix geochemistry had an average %RSD of 2.05% and a range of 0.00 – 10.19% which is within acceptable precision of %RSD less than 10%, except for Be at 10.19%. The RD% averaged 3.88% with 7 elements not accurate at values greater than 10%. One of these was MnO and so was removed from the interpretation of the oxides.

#### Duplicates

The average coefficient of variation ($CV_{avg}$(%)) was calculated on the two duplicate samples to determine precision (Piercey, 2014). $CV_{avg}$(%) values have an average of 2.4% and range of 0.0 – 33.3%. There are five elements (Cd, Nb, Se, Be, W) that are above the recommended 7.5% for analytical duplicates and are imprecise (Piercey, 2014), with two elements being below detection limit (Ge, Ta). These elements will not be used for interpretations.

#### Analysis in ioGAS

Analysis was performed in ioGAS 7.4.2 using centered-log ratio transformed (CLR) values for the oxides, no trace elements were analyzed. Data analysis included probability plots, box plots, and biplots (PCA) according to practices detailed in Grunsky (2010) and others to highlight variability (Jolliffe and Cadima, 2016; Abdi and Williams, 2010). The results of the PCA have been scaled using the RQ-mode approach (Grunsky, 2010). This allows plotting scaled PC scores (e.g., PC1 becomes RQ1) and PC elemental loadings in the same space on the same

figure. The number of k-means clusters was established at four based on a scree plot of the sum of squares distances from the CLR data using the 'elbow' method. A PCA was performed on the CLR transformed values.

## 3.3 Results

### 3.3.1 Clast Lithology Counts

Bar graphs were generated from the normalized data with samples in stratigraphic sequence for visualization and can be found in Appendix A. Raw clast count values are in Appendix C. Paleozoic Platform (PP) clasts dominate with a normalized average of 56% across all samples. This is followed by Undifferentiated Greenstones and Greywackes (UGG) at 30%. Shield Granitoids (SG), Red Paleozoic (RP), and Other are 8%, 3%, and 2% respectively. Four lithology clusters were identified during ioGAS analysis.

Cluster 1 is defined by elevated proportions of RP clasts with no overlap of other clusters (**Figure 19**, **Figure 20**) and a clear alignment to the red till (**Figure 21**) and therefore clay dominated (PSA C3). Cluster 1 has a notable lack of UGG and Other clasts compared to Clusters 2, 3, and 4, supporting a largely different material provenance. The bedrock source for the RP clasts is the Kenogami Formation, which lies ~70 km to the east of the study area or to the north ~450 km. This suggests either dispersal during the Cochrane surge from the east or dispersal from the north during the WIS.

Cluster 2 has the next clearest provenance signal defined by elevated SG and PP clasts (**Figure 19**, **Figure 20**). While low compared to Cluster 1, it has elevated RP clasts compared to cluster 3 and 4. Brown till dominates Cluster 2 but is present in all clusters, indicating a mixed material provenance sourced from both the NE and N. The presence of even some RP clasts suggests a southern ice flow but the SG and PP dominance indicates material inheritance from the underlying tills during the southward flow, prior to the dominance of RP clasts in red till dominated cluster 1.

Clusters 3 and 4 are the closest aligned, being UGG and Other clast dominated with a lack of RP clasts. Where they differ is in the inverse relationship of SG and PP content with a higher SG content in Cluster 3 and higher PP content in Cluster 4 (**Figure 20**). Grey till spans both Cluster 3 and 4 whereas the grey-brown till aligns closely with Cluster 3. However, there is a high degree of overlap between the two till colours in both clusters. SG clasts are mostly cherts and quartzites (36% normalized), potentially from the Sutton Inliers and/or Belcher Islands to the northeast, a source of UGG and Other as well (Hawley, 1925; Sanford et al., 1968; Stott et al.,

2010). An alternate source of SG specifically, as well as UGG and Other clasts, could be from the Precambrian Shield either proximally to the west or distally to the east and southeast.

Elevated RP clasts of cluster 1, a lack of UGG, and spatial constraint of the corresponding red till to the western bluffs of the study area suggests a northern material provenance. Brown till dominates Cluster 2 with high SP and PP and slightly elevated RP clasts but is present through all other clusters as well. The slight presence of RP clasts suggests a northern source with the high SP and PP clast content indicating prominent material inheritance from the underlying till units. Dominant UGG and Other clasts with a lack of RP clasts in Clusters 3 and 4, dominated by grey and grey-brown tills at the stratigraphic base, suggests a northeast provenance of the Sutton Inliers and Belcher Islands with an SG source from either the northeast Inliers/Belcher Islands or the Precambrian Shield from several directions.

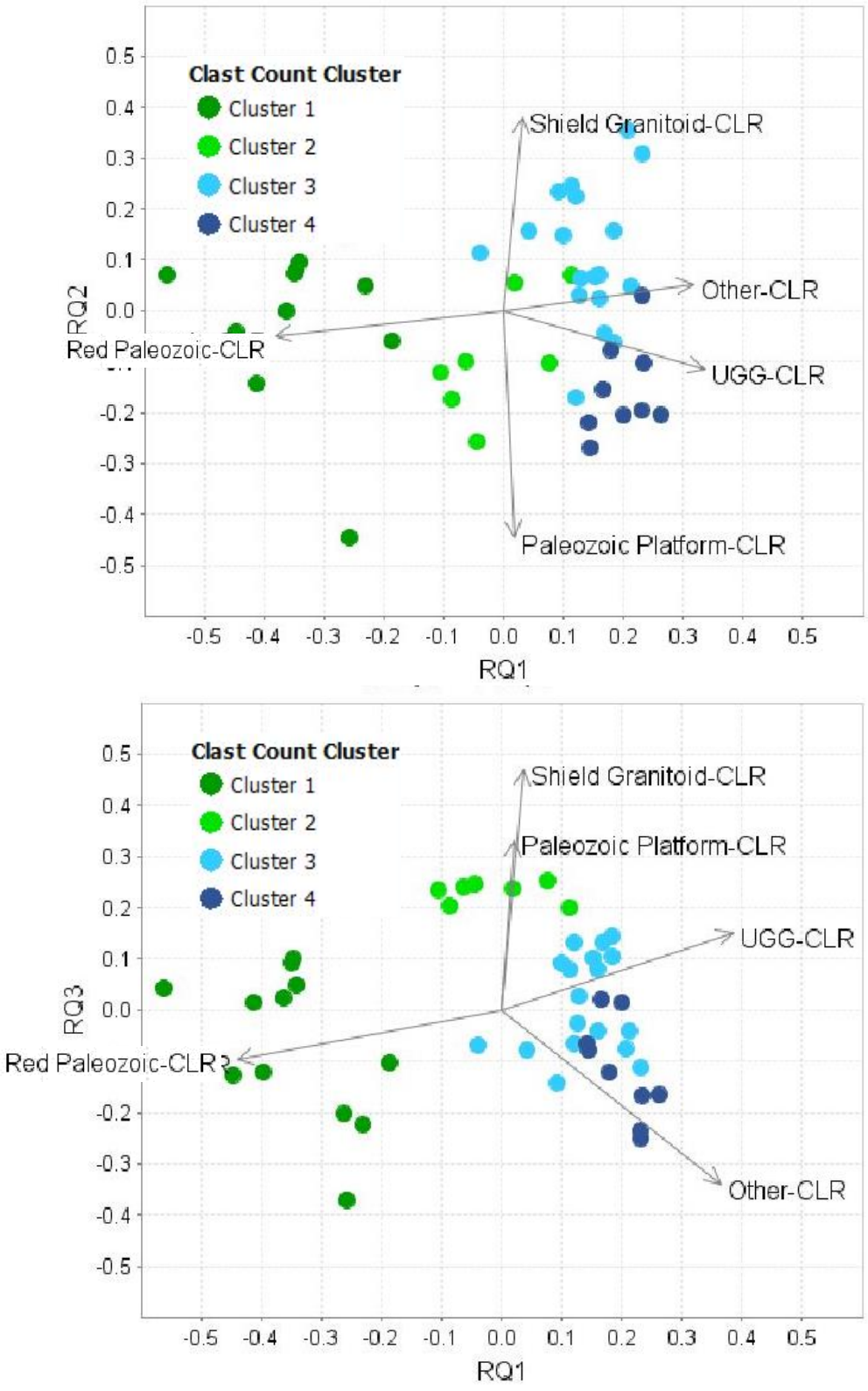


**Figure 19: Biplot of RQ1 vs RQ2 (above) and RQ1 vs RQ3 (below) showing four clusters of clast counts. Cluster 1 is defined by RP. Cluster 2 is most controlled by PP given its higher degree of influence between the two plots. Clusters 3 and 4 are dominated by UGG and Other but do invert between the plots based on the PP vector.**

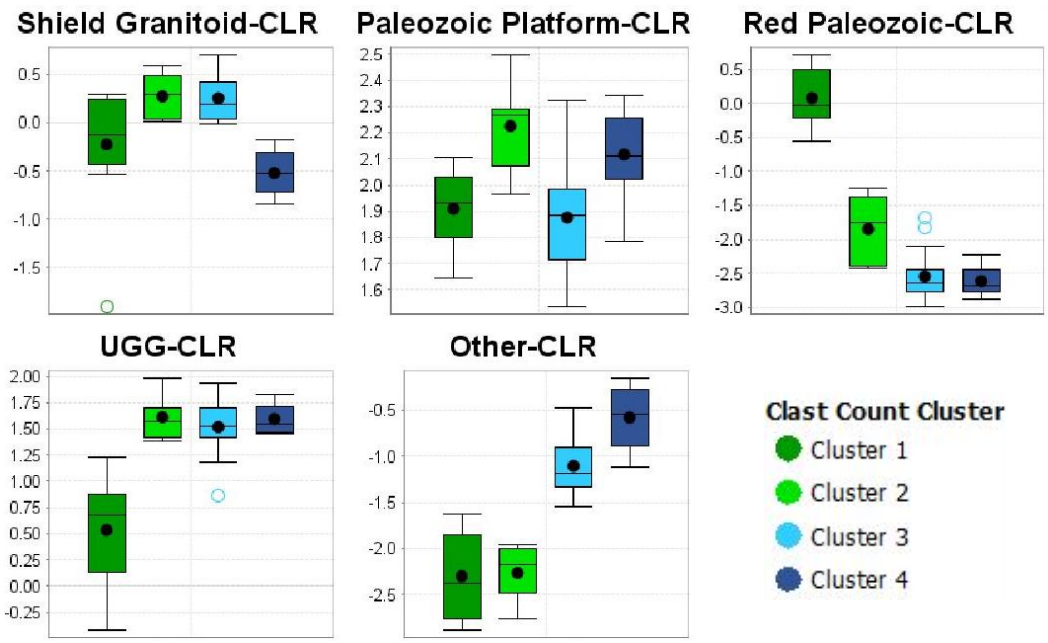


**Figure 20: Box plots of each cluster by clast lithology group demonstrating the distinct RP signature of Cluster 1 from the rest. Relatively high UGG dominates clusters 2, 3, and 4 with the overlapping 3 and 4 having Other lithologies dominate.**

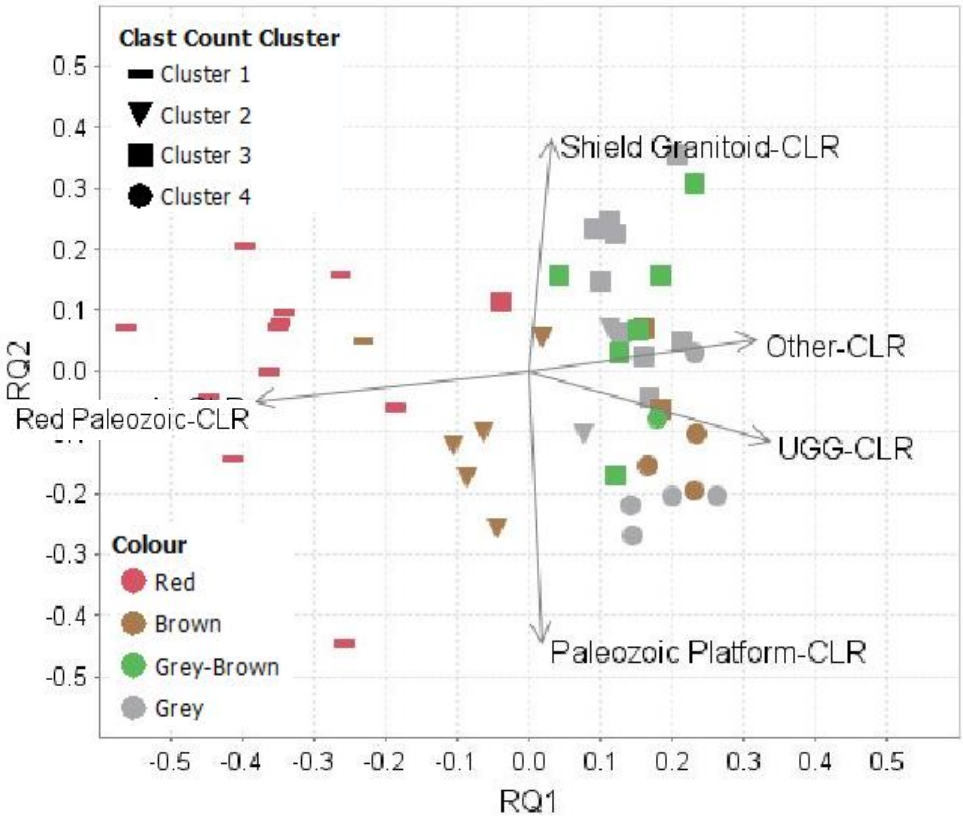


**Figure 21: RQ1 vs RQ2 biplot with clast count clusters (shape) by till colour (colour) showing the strong association of red till to RP clasts (Cluster 1) and a dominance of brown till in Cluster 2 (PP). Cluster 3 and 4 are seen to have a high degree of overlap among the grey, grey-brown and some brown till.**

### 3.3.2 Till matrix Geochemistry

The number of k-means clusters was established at four based on a scree plot of the sum of squares distances using the 'elbow' method. Samples were symbolized according to the cluster analysis on biplots to understand elemental assemblage associations (**Figure 22**), and also plotted by till colour and clast count cluster (**Figure 23**), and in box plots by oxide (**Figure 24**). Cluster 1 has a higher $Na_2O$ content, Cluster 2 is characterized by a $TiO_2$, $Al_2O_3$, and $Fe_2O_3$ assemblage, Cluster 3 is $K_2O$ dominated, and Cluster 4 has high CaO and MgO. Appendix D: Laboratory Results includes lab analysis information and results.

Cluster 1 is best defined by $Na_2O$ but has the weakest association with any oxide as shown by its central position in the biplots. The RQ1 vs RQ2 biplot indicates an $Na_2O$ and $P_2O_5$ control which is mostly an $Na_2O$ control as $P_2O_5$ is at opposition in the RQ1 vs RQ3 biplot. The trend toward $P_2O_5$ in RQ1 vs RQ2 is more likely an $Al_2O_4$ and $Fe_2O_3$ association, as seen in four of eight oxides in the box plots and RQ1 vs RQ3. This is a felsic/mafic signature with carbonate influence. Cluster 1 is exclusively grey till and always with UGG/Other clast count Cluster 3 and middle to sandy PSA Clusters 2 and 3.

Cluster 2 is defined by a blended mafic and felsic assemblage of $Al_2O_3$, $TiO_2$, and $Fe_2O_3$, as best shown by RQ1 vs RQ2 and the box plots, which also show elevated $P_2O_5$. This element assemblage could also occur under weathering conditions.

Cluster 3 is clear in its $K_2O$ association in RQ1 vs RQ2 with low $Na_2O$. The RQ1 vs RQ3 biplot locates Cluster 3 more centrally indicating a mixed oxide composition which can be seen in the variable association with different clusters in the box plots – aside from the previously discussed $K_2O$ and $Na_2O$ as well as $P_2O_5$. This cluster is strongly dominated by red till and supports a mudstone source in the fine PSA Cluster 3, coincident with the RP clast group and an upper stratigraphic location. RP clasts are interpreted to be derived from the Kenogami Formation. While no lithogeochemistry was found for this bedrock, Nicolas and Armstrong (2017) documented an elevated gamma signature in the middle member. The increased gamma signature could be due to the decay of potassium-40 to argon-40 representing a high potassium content. Another study from the Manitoba Geological Survey (Hodder, 2024) has a site with elevated Kenogami Formation clasts in a $K_2O$ enriched till unit. While tentative, both studies provide supporting evidence for a $K_2O$ association with the Kenogami Formation.

Cluster 4 is distinct with high CaO and MgO, no other cluster is comparable in these oxides. It is at opposition to Cluster 2 across most elements except $Na_2O$, reflected in the box plots. This is likely a carbonate signature indicating entrainment of limestones and dolostones.

Clusters 2 and 4, while at opposition, contain a mix of all till colours. Given the location of the single red till in Cluster 2, it can be attributed to Cluster 3 with high $K_2O$ and matches in all other analysis methods. The two brown tills in Cluster 2 (high $Al_2O_3$, $TiO_2$, and $Fe_2O_3$) are at the top of eastern bluffs, at stratigraphic opposition to the remaining five grey-brown and grey tills in this cluster. In addition to being geochemically distinct, the grey-brown and grey tills in Cluster 2 are stratigraphically isolated to the lowest five till units at AR2. This is attributed to an earlier ice flow event not seen in other bluffs, prior to the pervasive stratigraphic sequence beginning above an erosive and undulous contact.

Geochemistry well identifies the upper stratigraphic, fine, and RP dominated red tills by the high $K_2O$ content associated with the Kenogami Formation. In general, it indicates a mixed geochemical signal for the brown, grey-brown, and grey tills with either high CaO/MgO or $TiO_2/Fe_2O_3/Al_2O_3$ content. However, geochemistry is clear in its distinction of the bottom five till units at the far east AR2 bluff (Cluster 2). This leads to an interpretation of the preservation of an earlier till not recorded in the exposed stratigraphy in the rest of the project area. Cluster 1 is also geochemically distinct but not geographically constrained with four samples spread across the base of four bluffs. For this reason, Cluster 1 was not identified as a separate till phase from geochemistry but certainly could be.

**Figure 23** shows a division of clast count Clusters 3 and 4. Clast count Cluster 4 is dominated by Other clasts but has an exclusively carbonate till matrix signature. Clast count Cluster 3 is UGG/Other dominated with a slightly elevated SG content compared to Cluster 4, and in the till matrix geochemistry is split between the felsic C2 and felsic/carbonate C1. This suggests that while clast count Cluster 3 and 4 are similar, they are at opposition in the till matrix geochemistry between a felsic and carbonate signal. An elevated carbonate signal in the till matrix geochemistry likely indicates prevalent ice movement across the Paleozoic Platform while depletion suggests a modified path that reduces carbonate entrainment and increases felsic material, from the Canadian Shield to the northwest or southeast of the study area.

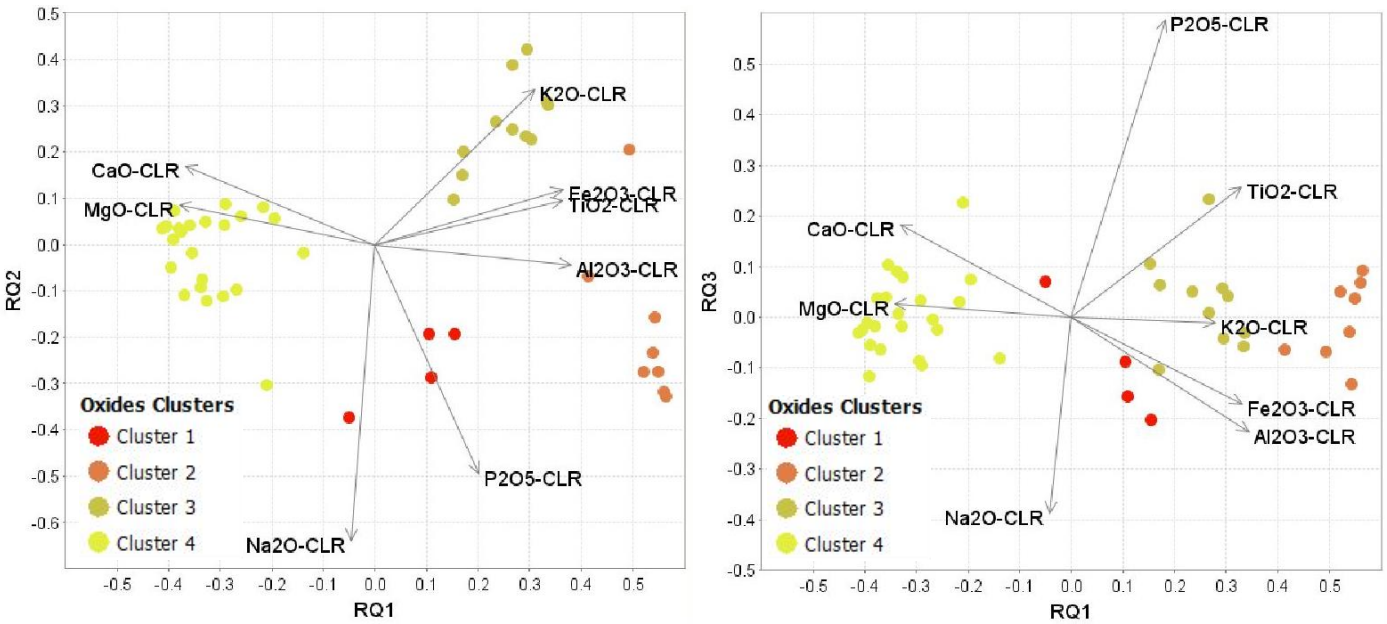


**Figure 22: Biplot of RQ1 vs RQ2 (left) and RQ1 vs RQ3 (right). Cluster 4 has high CaO and MgO content indicative of carbonate material while Cluster 3 has high $K_2O$ content. Cluster 2 has an assemblage of $Al_2O_3$, $TiO_2$, and $Fe_2O_3$ indicating mixed felsic and mafic material entrainment. While dominated by $Na_2O$, Cluster 1 is centrally located along RQ1 indicating a mixed composition of felsic and carbonate material.**

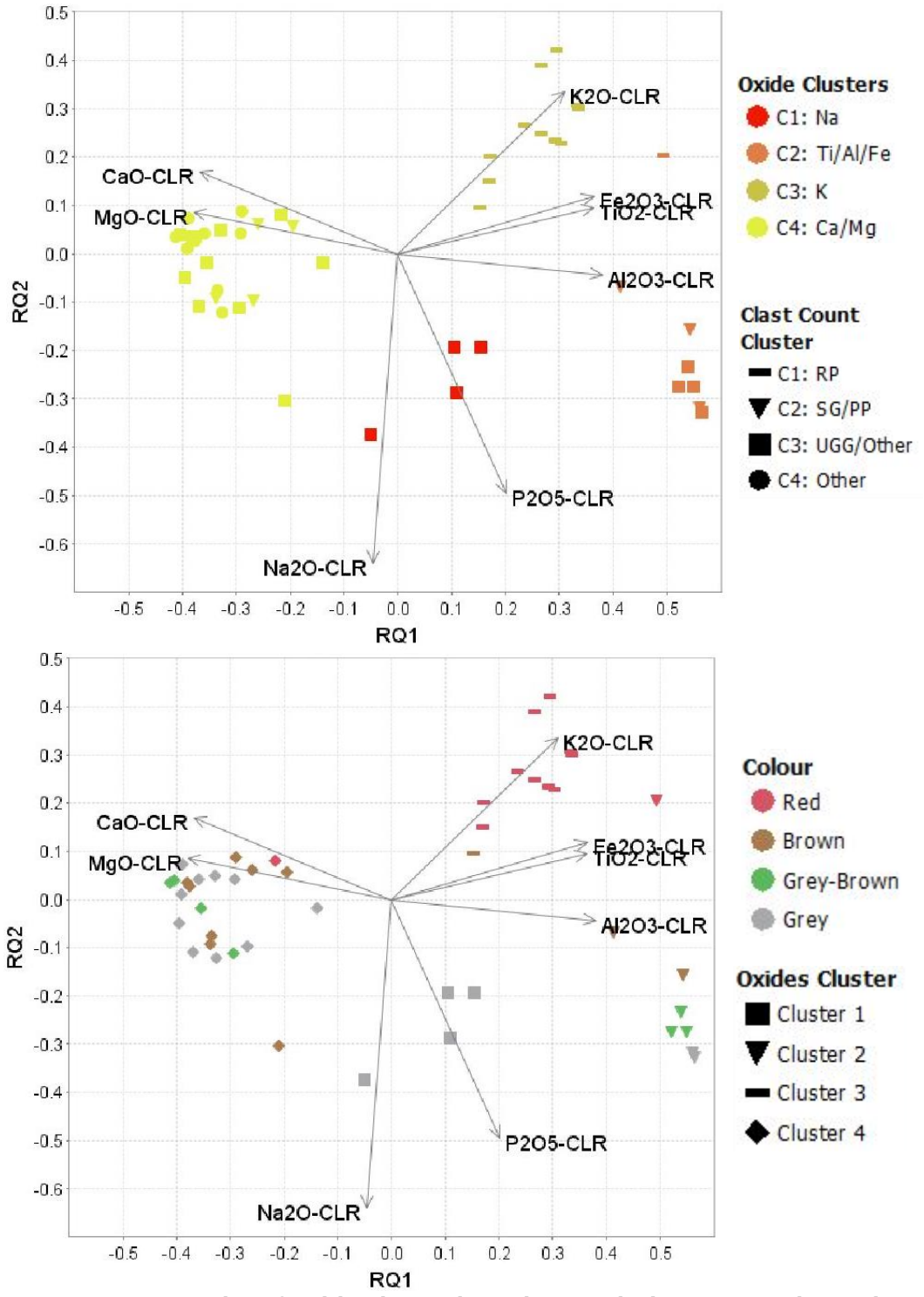


**Figure 23: Top - RQ1 vs RQ2 plot of oxide cluster by colour and Clast Count cluster by shape showing the correlation of oxide Cluster 3 ($K_2O$) with the RP Cluster 1 of clast counts. Oxide Cluster 4 contains a mix of all other clast count clusters while oxide Cluster 1 and 2 are dominated by clast count Cluster 3 (UGG/Other). Bottom - RQ1 vs RQ2 plot with clusters (shape) and till colour (colour). Red till dominates Cluster 3 with a variable spread of the other geochemistry clusters across the till groups. Aside from Cluster 1, which is exclusively grey till located at the base of bluffs.**

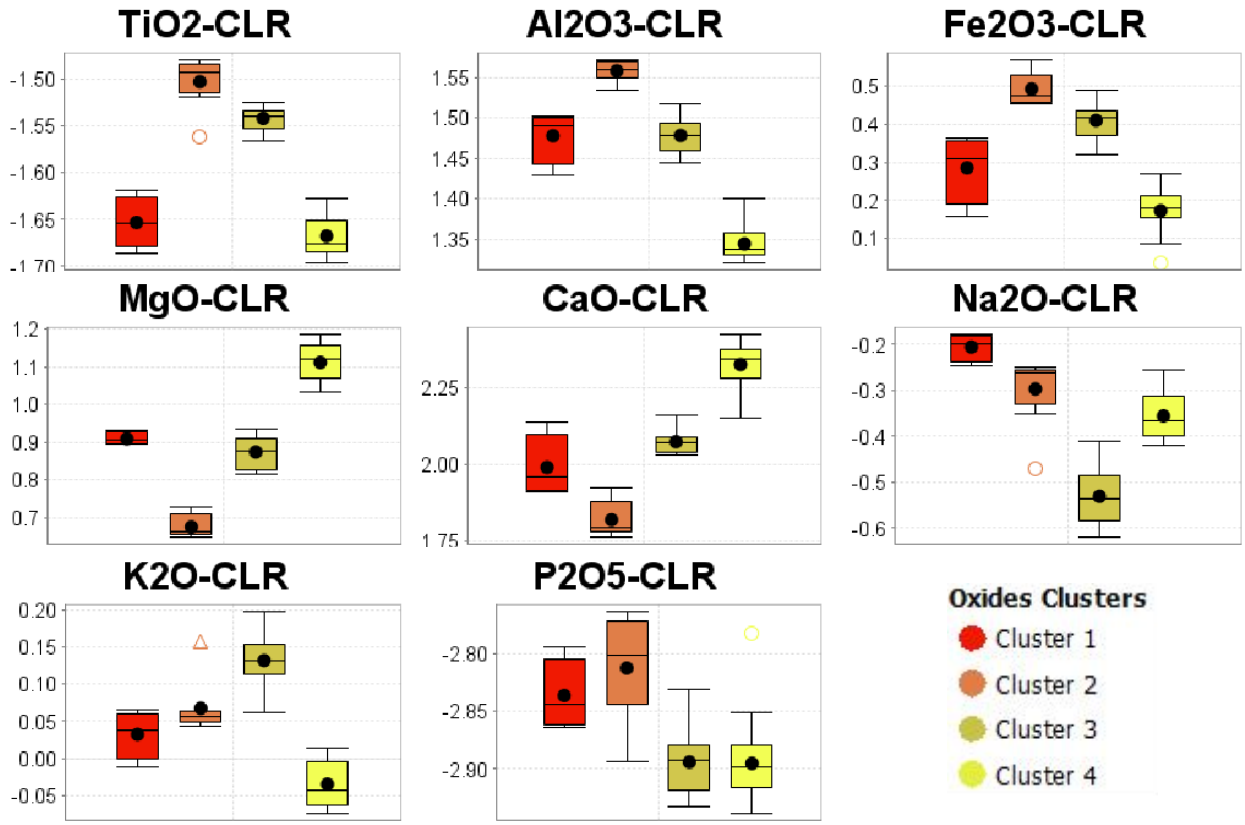


**Figure 24: Box plots of clusters by oxide. Cluster 3 is clear with its high $K_20$ content. MgO and CaO dominate Cluster 4 while Cluster 3 and 4 both have a low $P_2O_5$ control. Cluster 1 is poorly defined by any element except elevated $Na_2O$, although closely associated with Cluster 2 which shows dominance in $TiO_2$, $Fe_2O_3$, and $Al_2O_3$.**

### 3.4 Summary

Discussion in Chapter 2 developed a bottom-up stratigraphic sequence of grey till, grey-brown, brown, through red till based on observed sediment characteristics, ice flow indicators, and particle size results. Adding clast count and geochemistry analysis and integration adds material provenance interpretation in support of the prior discussed sequence.

The till matrix geochemistry overlaps the brown, grey-brown, and grey tills with opposing carbonate (CaO/MgO) or $TiO_2/Fe_2O_3/Al_2O_3$ signal, with a blended $TiO_2/Fe_2O_3/Al_2O_3$ and carbonate cluster (cluster 1 of high $Na_2O$) of four grey till samples lowest in the stratigraphy (Cluster 1).

However, the bottom five grey-brown and grey till units at the far east AR2 bluff are well-defined by $TiO_2/Fe_2O_3/Al_2O_3$ in the till matrix geochemistry (Cluster 2) and UGG/Other clast lithologies (Cluster 3), as well as slight SG clast elevation. This leads to an interpretation of the preservation of an earlier till not recorded in the exposed stratigraphy in the rest of the project

area with an ice flow direction crossing less of the Paleozoic Platform and more of the Canadian Shield. This could result from an early Q-L Sector flow from the southeast to northwest prior to the ice center shifting northward which would entrain northeastern Ontario and western Quebec Canadian Shield rock. Or it could be from a later Q-L Sector phase sourcing Sutton Inlier and Belcher Island lithologies but does not quite account for the slightly elevated SG clasts. Either path includes ice flow across the Paleozoic Platform to account for PP clast entrainment, but a southeast provenance has the least PP exposure and could account for the relatively low PP clasts in this unit. There is one a-axis clast fabric in these tills trending E-W which supports a provenance from the east or southeast. If so, RP clasts would be expected but is not the case. Further understanding of the Kenogami Formation lithologies sourced from the different basins could explain the absence of RP clasts. However, even with the lack of RP clasts a southeast provenance of Cluster 2 is preferred to explain the low PP, high UGG/Other, and elevated SG clasts with a strong $TiO_2$, $Fe_2O_3$, and $Al_2O_3$ signal in the geochemistry. Another option is a south-southeast moving Keewatin Sector ice flow event prior to the buildup of the Q-L Sector, entraining Shield rock from the northwest of the study area. This is not the preferred interpretation as Keewatin Sector ice is not anticipated to have reached as far south as the study area. Alternately, an assemblage of $TiO_2$, $Fe_2O_3$, and $Al_2O_3$ could occur because of prolonged weathering. In this case, Till 1 could be a much older till that has been preserved and extensively weathered.

There are other grey and grey-brown tills with high UGG/Other clast lithologies that cluster geochemically with a high carbonate till matrix (Cluster 4), indicating an ice flow path that crossed the Paleozoic Platform. These are attributed to the Q-L Sector of the LIS radiating across the HJBL.

The upper stratigraphic, fine, red till has a distinct provenance signature defined by elevated red carbonate clast content and high $K_2O$ in the till matrix. This provenance signature is interpreted to be a result of higher incorporation of Paleozoic siltstones, shales, and red carbonates of the Kenogami Formation from the north during deposition by the WIS.

While the brown till is variable in oxide cluster, it includes overlap with red till geochemistry, some RP clasts, and variable sediment characteristics that the grey-brown and grey tills do not have. This supports a comparable ice flow direction of the overlying red till with strong material inheritance and mixing of the underlying grey and grey-brown tills. This indicates brown tills deposited between red and grey-brown/grey tills to an early N-S flow of the WIS with prevalent material inheritance resulting in a till matrix signature comparable to the grey/grey-brown tills. As

the WIS progressed through time the northern material source became dominant, resulting in further brown till mixing and eventually the distinct red till signature.

This concludes the first objective of analyzing sediment and provenance characteristics to understand unit relationships and changes in the depositional environment through time.

# Chapter 4. Stratigraphic Framework

## 4.1 Ice Flow Phases

The stratigraphic sequence of grey till at the base, through grey-brown, brown, and red till is well established with various datasets as previously discussed. This chapter will use the stratigraphic columns in their relative position with the major oxides, PSA, and clast count clusters shown on top in block form with directional indicators as arrows (**Figure 25**). While arrows are unidirectional, they are treated as bidirectional for previously discussed factors (Section 2.2.4). **Figure 26** shows correlations of individual till units using all datasets and regional knowledge into ice flow phases (labeled Till 1, 2, etc.) resulting in a stratigraphic framework for the study area. This identifies the number, relative age, and direction of ice flow phases to achieve objective 2 and allow for the subsequent correlation to other regional glacial studies. For phase differentiation colours are used. Note that the phase colour does not always reflect the field identified till colour unless it was dominant in that phase and chosen to represent it.

The first ice flow phase produced Till 1 and is apparent in several datasets but most prominently in geochemistry and only observed in the far east bluff (AR2). It is the earliest phase exposed in the project area consisting of grey and grey-brown coloured tills. It is dominated by UGG clasts and an elevated SG clast content derived from greenstone belts and crystalline rock respectively. There are multiple interpretations for this phase:

1. It is a north-northwest phase of the Q-L Sector prior to the sector center shifting north. It sourced SG clasts from the east/east-southeast in Ontario and Quebec and UGG/Other clasts from the greenstone belts within the same SG source. This interpretation lacks an explanation for no RP clasts given the extensive mapped Kenogami Fm to the east.
2. A second interpretation is a southwest phase sourcing the Sutton Inliers and Belcher Islands for UGG and Other clasts after the Q-L Sector shifted north. This northeast source doesn’t account for the elevated SG content compared to later phases over comparable material.
3. A third option is a south-southeast moving Keewatin Sector ice flow event prior to the buildup of the Q-L Sector, entraining Shield rock from the northwest of the study area. This is not the preferred interpretation as Keewatin Sector ice is not anticipated to have reached as far south as the study area.

4. Alternately, an assemblage of $TiO_2$, $Fe_2O_3$, and $Al_2O_3$ could occur because of prolonged weathering which is masking the provenance signature in the oxides. In this case, Till 1 could be an older till of unknown provenance that has been preserved and extensively weathered. Analysis of the trace elements could provide insights to the provenance of this till.

Till 2 is a phase defined by the compact, UGG clast rich, grey till event. It is present at all bluffs and frequently overlain by a clast pavement. Pavements are well preserved along the Albany River. However, along the Dark and Ogoki Rivers the pavements are absent with a late deglacial phase (discussed below) directly overlying Till 2, suggesting a more erosive setting which would have stripped the pavement and transitional tills. Till 2 was deposited during Q-L ice movement from the northeast to southwest. However, ice direction indicators are north-south trending. This could be due to increased basal roughness of the Canadian Shield rock and resulting local ice deflection to the south over the smoother Paleozoic Platform. The Canadian Shield with crystalline rocks is a rougher surface, increasing friction with overriding ice, whereas the carbonate surface of the platform would provide a smooth, low friction surface for ice to move over. Till 2 includes geochemistry Cluster 2 which is unique in its carbonate and felsic blending and high $Na_2O$ which are located at the base of several bluffs. The high $Na_2O$ cluster is not identified as its own phase, but very well could have been.

The third ice phase predominantly consists of grey-brown, compact, sandy till with moderate fissility. Some brown tills with similar geochemistry (Cluster 4) and clast lithologies (Cluster 3) are included, two of which are above gradational contacts with a lower grey-brown till. These gradational contacts are interpreted as later stages of the same ice phase. Till 3 overlies preserved clast pavements above Till 2 in the east with a lack or preservation in the middle of the study area along the Dark and Ogoki Rivers where Till 3 was likely eroded away during later phases. It is present in the western Albany River bluffs with an apparent pinch out in the west. Given the similarity to Till 2, Till 3 is attributed to a late Q-L Sector ice phase of the LIS originating from the northeast and flowing southwest with a similar deflection as Till 2 within the study area.

The next ice flow phase deposited Till 4, containing exclusively brown till aside from one red till at OR2 which lacks the high RP and $K_2O$ signature. Till 4 lacks fissility and has a higher PP clast content than Till 3. It is predominantly in the far west of the project area on the Albany River, with the brown till at OR3 likely correlated to it based on the presence of RP clasts with fossils, although other characteristics are not as consistent. Due to the changed sediment

characteristics, PP clast clustering, and presence of RP clasts, Till 4 is attributed to an initial ice phase of the south flowing WIS with high material inheritance of the underlying tills and preservation in the west. It was largely eroded from the Ogoki River bluffs during the main WIS ice phase.

This brings us to Till 5 which is defined by red till colour with high $K_2O$ content and RP clasts originating from the Kenogami Formation in the north. Abundant RP clasts in conjunction with N-S trending surface streamlined landforms indicate this phase was moving NNW to SSE, and so part of the main WIS phase. It has a strong presence in bluffs to the west and south-central project area, but not in the east. This could indicate the eastern boundary of the WIS is not as far east as Veillette et al. (2017) indicate, however this is unlikely given the prevalence of surface flutings. Till 5 could have been eroded from the eastern bluff sites but it is more likely that it was not deposited given there is no subsequent ice flow phase with enough duration or extent to be highly erosive.

Finally, there is a late phase that deposited Till 6 with high PP clast content, felsic till matrix, and sediment characteristics that separate it from Till 5 (high RP content, $K_2O$ dominated). While geochemically clustering with the felsic Till 1, it is clay rich with a high PP clast content (Cluster 2). While Till 6 is not a part of the main WIS phase, it could be a late deglacial WIS surge as ice retreated from the area with limited extent and material dispersal with a slight direction offset to account for increased felsic material in the matrix. A lack of the Till 5 signature in Till 6 could be due to a weaker ice stream and more local provenance as well.

The stratigraphic location of the glaciofluvial unit at AR9B positions it below Till 2. However, there is no stratigraphic control with Till 1 to indicate if it is before or after the earliest ice flow phase. The undulous upper contact of Till 1, also lacking a clast pavement, could indicate an erosive surface. On this basis, the glaciofluvial unit is interpreted to have been deposited above Till 1 and then eroded away.

**Figure 27** demonstrates the correlations discussed above by plotting the till samples by ice flow phase on the PSA ternary (top left), clast count biplot (top right), and geochemistry biplots (bottom).

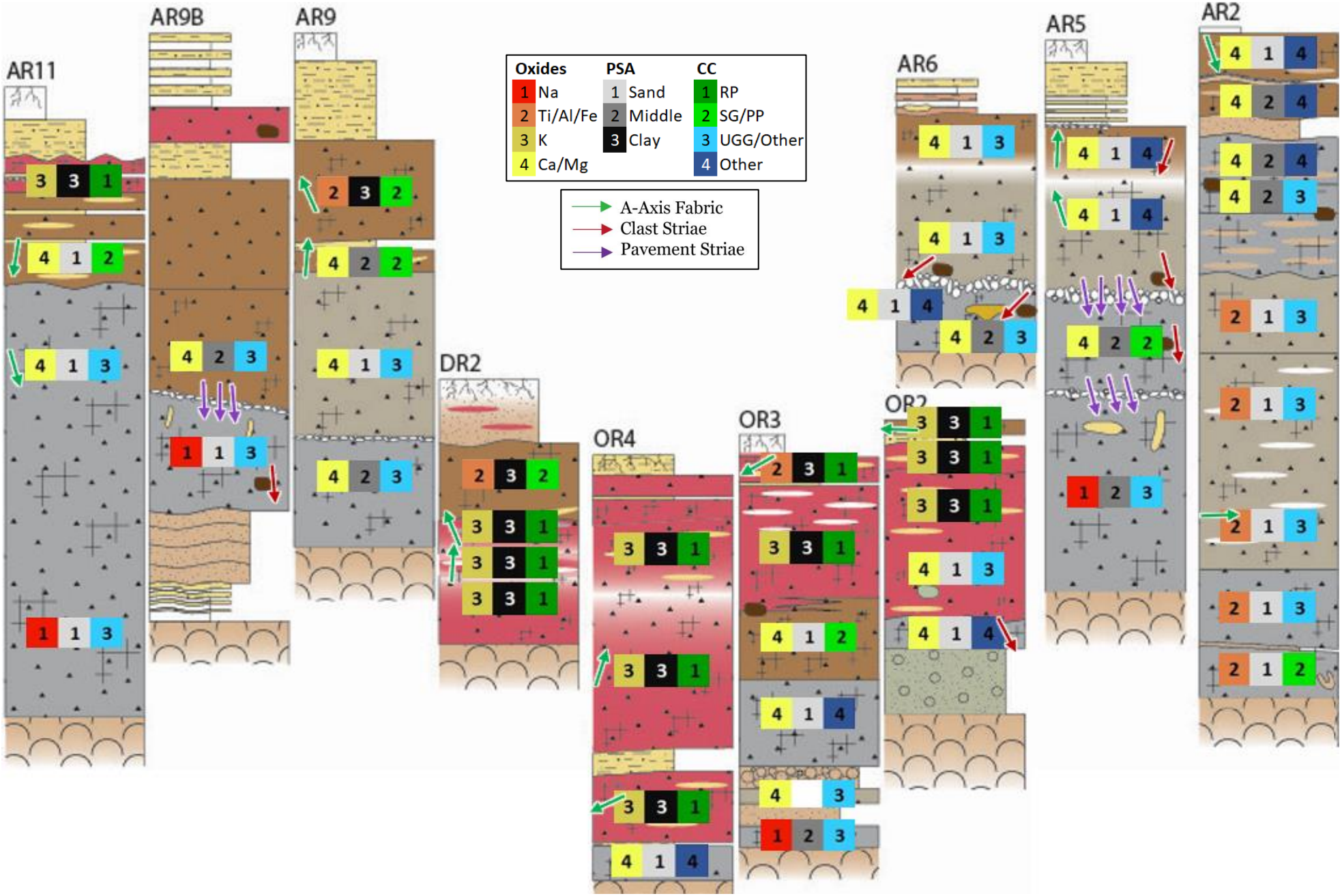


**Figure 25: Stratigraphic columns in relative location (heights to scale, distances not to scale). Dataset clustering per sample site is overlain in block form by colour and number.**

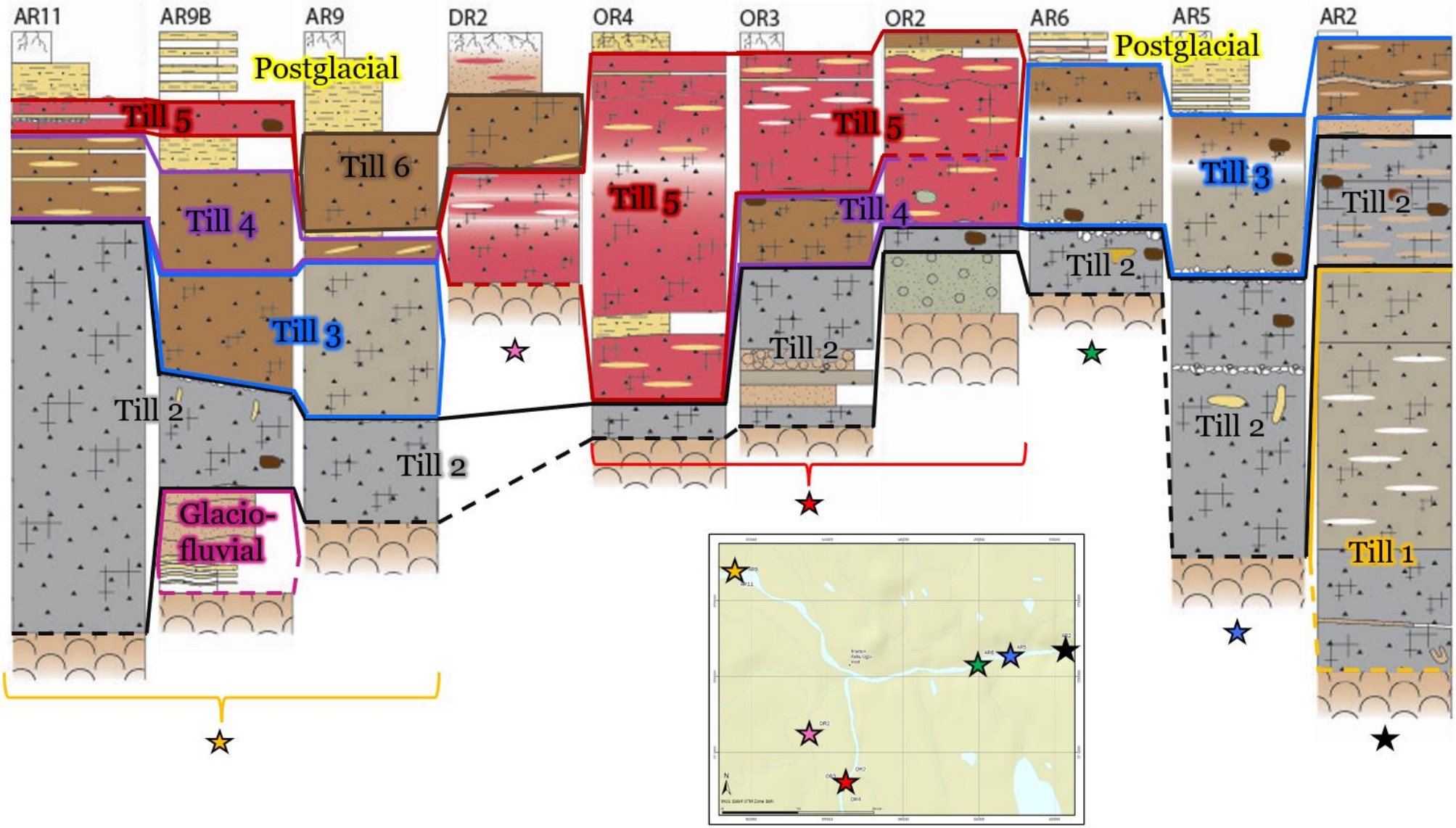


**Figure 26: Stratigraphic columns with correlation of ice flow phases. Bluffs are displayed in order west to east with heights to scale. Inset shows the location of bluffs in the project area. Till 1, 2, and 3 have similar characteristics and are attributed to the LIS. Till 4, 5 and 6 are attributed to the WIS with RP clasts. Till 4 has some characteristics of the underlying tills but the presence of RP clasts indicates a northern provenance and transitional composition.**

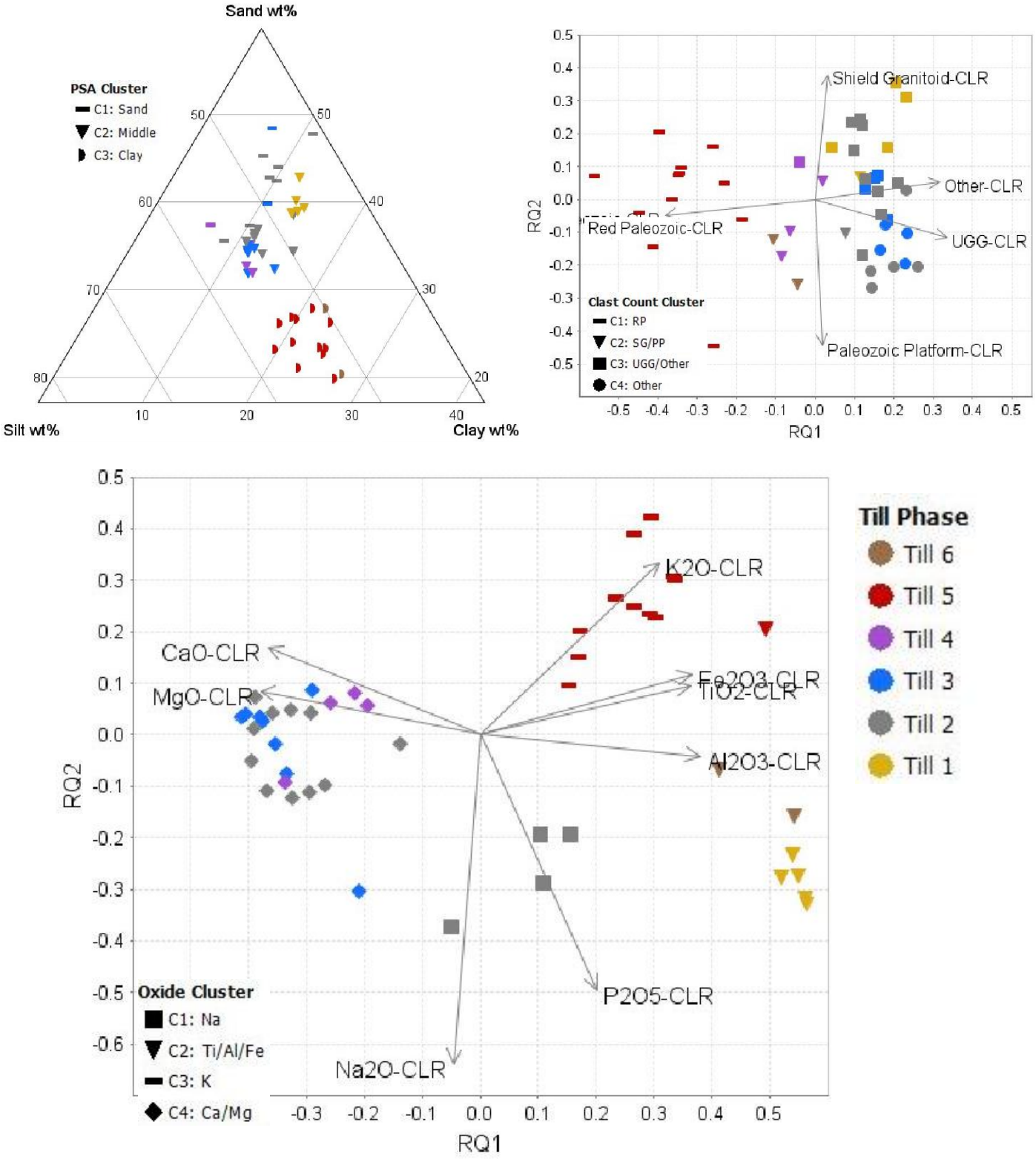


**Figure 27: Till samples by ice flow phase on PSA ternary (top left), clast count biplot (top right), and till matrix geochemistry biplots (bottom).**

### 4.1 Stratigraphic Framework Summary

The late evolution of the LIS through the late WIS is preserved within the study area (**Figure 28**). Till 1 is primarily interpreted to be an early westward flow while the Q-L Sector was at its southern extent sourcing SG and UGG clasts from the Canadian Shield prior to PP entrainment. It could be a later ice phase with northeast provenance from the Belcher Islands and Sutton Inliers. However, these interpretations do not account for a lack of RP clasts or elevated SG clasts respectively. A third interpretation could be that Till 1 was deposited in a much earlier LIS phase and was extensively weathered to create a $TiO_2$, $Fe_2O_3$, and $Al_2O_3$ signal.

Till 2 records a pervasive Q-L Sector phase that is highly compact, southwest flowing, and widespread. Finally, the late Till 3 was deposited with mixed characteristics, SW ice flow, and more limited spatial distribution. While Till 2 and Till 3 flowed to the southwest, N-S trending ice flow indicators suggest a deflection to the south on the Paleozoic Platform due to a higher basal roughness in the Canadian Shield causing an ice buildup.

Till 4, 5, and 6, record phases of the WIS from early development through to a late surge, all trending south/south-southeast. Till 4 is a relatively early phase of the WIS with some RP clasts and prominent incorporation of previously deposited tills. Till 5 is the main WIS phase with limited inheritance of the underlying tills as indicated by a distinct combination of fine particle size, red colour, RP clast provenance from the north, and north-south surface flutes. Till 6 directly overlies Till 5 at two bluffs but provenance indicators and limited spatial extent suggest it is a separate phase of ice movement. It is interpreted to be a late WIS surge with a more local Shield source from the north-northwest as the WIS waned.

This concludes the reconstruction of ice flow phases within the study area as part of research objective two. Chapter 5 will address the final part of objective two, the integration of identified ice flow phases with the existing stratigraphic framework from other regional studies.

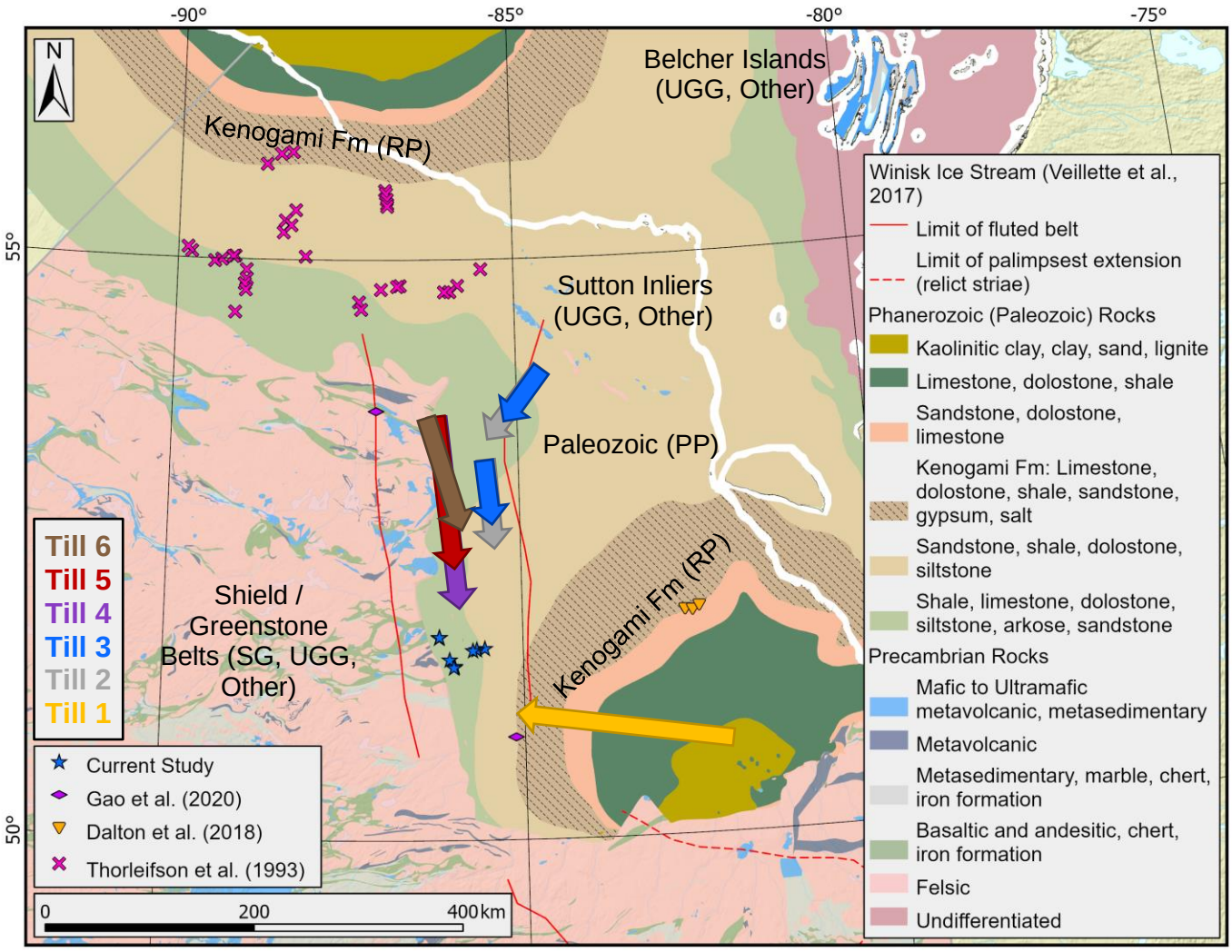


**Figure 28: Bedrock geology of Ontario (2011) with the provenance of key lithologies and till phase interpretation and regional studies used in correlations. Till 1 has several interpretations (see text), only the primary is displayed here.**

# Chapter 5. Regional Stratigraphic Correlations

## 5.1 Correlations

As discussed in Chapter 1.3, correlations across the expansive and glacially complex HJBL are prone to oversimplification and should be considered with caution. Variability in factors such as till deposition rates, bedrock sources, and dispersal distances make correlations challenging with decreased confidence as distance between studies increases. Regardless, this chapter will make regional correlations (**Table 5**) with studies by Thorleifson et al. (1993), Dalton et al. (2018), and Gao et al. (2020) which will imply correlations to other studies (Skinner, 1973; Nielsen et al., 1986) originally shown in **Table 1**. This will complete objective two by comparing and correlating ice flow phases of the local stratigraphic framework to existing regional knowledge (**Figure 6**).

Consistently among the three prioritized studies is a sequence of till units overlying an interglacial unit, the Fawn River Sediments (Thorleifson et al., 1993), Webequie Non-glacial Sediments (Gao et al., 2020), and the unnamed unit on the Albany River (Dalton et al., 2018). Based on stratigraphic location, the nonglacial unit seen regionally could correlate to the interglacial sediments observed at the base of AR9B with unknown depth extent.

It is plausible that Till 1 was deposited prior to the interglacial sediments with the interglacial material since eroded, leaving an undulous contact. This is a lithostratigraphic correlation based on regional descriptions of tills below the interglacial sediments as there is no stratigraphic control between the interglacial material and Till 1 in this study. Depending on interpretation, Till 1 could therefore correspond to the Rocksands Till or an earlier till. If related to a Q-L ice phase, it would correspond to the Rocksands Till and lowest 2 tills on the Albany River given the grey colour and elevated Precambrian clasts. It is primarily interpreted to be of an east provenance, which is supported by the single a-axis clast fabric direction indicator available.

The sequence above the interglacial sediments is comprised of three till units in each regional study. Starting at the base is the Sachigo Till (Thorleifson et al., 1993), which transitions from a grey lower material (Proterozoic rich, E-W ice flow) to red upper material (red carbonates, SE ice flow). The lower portion of this unit corresponds well with the lower till on the Winisk River farther east (Gao et al., 2020) and the grey phase of this study with high UGG clasts and ironstones, indicating a SW ice flow. The variance in ice flow direction is due to their relative position within the LIS and basal roughness variance between the Paleozoic Platform and Canadian Shield boundary (**Figure 4**). While sediment characteristic descriptions are not as

detailed for the eastern Albany River, Till 3 would be the corresponding till at that site with its dark grey colour (Dalton et al., 2018). It is unclear what caused the upper Sachigo Till to shift direction and obtain red carbonate clasts not seen in other studies, perhaps a function of regional radiation patterns or a local advance of the Keewatin Sector to account for the SE flow direction (Thorleifson et al., 1993).

The Severn Till does not correlate well with the second till at each of the other sites given the high red carbonate content. However, this till also has high Proterozoic clasts, is grey in colour, and has a SW ice flow direction (**Figure 25**). Again, due to the spatial reach of this study to the north and this till's location along the Severn River, it is likely that the red clasts were locally integrated from the Kenogami Formation without enough entrainment time to alter the colour of the till. It is therefore concluded that this till does correlate with the second till unit at other studies and this study's Till 3. The colour of these tills does vary and seems to correlate with the underlying presence of sand, which would locally lighten the till from grey.

This leaves the upper most till, the Winisk Till (Thorleifson et al., 1993). This till is variable between brown and red in colour with a N-S ice flow direction from surface streamlined landforms, high red carbonate clast content, and clast fabrics. Its presence in the east of Thorleifson et al. (1993) and at Gao et al. (2020) sites is within the WIS boundary delineated by surface flutings (Veillette et al., 2017). It corresponds to Till 4, 5 and 6 of this study. Till 4 does not correspond as well with its sandy nature so is interpreted to be associated with the early WIS but of high material inheritance, giving its variable signature. However, it is comparable to other second till units so the possibility it is a late phase of the Severn Till instead of Early WIS is not ruled out.

Both Till 5 and 6 are correlated to the top till unit of both Winisk River studies and therefore the WIS. It is unclear if the highest till at Dalton et al. (2018) is its own till phase, or perhaps a later phase of the till beneath. It is well outside the boundaries of the WIS and so not a WIS phase. Perhaps it is a late Cochrane surge or otherwise local deglacial event not observed in this study. In a similar manner, the ice phase depositing Till 6 is likely a late WIS event that was short in duration and limited in extent to the Ogoki River area.

**Table 5: Stratigraphic correlation table modified from Table 1 and reduced to Thorleifson et al. (1993), Gao et al. , and Dalton et al. (2018). Correlations are made using sediment characteristics, ice flow indicators, and stratigraphic position as consistently as possible. The grey row is an interglacial bed.**

| MIS | Thorleifson et al. (1993) Winisk River | Gao et al. (2020) Winisk, Little Current Rivers | Dalton et al. (2018) Albany River | This study Albany, Ogoki, and Dark Rivers |
|---|---|---|---|---|
| 1 | Postglacial Sediments | Postglacial Sediments | Postglacial Marine Sediments | Postglacial Sediments |
| 2 | Winisk Till: brown, in east only, on boulder pavement, N-S flutes and ice flow indicators<br>Amino acid (shells) | Upper Till: 0.3-2 m thick, clayey silt, brownish, high red carbonate clast content, N-S surface flutes | Till 4/5: Nye Channels, finer than below, W-NW ice flow indicators | Till 6: brown, high granitoid and paleozoic platform clasts, clay rich, N-S flutes<br>Till 5: red, red carbonate clasts, clay rich, N-S flutes |
| 2 | | | | Till 4: brown, intermediate clasts, some RP clasts, local sand contacts, sand lensing |
| 2 | Severn Till: grey, moderate Proterozoic, high red carbonate clasts, SW ice flow (flutes, fabrics, boulder straie)<br>Amino acid (shells) | Middle Till: 1.5-2 m, yellowish to light brown, sharp lower unconformable contact with sand.<br>S-SW ice flow (intermediate clast lithology) | Till 4: light grey-brown, massive, low clay content, stratified sediments throughout<br>S-SW flow (striated boulder to 204°) | Till 3: grey-brown to brown, compact, sandy, UGG and other clasts |
| 3/4 | Sachigo Till<br>Upper is red, ice flow (red carbonate clasts)<br>Lower is grey, E-W ice flow (fabric, boulder straie, Proterozoic clasts) | Lower Till: 6 m thick, dark grey, compact, SW flow (high proterozoic argillite and greywacke clasts and jasper ironstones) | Till 3: dark grey-brown, heavily lensed, high clay content | Till 2: grey, highly compact, high Proterozoic UGG clasts and ironstones, SW ice flow |
| 5e | Fawn River Sediments*<br>Paleo-ecological correlation | Webequie Non-glacial Beds<br>OSL on K-feldspar and radiocarbon on wood.<br>Chronostratigraphic correlation | Non-glacial Sediments<br>$^{14}C$ and OSL on Qtz give MIS 3, now attributed to MIS 5 (Hodder et al., 2023) | Interglacial Sediments* |
| 6 | Rocksand Till*: grey, NW-SE (fabric), WNW (striae, landforms), Proterozoic rich, red carbonate clast poor<br>Amino acid (shell), TL - negated | | Till 1/2 (Rocksands?): dark grey-brown, S-SW flow (high limestone/dolomitic clasts), high base metals | ^Till 1*: grey, RP and PP poor, mostly UGG rich, E-W ice flow (fabric), undulous upper contact |
| 6/7 | | | Till 1 (Rocksands?): dark grey, clay/silt rich, N-NW flow (low dolomite/calcite clasts, stone lines, boulder striae), high base metals | |
| 6/7 | Shagamu Till: SE ice flow (red carbonates, local source, therefore not Rocksands Till) | | | ^Till 1*: grey, RP and PP poor, mostly UGG rich, E-W ice flow (fabric), undulous upper contact. **Or earlier till.** |

*No stratigraphic control between units within the study's observed bluff sections.
^Till 1 correlation with Shagamu or Rocksand Till is interpretation dependant.

### 5.2 Regional Correlation Summary

The interglacial sediments can be lithostratigraphically correlated to the Fawn River Sediments, Webequie Non-glacial Sediments, and un-named interglacial sediments. Which in conjunction with sediment characteristics would correlate Till 1 with the Rocksands Till (Thorleifson et al., 1993) and Till 1/2 of Dalton et al. (2018) if it is interpreted to be of the Q-L Sector. It could be an even older till with the geochemistry being a weathering signature which would then correlate it to a pre Rocksands till (Shagamu Till if a Keewatin phase or otherwise).

Till 2 is consistent across studies (the Sachigo Till) with grey colour, high compaction, and Proterozoic clast lithologies (notably ironstones). It does vary in geochemistry by including Cluster 2 (high $Na_2O$) which could be a separate phase.

Till 3 corresponds to the second till unit above the interglacial sediments at other studies (Severn Till, Thorleifson et al. (1993)). It is lighter in colour, likely dependent on sand integration, with variable clasts content. Is it the final phase recorded of the LIS prior to the WIS developing.

This study identifies three tills attributed to WIS phases. Dalton et al. (2018) are outside of the WIS boundaries and so have an unrelated upper till. Other studies identify one Winisk Till with fine material and N-S ice flow direction from surface flutes and other indicators. These tills correspond to Till 5 and 6 of this study, and perhaps Till 4. Till 4 could be a final phase of the Severn Till but is herein interpreted to be an early WIS phase with high material inheritance given its variable traits between surrounding tills and some RP clasts present. Till 6 is a late WIS phase with enough variability to distinguish from Till 5 but is comparable in sediment characteristics and has a lack of spatial extent toward the east.

# Chapter 6. Conclusion

There are three till phases recording the late LIS changes with a further three phases recording the evolution of the WIS preserved within the study area. Till phases attributed to the LIS can be more readily correlated to regional till units whereas the WIS phases do not have the same differentiation in other studies as are seen in this study. There is also an interglacial sediment bed correlated with a known regional interglacial bed that is consistent with the HJBL stratigraphy.

Till 1 has two interpretations from the Q-L Sector (consistent with the current understanding of HJBL ice flow), one from the Keewatin sector, and one based on weathering:

1. A north-northwest phase prior to the Q-L center shifting northward. This is supported by a single east-west clast fabric indicating a source of SG, UGG, and Other clasts from the Canadian Shield and contained greenstone belts. However, it lacks Kenogami Formation clasts located to the east. This interpretation would correlate to the Rocksands Till.
2. A southwestward phase deposited once the Q-L sector had shifted toward the north of Quebec. This would source UGG and Other clasts from the Sutton Inliers and Belcher Islands but is counter to the single clast fabric trending east-west. This interpretation would correlate to the Rocksands Till.
3. A Keewatin ice phase, which requires that Keewatin ice reached farther than is currently thought and would have occurred prior to the Q-L Sector build up and ice advance from the east, correlating it to the Shagamu Till. This is not a likely scenario.
4. If the till matrix geochemistry contains a weathering signature it is potentially masking the provenance signature to some degree. If true then this could represent an even older till of uncertain provenance. Analysis of the trace element suite could provide insights to the provenance of this till.

Ice direction data contains many north-south clast pavements which are not always associated with the overlying till which could be misleading interpretations. A re-sort of clasts may indicate which Q-L phase if focused on differentiating the UGG group, Other which may have diagnostic erratics, and the carbonates for possible Kenogami Fm variability from its northern exposure. Using hyperspectral methods or a more detailed lithology analysis could differentiate UGG clasts that are from the Sutton Inlier/Belcher Islands source versus alternate Canadian Shield locations. Trace elements from the till matrix geochemistry could also indicate sources when

compared with available whole rock geochemistry, including from the Ring of Fire and Victor Diamond Mine as well as the Till 1 potential weathering signature.

Till 2 and Till 3 are both of the late LIS when the Q-L was located in its northern reaches and flowing to the southwest, meaning a provenance source of the Belcher Islands and Sutton Inliers for the high UGG and Other clasts as well as carbonate dominated till matrix geochemistry from the pervasive Paleozoic Platform rocks. Ice direction data to the north-south is attributed to a deflection of ice to the south on the Paleozoic Platform due to the increased basal roughness encountered at the bedrock contact with the Canadian Shield. A slight increase in the elevation gradient onto the shield could also contribute to the deflection to the south. Further geochemistry work could shed light on the blended felsic/mafic and carbonate signature of the $Na_2O$-rich till matrix geochemistry Cluster 1 which is here grouped with Till 2. Like Till 1, it is stratigraphically located at the base of bluffs and geochemically different from other grey tills. Research into the sodium source could indicate if tills of geochemistry Cluster 1 should have been assigned to Till 1, remain with Till 2, or most likely split as a till phase of their own.

Ice deflection along the Shield-Paleozoic boundary matches the development of the WIS in a comparable location once ice thinned. Till 4 represents the initial development of the WIS, during which there was abundant material inheritance from underlying tills and a weak northward provenance signature. The main WIS ice phase is well preserved in the till record of this study area and distinct in characteristics and composition. The final Till 6 represents the end of the WIS and likely a local advance of ice. The presence of the WIS Till 5 is consistent with other studies where the additional two WIS tills could be due to the project's location within the heart of the WIS path and thus recording the initiation (Till 4) and last advnaces (Till 6) of WIS movement.

The presence of three till phases deposited across the HJBL and up to three WIS phases locally in north-central Ontario highlights the complexity of the stratigraphic record. This includes local WIS patterns and variable basal bedrock roughness impacting material dispersal, which is an ongoing complication for mineral exploration in the region. While generally consistent with LIS ice movement understanding in the HJBL, local north-south ice direction indicators with variable other provenance indicators require a deflection of ice along the Paleozoic – Precambrian contact, which is a new hypothesis to be explored further.

# References


Abdi, H., Williams, L.J., 2010. Principal component analysis. Wiley Interdiscip. Rev. Comput. Stat. 2, 433–459. https://doi.org/10.1002/wics.101

Batchelor, C.L., Margold, M., Krapp, M., Murton, D.K., Dalton, A.S., Gibbard, P.L., Stokes, C.R., Murton, J.B., Manica, A., 2019. The configuration of Northern Hemisphere ice sheets through the Quaternary. Nat. Commun. https://doi.org/10.1038/s41467-019-11601-2

Benediktsson, Í.Ö., Jónsson, S.A., Schomacker, A., Johnson, M.D., Ingólfsson, Ó., Zoet, L., Iverson, N.R., Stötter, J., 2016. Progressive formation of modern drumlins at Múlajökull, Iceland: stratigraphical and morphological evidence. Boreas 45, 567–583. https://doi.org/10.1111/bor.12195

Benn, D., 2007. Till Fabric Analysis, in: Encyclopedia of Quaternary Science. Elsevier, Glacial Landforms, Sediments, pp. 954–959. https://doi.org/10.1016/B0-444-52747-8/00093-4

Carr, S.J., Rose, J., 2003. Till fabric patterns and significance: particle response to subglacial stress. Quat. Sci. Rev. 22, 1415–1426. https://doi.org/10.1016/S0277-3791(03)00125-2

Chandler, B.M.P., Lovell, H., Boston, C.M., Lukas, S., Barr, I.D., Benediktsson, Í.Ö., Benn, D.I., Clark, C.D., Darvill, C.M., Evans, D.J.A., Ewertowski, M.W., Loibl, D., Margold, M., Otto, J.-C., Roberts, D.H., Stokes, C.R., Storrar, R.D., Stroeven, A.P., 2018. Glacial geomorphological mapping: A review of approaches and frameworks for best practice. Earth-Sci. Rev. 185, 806–846. https://doi.org/10.1016/j.earscirev.2018.07.015

Clark, C.D., Knight, J.K., T. Gray, J., 2000. Geomorphological reconstruction of the Labrador Sector of the Laurentide Ice Sheet. Quat. Sci. Rev. 19, 1343–1366. https://doi.org/10.1016/S0277-3791(99)00098-0

Dalton, A.S., Dulfer, H.E., Margold, M., Heyman, J., Clague, J.J., Froese, D.G., Gauthier, M.S., Hughes, A.L.C., Jennings, C.E., Norris, S.L., Stoker, B.J., 2023. Deglaciation of the north American ice sheet complex in calendar years based on a comprehensive database of chronological data: NADI-1. Quat. Sci. Rev. 321, 108345. https://doi.org/10.1016/j.quascirev.2023.108345

Dalton, A.S., Finkelstein, S.A., Barnett, P.J., Forman, S.L., 2016. Constraining the Late Pleistocene history of the Laurentide Ice Sheet by dating the Missinaibi Formation, Hudson Bay Lowlands, Canada. Quat. Sci. Rev. 146, 288–299. https://doi.org/10.1016/j.quascirev.2016.06.015

Dalton, A.S., Finkelstein, S.A., Barnett, P.J., Väliranta, M., Forman, S.L., 2018. Late Pleistocene chronology, palaeoecology and stratigraphy at a suite of sites along the Albany River, Hudson Bay Lowlands, Canada. Palaeogeogr. Palaeoclimatol. Palaeoecol. 492, 50–63. https://doi.org/10.1016/j.palaeo.2017.12.011

Dalton, A.S., Margold, M., Stokes, C.R., Tarasov, L., Dyke, A.S., Adams, R.S., Allard, S., Arends, H.E., Atkinson, N., Attig, J.W., Barnett, P.J., Barnett, R.L., Batterson, M., Bernatchez, P., Borns, H.W., Breckenridge, A., Briner, J.P., Brouard, E., Campbell, J.E., Carlson, A.E., Clague, J.J., Curry, B.B., Daigneault, R.-A., Dubé-Loubert, H., Easterbrook, D.J., Franzi, D.A., Friedrich, H.G., Funder, S., Gauthier, M.S., Gowan, A.S., Harris, K.L., Hétu, B., Hooyer, T.S., Jennings, C.E., Johnson, M.D., Kehew, A.E.,

Kelley, S.E., Kerr, D., King, E.L., Kjeldsen, K.K., Knaeble, A.R., Lajeunesse, P., Lakeman, T.R., Lamothe, M., Larson, P., Lavoie, M., Loope, H.M., Lowell, T.V., Lusardi, B.A., Manz, L., McMartin, I., Nixon, F.C., Occhietti, S., Parkhill, M.A., Piper, D.J.W., Pronk, A.G., Richard, P.J.H., Ridge, J.C., Ross, M., Roy, M., Seaman, A., Shaw, J., Stea, R.R., Teller, J.T., Thompson, W.B., Thorleifson, L.H., Utting, D.J., Veillette, J.J., Ward, B.C., Weddle, T.K., Wright, H.E., 2020. An updated radiocarbon-based ice margin chronology for the last deglaciation of the North American Ice Sheet Complex. Quat. Sci. Rev. 234, 106223. https://doi.org/10.1016/j.quascirev.2020.106223

De Beers Group, 2019. Superior Glacial Processing Summary.

Dredge, L.A., Cowan, W.R., 1989. Quaternary Geology of the Southwestern Canadian Shield., in: Quaternary Geology of Canada and Greenland. Geological Survey of Canada, Ottawa, Canada, pp. 214–235.

Dredge, L.A., McMartin, I., 2011. Glacial stratigraphy of northern and central Manitoba (No. 600). Geological Survey of Canada. https://doi.org/10.4095/288561

Dredge, L.A., Nielsen, E., 1985. Glacial and interglacial deposits in the Hudson Bay Lowlands: a summary of sites in Manitoba. Geol. Surv. Can. Paper 85-1A, 247–257.

Dubé-Loubert, H., Roy, M., Allard, G., Lamothe, M., Veillette, J.J., 2013. Glacial and nonglacial events in the eastern James Bay lowlands, Canada. Can. J. Earth Sci. 50, 379–396. https://doi.org/10.1139/cjes-2012-0065

Dyke, A.S., Andrews, J.T., Clark, P.U., England, J.H., Miller, G.H., Shaw, J., Veillette, J.J., 2002. The Laurentide and Innuitian ice sheets during the Last Glacial Maximum. Quat. Sci. Rev. 21, 9–31. https://doi.org/10.1016/S0277-3791(01)00095-6

Dyke, A.S., Prest, V.K., 1987. Late Wisconsinan and Holocene History of the Laurentide Ice Sheet. Géographie Phys. Quat. 41, 237–263. https://doi.org/10.7202/032681ar

Evans, D.J.A., Benn, D., 2004. Chapter 5 - Macrofabric., in: A Practical Guide to the Study of Glacial Sediments, Edited by D. Evans and D. Benn: Routledge.

Evans, D.J.A., Phillips, E.R., Hiemstra, J.F., Auton, C.A., 2006. Subglacial till: Formation, sedimentary characteristics and classification. Earth-Sci. Rev. 78, 115–176. https://doi.org/10.1016/j.earscirev.2006.04.001

Gao, C., Huot, S., McDonald, A.M., Crabtree, D.C., Turton, C.L., 2020. Subtill nonglacial deposits and their climatic implications for the Last Interglacial (MIS 5e), Hudson Bay Lowlands, Canada. Quat. Sci. Rev. 248, 106590. https://doi.org/10.1016/j.quascirev.2020.106590

Gao, C., V.L. Lee, K.H. Yeung, 2015. Project Unit 15-001: Field Studies in Support of Remote Predictive Mapping in the Missisa Lake Area, Far North of Ontario (No. Open File Report 6313), Summary of Field Work and Other Activities 2015. Ontario Geological Survey.

Gauthier, M.S., Hodder, T.J., Lian, O.B., Finkelstein, S.A., Dalton, A.S., Paulen, R.C., 2021. Stratigraphic, paleoenvironmental and geochronological investigations of intertill nonglacial deposits in northeastern Manitoba (parts of NTS 54B-F, K, L, 64A, H, I). Manit. Agric. Resour. Dev. Manit. Geol. Surv. Report of Activities 2021, 71–76.

Gauthier, M.S., Hodder, T.J., Ross, M., 2022. 2022: Quaternary stratigraphy and ice-flow indicator data for the Gillam region, Manitoba (parts of NTS 54C, D, 64A). Manit. Nat. Resour. North. Dev. Manit. Geol. Surv. Geoscientific Paper GP2022-2, 37.

Gauthier, M.S., Hodder, T.J., Ross, M., Kelley, S.E., Rochester, A., McCausland, P., 2019. The subglacial mosaic of the Laurentide Ice Sheet; a study of the interior region of southwestern Hudson Bay. Quat. Sci. Rev. 214, 1–27. https://doi.org/10.1016/j.quascirev.2019.04.015

Grunsky, E.C., 2010. The interpretation of geochemical survey data. Geochem. Explor. Environ. Anal. 10, 27–74. https://doi.org/10.1144/1467-7873/09-210

Harrison, S., Smith, D.E., Glasser, N.F., 2018. Late Quaternary meltwater pulses and sea level change. J. Quat. Sci. 34, 1–15. https://doi.org/10.1002/jqs.3070

Hawley, J.E., 1925. Geology and economic possibilities of Sutton Lake area, District of Patricia. Ont. Dep. Mines Annual Report 1925 34, 53.

Hicock, S.R., Goff, J.R., Lian, O.B., Little, E.C., 1996. On the interpretation of subglacial till fabric. J. Sediment. Res. 66, 928–934.

Hodder, T.J., 2024. RE: K2O in Kenogami. Pers. Commun.

Hodder, T.J., Gauthier, M.S., Nielsen, E., 2017. Quaternary stratigraphy and till composition along the Hayes, Gods, Nelson, Fox, Stupart, Yakaw, Angling and Pennycutaway rivers, northeast Manitoba (parts of NTS 53N, 54C, 54D, 54F). Manit. Geol. Surv. Open File 2017-4.

Hodder, T.J., Gauthier, M.S., Ross, M., Lian, O.B., 2023. Was there a nonglacial episode in the western Hudson Bay Lowland during Marine Isotope Stage 3? Quat. Res. 116, 148–161. https://doi.org/10.1017/qua.2023.35

Holmes, C.D., 1941. Till Fabric. Bull. Geol. Soc. Am. 52, 1299–1354.

Iverson, N.R., 2017. Determining glacier flow direction from till fabrics. Geomorphology 299, 124–130. https://doi.org/10.1016/j.geomorph.2017.10.005

Jackson, G.D., 2013. Geology, Belcher Islands, Nunavut. Open File Report 4923. https://doi.org/10.4095/292434

Jenner, G.A., 1996. Trace Element Geochemistry of Igneous Rocks: Geochemical Nomenclature and Analytical Geochemistry, in: Trace Element Geochemistry of Volcanic Rocks: Applications for Massive Sulphide Exploration, Short Course Notes. Geological Association of Canada, pp. 51–77.

Jolliffe, I.T., Cadima, J., 2016. Principal component analysis: a review and recent developments. Philos. Trans. R. Soc. Math. Phys. Eng. Sci. 374. https://doi.org/10.1098/rsta.2015.0202

Klassen, R.W., 1986. Surficial geology of north-central Manitoba, Memoir / Geological Survey of Canada. Geological Survey of Canada, Ottawa, Canada.

Margold, M., Stokes, C.R., Clark, C.D., 2018. Reconciling records of ice streaming and ice margin retreat to produce a palaeogeographic reconstruction of the deglaciation of the

Laurentide Ice Sheet. Quat. Sci. Rev. 189, 1–30. https://doi.org/10.1016/j.quascirev.2018.03.013

McCurdy, M.W., Garrett, R.G., 2016. Geochemical data quality control for soil, till and lake and stream sediment samples (No. 7944). https://doi.org/10.4095/297562

McDonald, B.C., 1969. Glacial and Interglacial Stratigraphy, Hudson Bay Lowland (No. 68–53). Geological Survey of Canada. https://doi.org/10.4095/102949

McMartin, I., Paulen, R.C., 2009. Ice-Flow Indicators and the Importance of Ice-Flow Mapping for Drift Prospecting. Appl. Till Stream Sediment Heavy Miner. Geochem. Methods Miner. Explor. West. North. Can. Geological Association of Canada Short Course Notes, 15–34.

Miller, G.H., Andrews, J.T., 2019. Hudson Bay was not deglaciated during MIS-3. Quat. Sci. Rev. 225, 1–7. https://doi.org/10.1016/j.quascirev.2019.105944

Natural Resources Canada, 2023. Canadian Digital Elevation Model (CDEM), 1945-2011.

Nicolas, M.P.B., Armstrong, D.K., 2017. GS2017-12: Update on Paleozoic stratigraphic correlations in the Hudson Bay Lowland, northeastern Manitoba and northern Ontario. Manit. Agric. Resour. Dev. Manit. Geol. Surv. Report of Activities 2017, 133–147.

Nielsen, E., Morgan, A.V., Morgan, A., Mott, R.J., Rutter, N.W., Causse, C., 1986. Stratigraphy, paleoecology, and glacial history of the Gillam area, Manitoba. Can. J. Earth Sci. 23, 1641–1661.

Ontario GeoHub, 2023. Provincial Digital Elevation Model (PDEM).

Ontario Geological Survey, 2011. 1:250 000 Scale Bedrock Geology of Ontario. MRD126.

Ontario Geological Survey, 1997. Quaternary Geology, Seamless Coverage of the Province of Ontario. EDS014-REV.

Parent, M., Paradis, S.J., Boisvert, É., 1995. Ice-flow patterns and glacial transport in the eastern Hudson Bay region: implications for the late Quaternary dynamics of the Laurentide Ice Sheet. Can. J. Earth Sci. 32, 2057–2070. https://doi.org/10.1139/e95-159

Piercey, S.J., 2014. Modern Analytical Facilities 2. A Review of Quality Assurance and Quality Control (QA/QC) Procedures for Lithogeochemical Data. Geosci. Can. 41, 75–88. https://doi.org/10.12789/geocanj.2014.41.035

Riley, J.L., 2011. Wetlands of the Hudson Bay Lowland: an Ontario overview. Nature Conservancy of Canada, Toronto.

Ross, M., 2022. Update Till Fabric Analysis Demo-Copy1.ipynb. Modif. Robin Taves Nov 2022.

Roy, M., Dell'Oste, F., Veillette, J.J., De Vernal, A., Hélie, J.-F., Parent, M., 2011. Insights on the events surrounding the final drainage of Lake Ojibway based on James Bay stratigraphic sequences. Quat. Sci. Rev. 30, 682–692. https://doi.org/10.1016/j.quascirev.2010.12.008

Sanford, B.V., Norris, A.W., Bostock, H.H., 1968. Geology of the Hudson Bay Lowlands (Operation Winisk). (No. Paper 67-60). Geological Survey of Canada.

Shilts, W., 1982. Quaternary evolution of the Hudson/James Bay region. Nat. Can. 109, 309–332.

Skinner, R.G., 1973. Quaternary Stratigraphy of the Moose River Basin, Ontario. Geol. Surv. Can. Bulletin 225.

SRC, 2024. Services Schedule. Sask. Res. Counc. Geoanalytical Laboratories.

Stokes, C.R., Margold, M., Clark, C.D., Tarasov, L., 2016. Ice stream activity scaled to ice sheet volume during Laurentide Ice Sheet deglaciation. Nature 530, 322–326. https://doi.org/10.1038/nature16947

Stott, G.M., Buse, S., Davis, D.W., Hamilton, M.A., 2010. The Sutton Inliers - A Paleoproterozoic Succession in the Hudson Bay Lowlands, in: Summary of Field Work and Other Activites. Ontario Geological Survey, pp. 19–1 to 19–14.

Thorleifson, H., n.d. Review of Lake Agassiz History. Geol. Surv. Can. 55–84.

Thorleifson, L.H., Wyatt, P.H., Warman, T.A., 1993. Quaternary stratigraphy of the Severn and Winisk drainage basins, northern Ontario (No. 442). https://doi.org/10.4095/183911

United States Geological Survey, 2005. Geological Map of North America.

Veillette, J.J., Dyke, A.S., Roy, M., 1999. Ice-flow evolution of the Labrador Sector of the Laurentide Ice Sheet: a review, with new evidence from northern Quebec. Quat. Sci. Rev. 18, 993–1019.

Veillette, J.J., Roy, M., Paulen, R.C., Ménard, M., St-Jacques, G., 2017. Uncovering the hidden part of a large ice stream of the Laurentide Ice Sheet, northern Ontario, Canada. Quat. Sci. Rev. 155, 136–158. https://doi.org/10.1016/j.quascirev.2016.11.008

Vincent, J.-S., 1989. Quaternary Geology of the southeastern Canadian Shield., in: Quaternary Geology of Canada and Greenland. Geological Survey of Canada, Ottawa, Canada, pp. 245–275.

Wang, Y., 2018. Statistical analysis of till geochemistry in the Nelson River area, northeastern Manitoba: implications for Quaternary glacial stratigraphy. University of Waterloo.

# Appendix A. Detailed Stratigraphic Columns

All stratigraphic columns have been dip corrected to true thicknesses and use the legends as shown below.

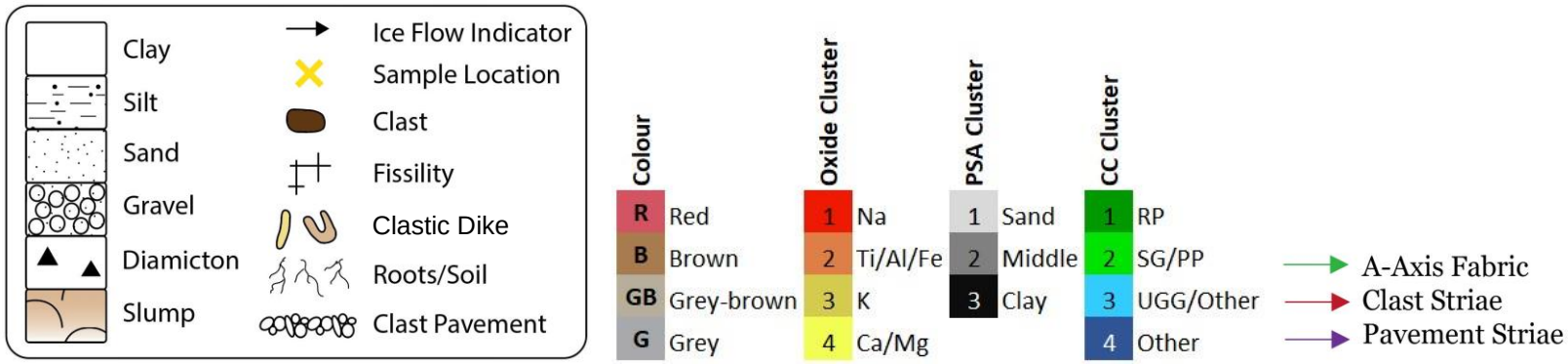


## Albany River 11 (AR11)

AR11 is located on the south side of the Albany River near a fork in the river. It is roughly 10 m high with 8 m of exposure and 2 m of slump material. There are four till units identified, from the bottom to top are a grey, brown, brown with silty laminations, and a red till with a large silt lense in the middle. Contacts are sharp in all cases and the grey to brown contact is undulous. The significant silt lamination in the upper brown unit has a small gravel lag at the base.

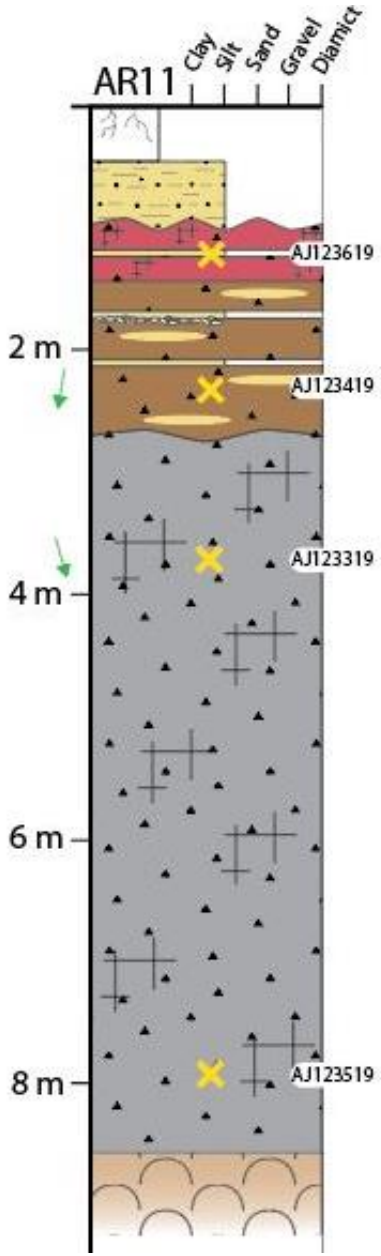


NAD 83 UTM Zone 16: 557809E 5733679N

| Unit: Lithofacies Code | Description and Interpretation |
|---|---|
| Soil | |
| Fm | |
| 4: Dmm, Fm | Red diamicton with iron staining along fine fissility. Single silt bed divides the unit into two layers and has soft gravel at the base. Sharp lower contact. Subglacial traction till. |
| 3: Dmm, Fm | Brown diamicton heavily interbedded with silt. Small clasts with no cobbles present. Silt layer along sharp lower contact. Subglacial traction till. |
| 2: Dmm, Fm, Sm, GRm | Brown with moderate iron staining along fissility. Silt, sand, and gravel beds up to 5 cm thick pinch out laterally. No cobbles present. Undulous lower contact dips to the SW. Subglacial traction till. |
| 1: Dmm | Grey, hard, compact, and dry with a high clast content. Coarse, steeply dipping fissility in sheets ~2 cm thick throughout. Moderate iron staining along fissility reduces with depth. No lower contact seen. Subglacial traction till. |

| Sample | Colour | Oxide Cluster | PSA Cluster | CC Cluster |
|---|---|---|---|---|
| AJ123619 | R | 3 | 3 | 1 |
| | B | | | |
| AJ123419 | B | 4 | 1 | 2 |
| AJ123319 | G | 4 | 1 | 3 |
| AJ123519 | G | 1 | 1 | 3 |

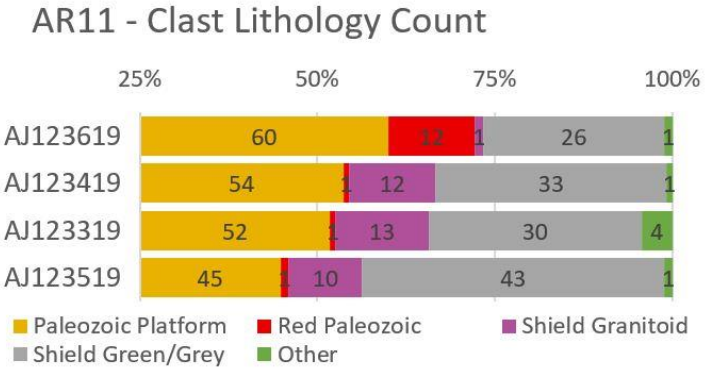


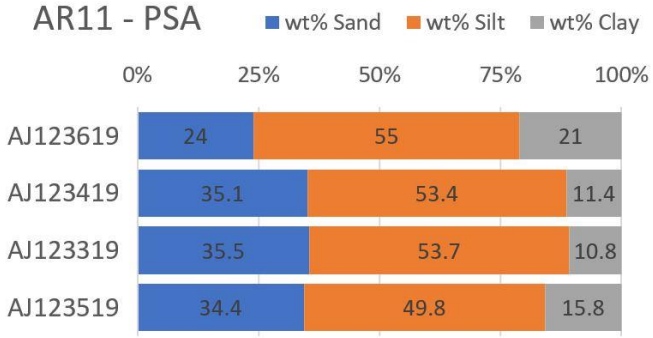

### Albany River 9B (AR9B)

AR9B is located 200 m west of AR9 and was visited over two, not sequential, days. It is a 10 m high bluff on the north shore of the Albany River with patchy but extensive exposure. The top 7 m of the bluff was cleared but no angle measurement was recorded or measuring tape used to retrieve depths of units. Staff recollection is that this bluff was quite steep and likely higher than the average 46 degrees of all bluffs. As a result, the two depths of sample sites and field sketch values were used uncorrected as this was deemed more accurate than the corrected values using the average.

The base of this unit begins with fine, laminated, glaciolacustrine material overridden by upward coarsening, glaciofluvial sands. Above a sharp and undulous contact is a grey, subglacial traction till containing pipe flow features and a dipping clast pavement at the top. The subsequent two units are both brown, subglacial traction tills with varying characteristics. The lower brown till has platey fissility whereas the upper brown till is very soft with no fissility. The next unit is a prominent silt layer with sharp contacts below and above with a red diamicton, also interpreted as a subglacial traction till. Interbedded clays and silts (glaciolacustrine varves) were deposited for the top 0.5 m of this bluff.

### Albany River 9 (AR9)

AR9 is 200 m east of AR9B along the north shore of the Albany River. Between the units, the fine, laminated glaciolacustrine material was intermittently observed but not present exactly at AR9. AR9 is approximately 20 m tall with 7 m of exposed stratigraphy and sparse vegetation. At its base is a grey, highly compact, subglacial traction till with a clast pavement at its upper contact. Above the clast pavement is a grey-brown subglacial traction till that is also highly compact. The next two diamictons are brown and also interpreted as subglacial traction tills. They have sharp contacts and are separated by a thin silt layer. The lower brown till is looser with silty, dipping interbeds up to 1 cm thick. The upper brown till is also soft but has some fissility. The top of this bluff is a relatively thick glaciolacustrine silt unit with beds of red and grey sediments and some pebbles throughout.

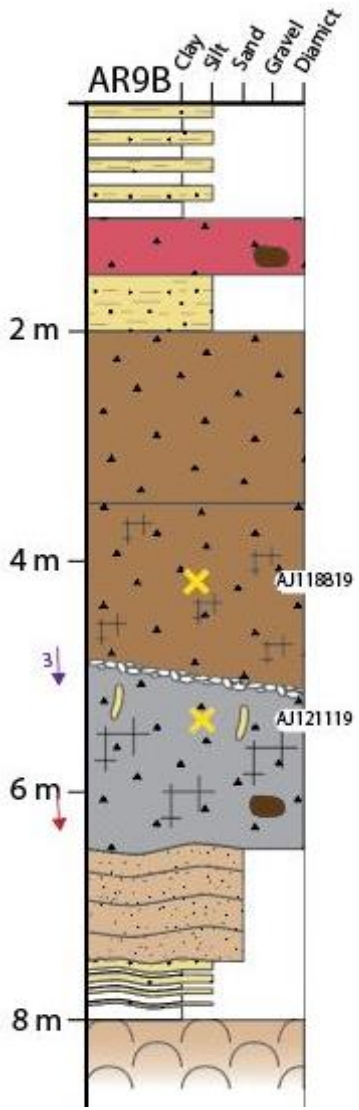


NAD 83 UTM Zone 16: 557927E 5734116N

| Unit: Lithofacies Code | Description and Interpretation |
|---|---|
| Flv | Interbedded clay and silt. Glaciolacustrine varves. |
| 4: Dmm | Red diamicton with large boulder. Subglacial traction till. |
| Silt | |
| 3: Dmm | Brown diamicton that is very soft with no fissility. Subglacial traction till. |
| 2: Dmm | Brown till with platey fissility in no pattern. Minor iron staining on the joints. Sharp lower contact is dipping with weak boulder pavement containing striated clast. Subglacial traction till. |
| BL | |
| 1: Dmm, Sm | Grey, over-compacted, fissile diamicton with sandy pipe flow features along joints dipping ENE. Sample located right below cobble lag. Lower contact is sharp and undulous. Subglacial traction till. |
| Suc, Sd | Silty sand, slightly deformed, stratified layers that coarsen upwards to upper contact. Glaciofluvial sediments. |
| Fl | Fine, laminated material. Glaciolacustrine. |

| Sample | Colour | Oxide Cluster | PSA Cluster | CC Cluster |
|---|---|---|---|---|
| AJ118819 | B | 4 | 2 | 3 |
| AJ121119 | G | 1 | 1 | 3 |

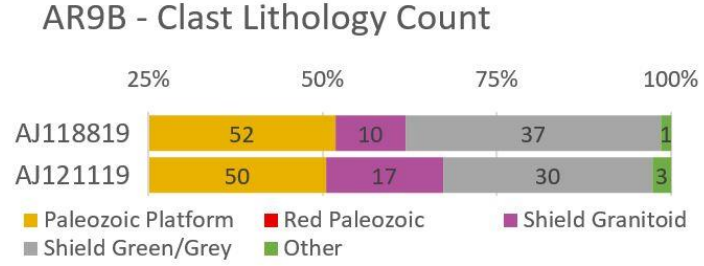


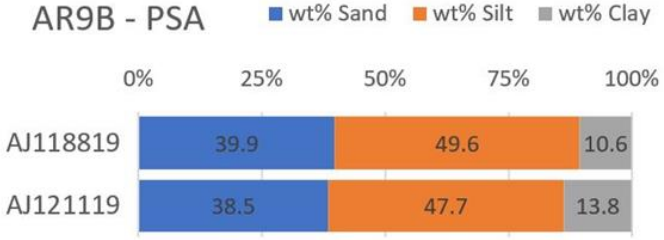

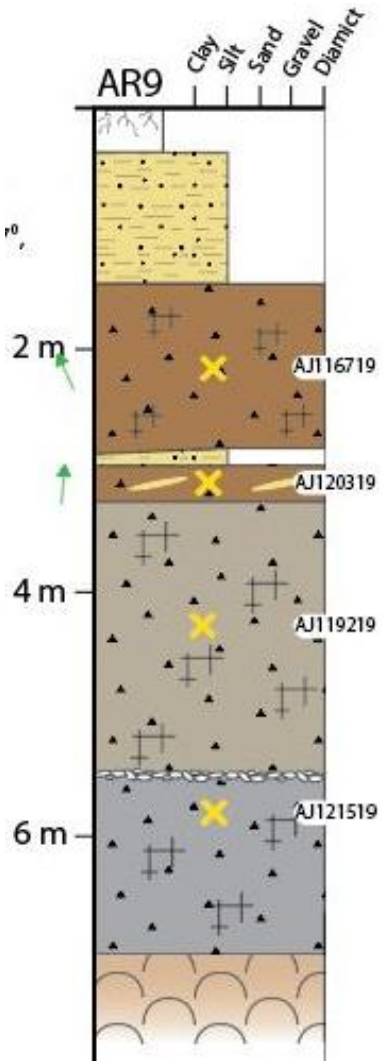


NAD 83 UTM Zone 16: 558138E 5734130N

| Unit: Lithofacies Code | Description and Interpretation |
|---|---|
| Soil | |
| Fl(d) | Layers of red and grey silt sediments with pebbles. Sharp lower contact. Glaciolacustrine silt. |
| 4: Dmm | Brown diamicton with moderate amount of iron staining along joints and some local oxidation throughout. Medium fissility and soft. Sharp lower contact is dipping. Subglacial traction till. |
| Sm | |
| 3: Dmm, Sm | Brown, relatively soft, sandy diamicton. Silty interbeds of about 1 cm thickness dipping south. Sharp upper and lower contact. Subglacial traction till. |
| 2: Dmm(p) | Grey-brown, and blocky above minor boulder lag and sharp lower contact. Heavy oxidation along joints. Unit has very coarse fissility and is overcompacted. Less cobbles than unit below. Subglacial traction till. |
| BL | |
| 1: Dmm | Grey over-compacted diamicton with coarse fissility. Subglacial traction till. |

| Sample | Colour | Oxide Cluster | PSA Cluster | CC Cluster |
|---|---|---|---|---|
| AJ116719 | B | 2 | 3 | 2 |
| AJ120319 | B | 4 | 2 | 2 |
| AJ119219 | GB | 4 | 1 | 3 |
| AJ121519 | G | 4 | 2 | 3 |

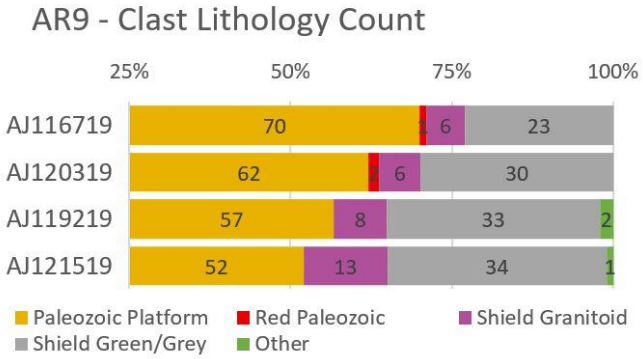


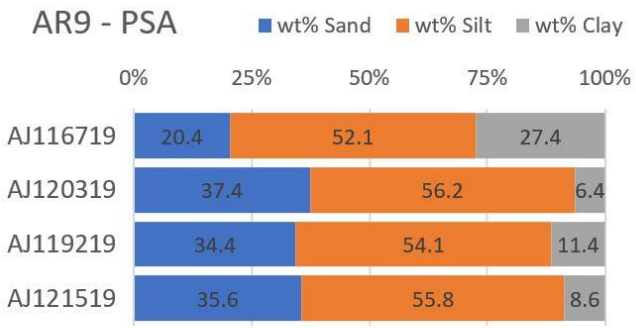

### Dark River 2 (DR2)

DR2 lies on the northeast bank of a bend in a slow-moving part of the river. It is laterally limited with pervasive vegetation along the bottom and edges. There are four tills, three red and one brown, capped by almost one meter of silty sand with lenses of red till entrained. The bottom three tills are red with fine fissility and gradational contacts. Clast content was noted in the field to be high in unit 1 with highest sand content in unit 3. Unit 2 contains lenses of leached till and pinches out laterally. Unit 3 has grey till lenses in the upper half, below the sharp and undulous contact with brown till. The brown till is clast rich with clay balls and a single large silt lense just above the lower contact. It has a sharp and undulous contact with the overlying sand which, while largely beige, has some red lenses.

### Ogoki River 4 (OR4)

OR4 is located on the east side of the Ogoki River with a heavily vegetated, 10 m slump at the bottom. The exposed succession is 6 m high dominated by red till with a sharp, silt contact to grey till at its base. Silt is present at two of the contacts of the red till while two tills have silt lensing throughout. Contacts are sharp aside from one which is gradational between two red tills in the middle of the sequence. Characteristics of the red till vary at this site from fissile to no fissility and compact to lose. The uppermost red till appears deformed and could be a slow creep material but the other tills are interpreted as subglacial tractions tills.

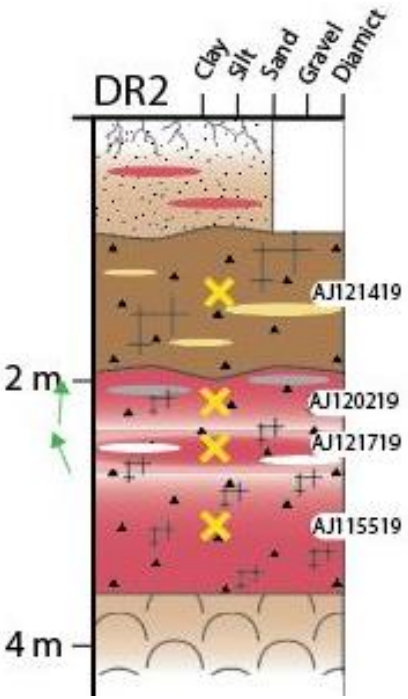


NAD 83 UTM Zone 16: 567937E 5712549N

| Unit: Lithofacies Code | Description and Interpretation |
|---|---|
| Sm | Mostly beige silty sand with some red lenses. Sharp and undulous lower contact. Possibly glaciolacustrine sediments. |
| 4: Dmm(p), Sm, Fm | Brown diamicton that is clast rich. Coarsely fissile with dark, pedogenic alteration along joints. Clay balls up to one cm diameter throughout. Large silt lens at 1.5 m. Undulous and sharp lower contact. Subglacial traction till. |
| 3: Dmm | Red and fissile with pedogenic alteration in the joints. Lenses of grey till in upper 20 cm. Few large clasts with higher coarse sand content than below. Sharp gradational lower contact over 10 cm. Subglacial traction till. |
| 2: Dmm | Red, finely fissile till with high silt and clay content . Clast poor with lenses of leached till. Gradational textural contact with comparable till below. Pinches out laterally. Subglacial traction till. |
| 1: Dmm | Red, finely fissile diamicton. Clast rich compared to other layers. Lower contact not seen. Subglacial traction till. |

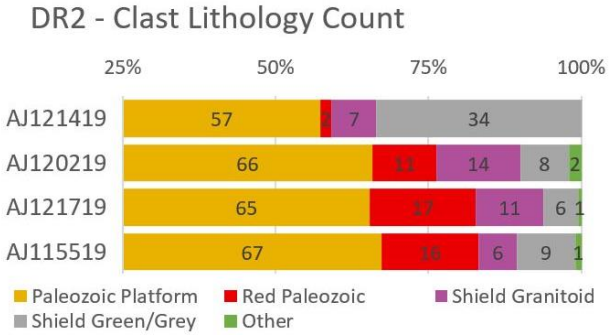


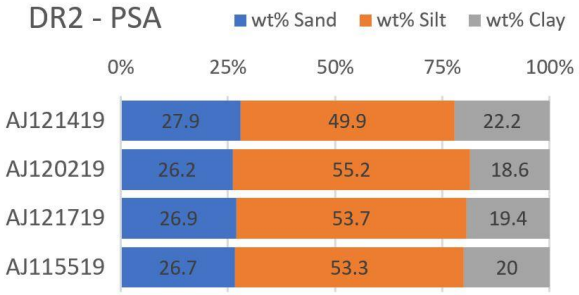


| Sample | Colour | Oxide Cluster | PSA Cluster | CC Cluster |
|---|---|---|---|---|
| AJ121419 | B | 2 | 3 | 2 |
| AJ120219 | R | 3 | 3 | 1 |
| AJ121719 | R | 3 | 3 | 1 |
| AJ115519 | R | 3 | 3 | 1 |

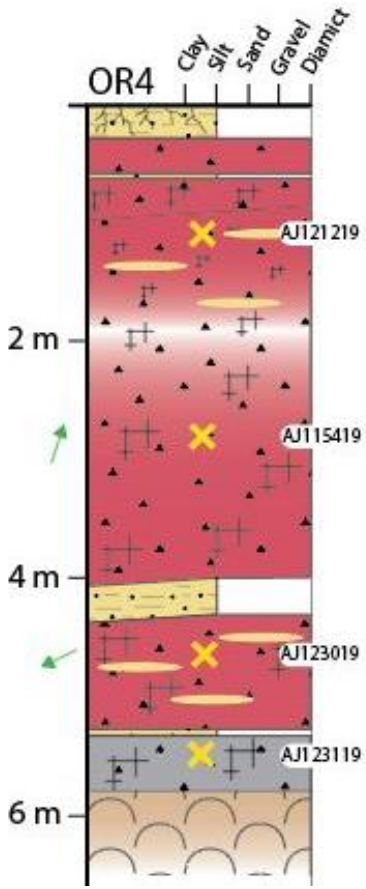


NAD 83 UTM Zone 16: 572049E 5705116N

| Unit: Lithofacies Code | Description and Interpretation |
|---|---|
| Sm<br>6: Dmm | Interbedded green-grey and red altered diamicton. Bounded by silt lenses at sharp contacts. Subglacial traction till or potential slow creep subglacial till. |
| 5: Dmm, Fm | Red with medium fissility and clay balls. Sharp angular lower contact with a small, angled layer of light brown laminated diamict. Subglacial traction till. |
| 4: Dmm, Fm | Red, soft diamict with fine fissility and thin silt lenses throughout. Lower contact is gradational change in texture. Subglacial traction till. |
| 3: Dmm | Red, clast poor diamict with coarse fissility and some iron staining on joints. Sharp angular contact with below laminated silt but no silt lenses throughout. Subglacial traction till. |
| Fl | Laminated silt. Glaciofluvial material. |
| 2: Dmm, Fm | Red and very soft with lenses of silt and grey-red diamict. Coarse fissility with iron stained joints. Silt lense at lower contact. Red carbonates with crinoid fossils. Subglacial traction till. |
| 1: Dmm | Grey and highly compact with coarse fissility. Some iron staining on joints. Cobbles larger relative to other units. No lower contact seen. Subg traction till. |

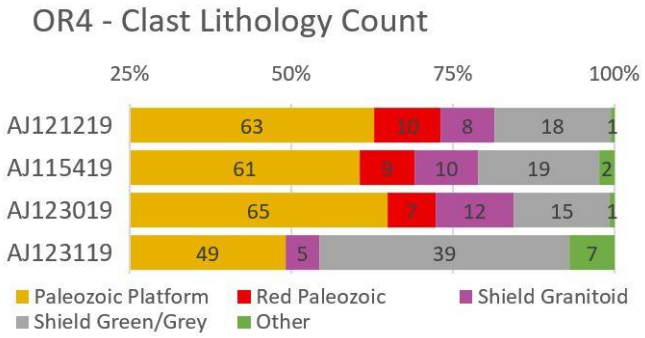


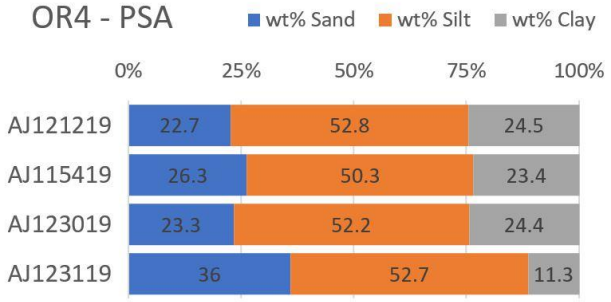


| Sample | Colour | Oxide Cluster | PSA Cluster | CC Cluster |
|---|---|---|---|---|
| AJ121219 | R | 3 | 3 | 1 |
| AJ115419 | R | 3 | 3 | 1 |
| AJ123019 | R | 3 | 3 | 1 |
| AJ123119 | G | 4 | 1 | 4 |

### Ogoki River 3 (OR3)

OR3 is a relatively shallow dipping bluff on the northwest side of a bend on the Ogoki River. There is ~5.5 m of exposed bluff with a further ~6 m of flat vegetated slump. Carbonate bedrock is exposed at river level. There are 6 till units at this bluff and two fluvial units near the base. Unit 1 is a highly-compacted, grey till which a fluvial material sharply overlies. The lower fluvial material is well-sorted, upward fining sand 30 cm thick. It is overridden by a 20 cm of grey-brown till, followed by a moderately-sorted, matrix-supported (sand), cobble unit. Above this fluvial unit is a succession of grey till, then brown till, and capped by red till. The brown and red till have an interfingered contact over 20 cm. There are two units of red till separated by a 5 cm thick silt lense. The lower red till has increased lenses of leached material and lighter colour with decreased depth whereas the upper red till has silt lenses throughout.

### Ogoki River 2 (OR2)

OR2 is on the NW corner of a bend in the Ogoki River with carbonate bedrock at river level. It is 10 m high with 4 m of exposure and heavy vegetation at the bottom. The base of this section has a matrix-supported fluvial unit of sand matrix and coarse cobbles. The upper portion has a higher silt content and a sharp contact with an overlying, thin, grey till unit. Above a sharp, undulous contact with grey till is 2 m of red till split into two units. In the lower red till the fissility fines, compaction decreases and becomes less blocky, and gravel content increases with depth. The 30 cm upper red till unit has no fissility. Silt lensing is present through both red till units and all red till contacts are sharp and undulous. Above the red till is a 20 cm unit of silt below a 20 cm, fissile, brown till unit.

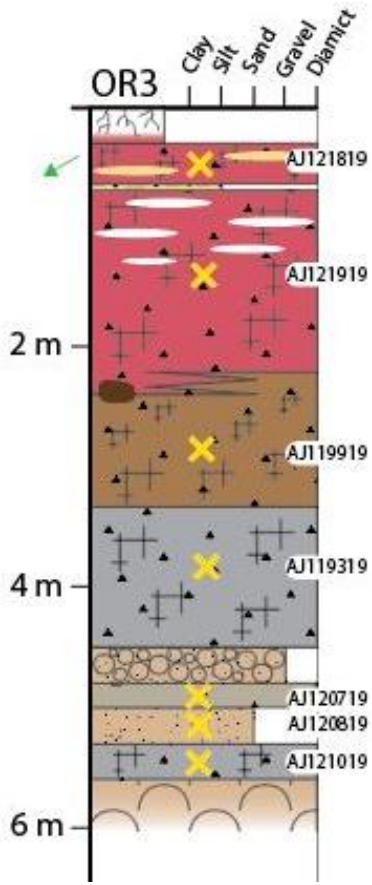


NAD 83 UTM Zone 16: 572377E 5705821N

| Unit: Lithofacies Code | Description and Interpretation |
|---|---|
| Soil | |
| 6: Dmm, Fm | Red diamict with thin, discontinuous lenses of silt. Very compact and fissile with iron staining along joints. Not blocky. Lenses of silt ~5 cm thick at sharp lower contact. Subglacial traction till. |
| 5: Dmm, Fm | Red, blocky, compacted, diamicton with coarse fissility and high clay and low gravel content. Bands (4 cm thick) of leached till in upper portion. Interfingered lower contact over 20 cm with red colour begining to fade below 2.1 m. Subglacial traction till. |
| 4: Dmm | Brown diamict with iron staining along joints. Fissility is fine at the top and coarsens with depth. Clast content increases with depth to sharp lower contact. Subglacial traction till. |
| 3: Dmm | Grey, very-compact diamict with a high clast content. Very coarse fissility with extensive iron staining along joints. Sharp lower contact with gravel. Subglacial traction till. |
| Gm 2: Dmm | Grey-brown, thin, lightly compacted diamict. Higher gravel and sand content near the top with large clasts of mixed lithologies. Weak iron staining along minor joints. Sharply bounded by gravel above and sand below. Subglacial traction till. |
| Suf | Well sorted, light brown sand. Upward gradational sorting with gravel content highest at base. Unit dips down into the bluff. Glaciofluvial sediment. |
| 1: Dmm | Grey, highly compacted diamict with coarse fissility. No lower contact seen. Subglacial traction till. |

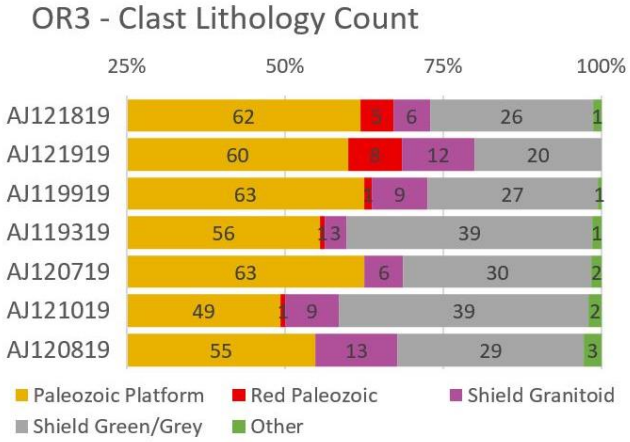


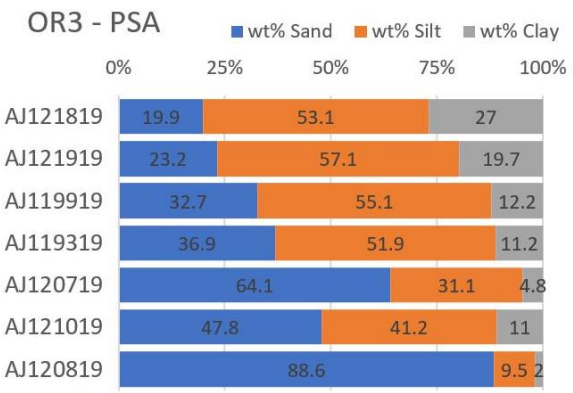


| Sample | Colour | Oxide Cluster | PSA Cluster | CC Cluster |
|---|---|---|---|---|
| AJ121819 | R | 2 | 3 | 1 |
| AJ121919 | R | 3 | 3 | 1 |
| AJ119919 | B | 4 | 1 | 2 |
| AJ119319 | G | 4 | 1 | 4 |
| AJ120719 | GB | 4 | | 3 |
| AJ121019 | G | 1 | 2 | 3 |

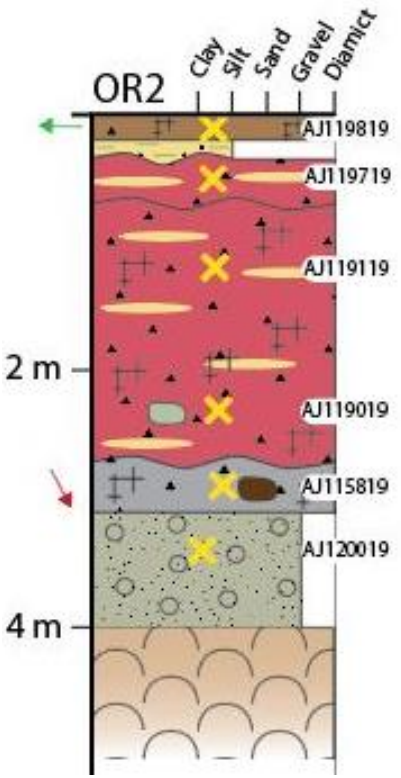


NAD 83 UTM Zone 16: 572686E 5706513N

| Unit: Lithofacies Code | Description and Interpretation |
|---|---|
| 4: Dmm<br>Sm<br>3: Dmm | Brown, very fissile, thin diamicton with few clasts but some cobbles. Sharp contacts. Subglacial traction till.<br>Red diamicton with leached lenses up to 10 cm thick throughout. Sharp, undulous upper contact with a silt lense. Sharp, undulous, lower contact. Subglacial traction till. |
| 2: Dmm, Fm | Red diamicton with silt lenses and minor iron staining along joints. Coarse fissility, blocky, and compact upper portion. Fissility decreases with depth and gravel content is high at the base. Large green diamicton clast present. Sharp lower contact is undulous. Subglacial traction till. |
| 1: Dmm | Grey, silty-sandy, compact diamicton with cobbles and some rotten clasts. Extremely fissile with weak iron staining on joints. Sharp lower contact. Subglacial traction till. |
| Gms, Gfu | Grey-green coarse layer with coarse gravel to boulders of mixed lithologies. High silt content in top 10 cm. No lower contact seen. Glaciofluvial. |

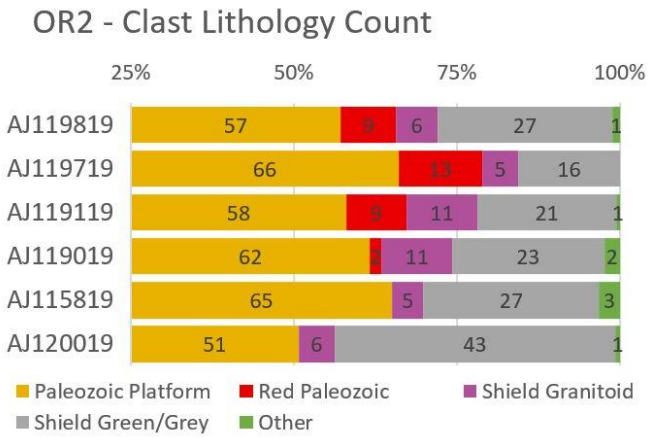


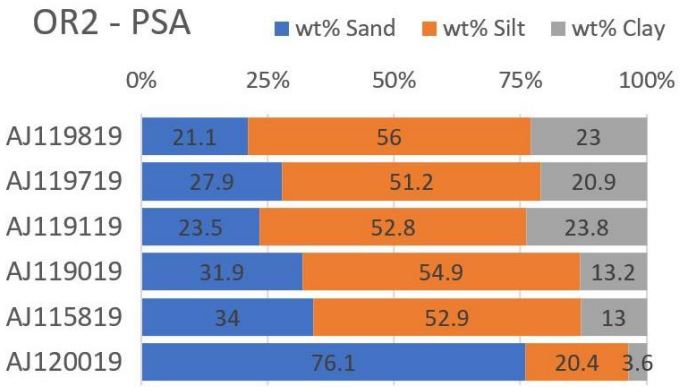


| Sample | Colour | Oxide Cluster | PSA Cluster | CC Cluster |
|---|---|---|---|---|
| AJ119819 | B | 3 | 3 | 1 |
| AJ119719 | R | 3 | 3 | 1 |
| AJ119119 | R | 3 | 3 | 1 |
| AJ119019 | R | 4 | 1 | 3 |
| AJ115819 | G | 4 | 1 | 4 |

**Albany River 6 (AR6)**

AR6 is a small bluff with only 4 m of stratigraphy exposed. Slumped material is relatively thick and heavily vegetated along the south bank of the river. Three subglacial traction tills are present here capped by laminated fines containing drop stones. The till succession starts with grey till at the bottom with a boulder pavement along its upper contact with a grey-brown till. The grey-brown till grades into the top brown till. The grey till has a large (~1 m) pipe flow feature of sand and proximal alteration of the till.

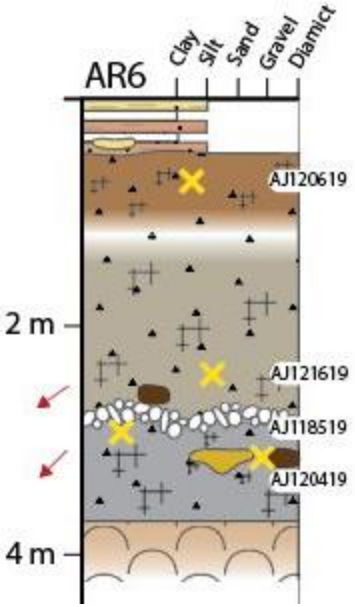


## Albany River Section 6 (AR6)

NAD 83 UTM Zone 16: 590141E 5721578N

| Unit: Lithofacies Code | Description and Interpretation |
|---|---|
| Flv(d), Sm | Laminated silt and clay with some drop stones. Sharp colour change from tan above to red below at 0.2 m. Undulating silt lense 5 cm thick. Glaciolacustrine sediment. |
| 3: Dmm | Brown, very crumbly diamicton with fine fissility and iron staining. Subglacial traction till. |
| 2: Dmm(p) | Grey-Brown, blocky, and compact with coarse fissility. Jointing is horizontal in the upper part with minor jointing in the cobble-rich lower portion. Sharp lower contact with boulder pavement. Subglacial traction till. |
| BL | |
| 1: Dmm, Sm | Grey, over-compact diamicton with coarse fissility and many oversized clasts. Blocky and breaks in small chunks. Sample AJ118519 is more representative of material as AJ120419 is in softer material surrounding a ~0.6 m wide sand pocket. No lower contact seen. Subglacial traction till. |

| Sample | Colour | Oxide Cluster | PSA Cluster | CC Cluster |
|---|---|---|---|---|
| AJ120619 | B | 4 | 1 | 3 |
| | GB | | | |
| AJ121619 | GB | 4 | 1 | 3 |
| AJ118519 | G | 4 | 1 | 4 |
| AJ120419 | G | 4 | 2 | 3 |

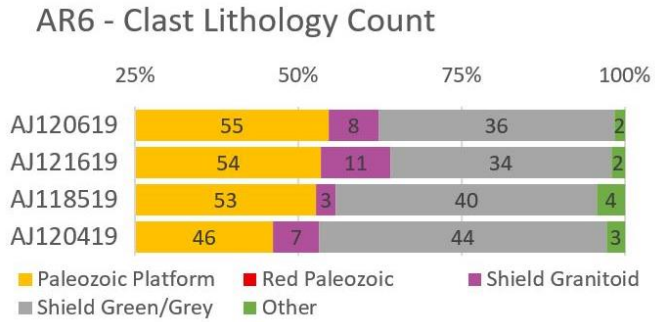


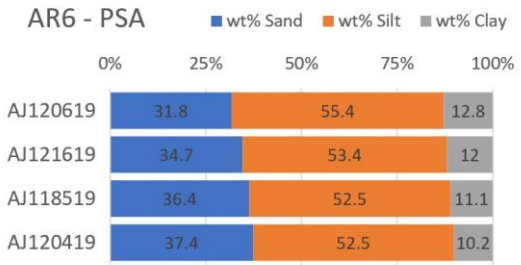

### Albany River 5 (AR5)

AR5 is a laterally continuous (>50 m) bluff with approximately 7.5 m of exposed, depth-corrected, in-situ material. Immediately under is 2 m of unvegetated slump material with a further 5 m of vegetated slump down to the river. It is on the south bank of the Albany River with dip from horizontal of 50°. There are four subglacial traction tills present, three boulder lags, and a relatively thick fluvial succession on top. The bottom two units are grey, over-compacted diamictons with coarse fissility, blocky texture, and divided by a moderately defined boulder lag with striae measurements trending 165°. The first unit has iron staining on joints, steep fractures, and a pipe flow feature near the top. The second grey unit has a more pervasive cobble presence than the lower till. Overlying the grey units is a grey-brown till with coarse fissility and flakey texture. The basal contact is a well-defined boulder pavement with several striae trending toward 180° – 162°. There is a gradational contact between unit 3 and 4. Unit 4 is brown and has a soft texture with fine fissility and abundant small clasts. Above a sharp contact with a gravel lag is a relatively thick fluvial succession of laminated silts and clay, interpreted to be glaciofluvial varves, below a sand- silt unit.

### Albany River 2 (AR2)

AR2 is the largest bluff visited at 9.1 m of depth-corrected material exposed. Sulfide boulders are seen throughout this bluff, being most notable in unit 1, 3, and 6. The bluff is approximately 30-40 m high and 50° from horizontal with heavy vegetation on the bottom 15 m. Units were hard to distinguish at this bluff. The bottom two units are grey, blocky, and coarsely fissile with a westward dipping, sharp contact defined by a sand bed. Above these are two units of grey-brown till. The fissility, pebble content, and compaction decrease with depth while lenses of white sand are throughout. Unit 4 then maintains the coarser fissility, high pebble content, and high compaction with increased blocky texture and no sand lenses. Above unit 4 is an undulous, sharp contact into 3 grey tills. Unit 5 and 6 have coarse fissility whereas unit 7 has fine. Unit 5 and 7 have sand lenses throughout while unit 6 does not, but rather has gravel and clasts throughout. Above the grey tills is a unit of massive sand with sharp, undulous contacts. Unit 8 and 9 are both brown tills with a thin, undulous sand layer in between including a minor pebble lag at the base of unit 9. Both brown tills have iron staining, sand lenses throughout, and fine fissility. The fissility in unit 8 is more horizontal than unit 9.

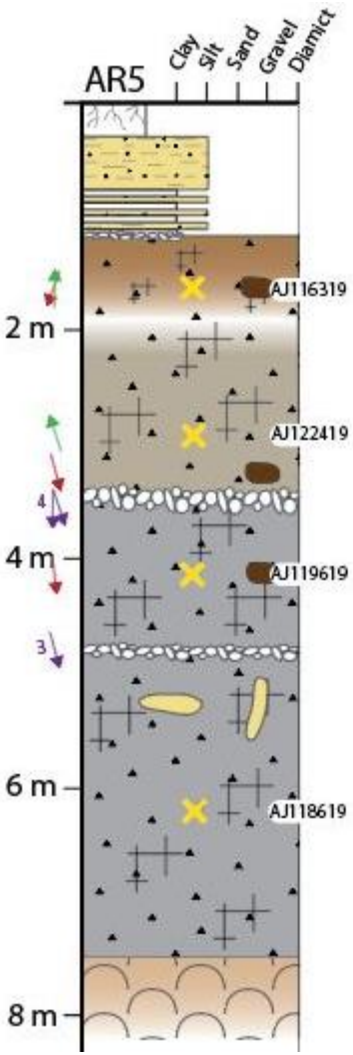


NAD 83 UTM Zone 16: 593954E 5722602N

| Unit: Lithofacies Code | Description and Interpretation |
|---|---|
| Soil | |
| Fm<br>Flv | Sandy silt overlying laminated silt and clay rhythmites. Lower contact is sharp with a gravel lag. Glaciolacustrine with varves. |
| 4: Dmm | Brown, very soft diamicton with many small clasts, fine fissility, and iron staining along fissility. Striae on clast measured at 200°. Lower contact is gradational. Subglacial traction till. |
| 3: Dmm | Grey-Brown with flakey texture and coarse fissility. Iron staining along fissility and within till. Blockier than above unit. Well-defined boulder pavement at sharp base contact. Subglacial traction till. |
| BL | |
| 2: Dmm | Grey, over-compacted diamicton with coarse fissility, and cobbles throughout. Striae on boulder trending 173° measured at 4.1 m. Moderately-defined boulder pavement at base. Subglacial traction till. |
| BL | |
| 1: Dmm, Sm | Grey, over-compacted with coarse fissility. Iron staining in lenses and along joints. Clasts smaller than above unit. Pipe flow feature at 5.4 m and sand filled, steep fractures. No lower contact seen. Subglacial traction till. |

| Sample | Colour | Oxide Cluster | PSA Cluster | CC Cluster |
|---|---|---|---|---|
| AJ116319 | B | 4 | 1 | 4 |
| AJ122419 | GB | 4 | 1 | 4 |
| AJ119619 | G | 4 | 2 | 2 |
| AJ118619 | G | 1 | 2 | 3 |

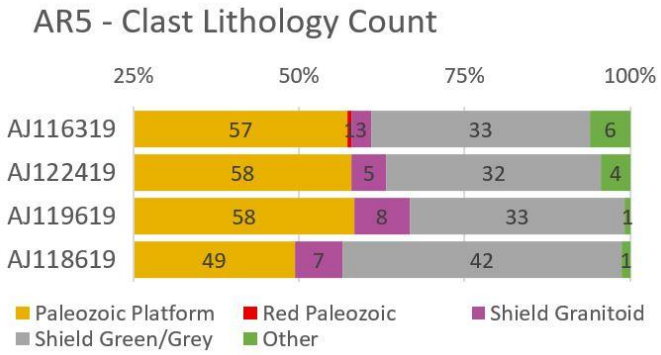


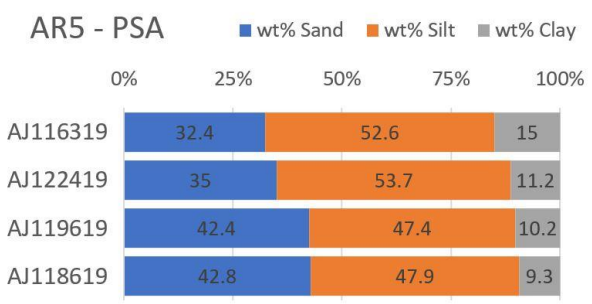

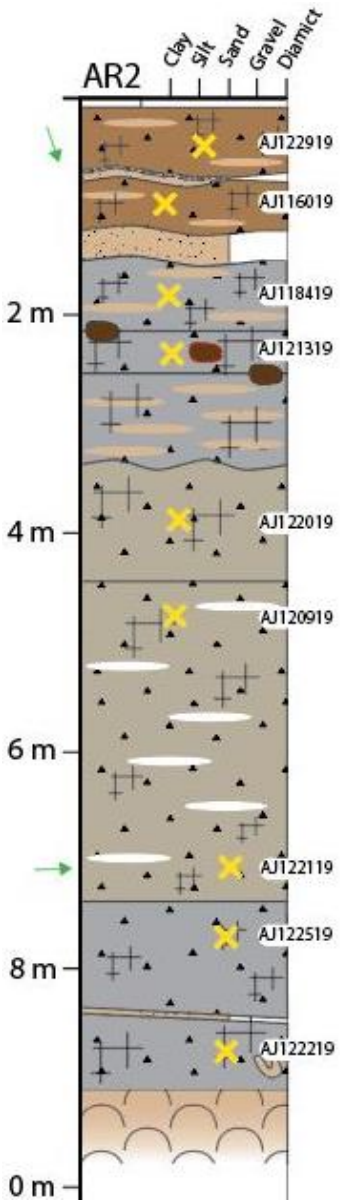


NAD 83 UTM Zone 16: 601518E 5723671N

| Unit: Lithofacies Code | Description and Interpretation |
|---|---|
| 9: Dmm, Sm | Brown with fine, crumbly fissility, sand lenses and iron staining throughout. Minor lag and sand lense at sharp, undulous, base contact. Subglacial traction till. |
| 8: Dmm, Sm | Brown with fine fissility. Thin sand lenses up to 5 cm thick. Iron staining along horizontal fissility. Base contact defined by undulous sand layer. Subglacial traction till. |
| Sm | Grey and sandy with oxidation along fine, horizontal fissility and around large cobbles. Coarse, isolated, sand lenses up to 10 cm thick. Sharp basal contact with large cobble. |
| 7: Dmm, Sm | Subglacial traction till. |
| 6: Dmm | Grey with coarse fissility and minor iron staining along fissility. Large sulphide boulder with stained, 3 cm halo. Differentiated from above unit by colour. Sharp lower contact has cobble. Subglacial traction till. |
| 5: Dmm, Sm | Grey with extensive interbedded rusty sand layers and coarse fissility. Subglacial traction till. |
| 4: Dmm | Grey-Brown and very blocky with coarse fissility. Lots of small gravel but very few cobble-sized clasts. Sharp lower contact. Subglacial traction till. |
| 3: Dmm, Sm | Grey-Brown with high sand content and lenses of white, medium-grained sand throughout. Fissility, pebble content, and compaction decrease with depth. Minor sulphide clasts present but no iron staining. Sharp lower contact. Subglacial traction till. |
| 2: Dmm | Grey with moderate compaction, moderate to coarse fissility, but crumbles very easily with finer fissility than above unit. More pebbles than cobbles with mixed lithology. Sharp lower contact dipping to the west with sand bed. Subglacial traction till. |
| Sm | |
| 1: Dmm, Sm | Grey and blocky with coarse fissility. Iron staining around many pebbles with variable lithologies. Sulfide clasts present in minor amounts. Contains isolated and truncated folds of sand and till including a large pipe flow feature. No lower contact seen. Subglacial traction till. |

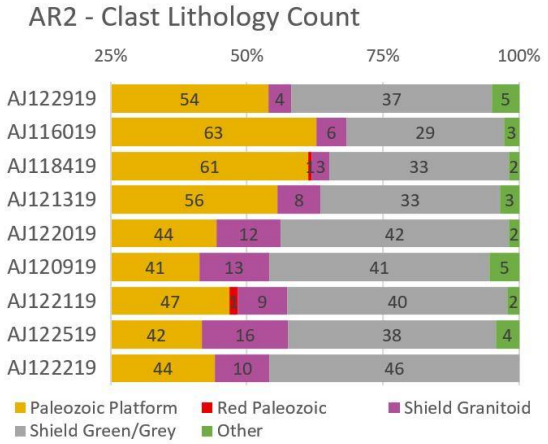


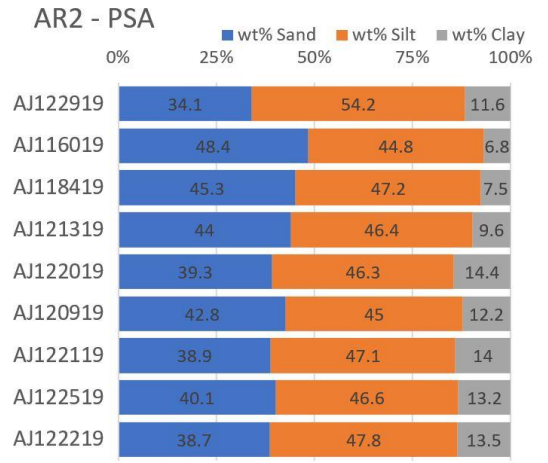


| Sample | Colour | Oxide | PSA | CC |
|---|---|---|---|---|
| AJ122919 | B | 4 | 1 | 4 |
| AJ116019 | B | 4 | 2 | 4 |
| AJ118419 | G | 4 | 2 | 4 |
| AJ121319 | G | 4 | 2 | 3 |
| | G | | | |
| AJ122019 | GB | 2 | 1 | 3 |
| AJ120919 | GB | 2 | 1 | 3 |
| AJ122119 | GB | 2 | 1 | 3 |
| AJ122519 | G | 2 | 1 | 3 |
| AJ122219 | G | 2 | 1 | 2 |

# Appendix B. Clast Fabrics

Clast fabric statistics. Red principal S1 values are ≥0.54 so deemed directionally significant.

| ID | n | S1 | Isotropy | Elongation | R | V1_trend | V1_plunge |
|---|---|---|---|---|---|---|---|
| **AR11_F1** | 50 | **0.635398** | 0.1421 | 0.5683 | 0.29 | 8.9 | 1.4 |
| **AR11_F2** | 50 | **0.542895** | 0.3003 | 0.4583 | 0.24 | 344.4 | 19.3 |
| **AR11_F3** | 50 | 0.477238 | 0.3694 | 0.274 | 0.36 | 2.1 | 18 |
| **AR2_F1** | 50 | **0.540314** | 0.2179 | 0.3672 | 0.41 | 341.2 | 3.8 |
| **AR2_F3** | 50 | 0.525452 | 0.1482 | 0.2451 | 0.61 | 331.3 | 4.6 |
| **AR2_F6** | 50 | 0.448997 | 0.4822 | 0.255 | 0.26 | 43 | 5.3 |
| **AR2_F7** | 50 | **0.548663** | 0.3617 | 0.5391 | 0.1 | 267.7 | 13.7 |
| **AR2_F9** | 50 | 0.480789 | 0.2736 | 0.1937 | 0.53 | 206.2 | 5.1 |
| **AR5_F1** | 50 | **0.638275** | 0.1092 | 0.5424 | 0.35 | 181.5 | 0 |
| **AR5_F2** | 50 | **0.558292** | 0.1981 | 0.407 | 0.39 | 161.7 | 4.9 |
| **AR6_F1** | 51 | 0.53088 | 0.2323 | 0.3486 | 0.42 | 175.4 | 5.5 |
| **AR6_F2** | 50 | 0.470739 | 0.3585 | 0.2342 | 0.41 | 302.5 | 13.7 |
| **AR6_F3** | 50 | 0.538421 | 0.3431 | 0.4859 | 0.17 | 89.9 | 0.8 |
| **AR6_F4** | 50 | 0.412606 | 0.5558 | 0.1323 | 0.31 | 22.6 | 21.3 |
| **AR9_F1** | 50 | **0.676089** | 0.1336 | 0.6545 | 0.21 | 155.8 | 6.5 |
| **AR9_F2** | 49 | **0.648006** | 0.1634 | 0.6202 | 0.22 | 185.3 | 11.2 |
| **AR9B_F1** | 49 | 0.456946 | 0.5043 | 0.3158 | 0.18 | 146.6 | 18.3 |
| **AR9B_F2** | 50 | 0.481944 | 0.3266 | 0.2516 | 0.42 | 172.8 | 6.9 |
| **AR9B_F3** | 50 | 0.508841 | 0.305 | 0.3397 | 0.36 | 157 | 3.7 |
| **DR2_F1** | 50 | 0.530257 | 0.2692 | 0.3833 | 0.35 | 194.8 | 14.8 |
| **DR2_F2** | 50 | **0.548331** | 0.1854 | 0.3617 | 0.45 | 183.7 | 1.1 |
| **DR2_F3** | 50 | **0.696238** | 0.1321 | 0.6958 | 0.17 | 157.2 | 4.7 |
| **DR2_F4** | 50 | 0.510788 | 0.269 | 0.3112 | 0.42 | 301.4 | 4.4 |
| **OR2_F1** | 50 | **0.649115** | 0.149 | 0.6085 | 0.24 | 92.1 | 29.9 |
| **OR2_F2** | 53 | 0.507136 | 0.3355 | 0.3636 | 0.3 | 77.8 | 2 |
| **OR2_F3** | 50 | 0.504802 | 0.3592 | 0.3782 | 0.26 | 160.5 | 13.9 |
| **OR2_F4** | 50 | 0.53341 | 0.3349 | 0.4601 | 0.21 | 91.1 | 4.1 |
| **OR2_F5** | 51 | 0.430473 | 0.4223 | 0.0993 | 0.48 | 124.7 | 5.5 |
| **OR3_F1** | 50 | **0.557833** | 0.1786 | 0.3859 | 0.44 | 60 | 15.8 |
| **OR3_F2** | 50 | 0.516089 | 0.2189 | 0.2813 | 0.5 | 174.2 | 10 |
| **OR3_F3** | 50 | 0.503782 | 0.2877 | 0.3027 | 0.41 | 21.6 | 6.4 |
| **OR3_F4** | 50 | 0.487183 | 0.3337 | 0.2811 | 0.39 | 328.4 | 26.6 |
| **OR3_F5** | 50 | 0.471206 | 0.4276 | 0.3054 | 0.27 | 54.9 | 11.7 |
| **OR3_F6** | 50 | 0.48003 | 0.2836 | 0.2004 | 0.52 | 329.6 | 23.6 |
| **OR4_F1** | 50 | 0.517884 | 0.3636 | 0.4327 | 0.2 | 298.2 | 2.9 |
| **OR4_F2** | 51 | 0.534567 | 0.1765 | 0.3058 | 0.52 | 87.7 | 7.8 |
| **OR4_F3** | 50 | **0.640589** | 0.1193 | 0.5583 | 0.32 | 197.8 | 3.5 |
| **OR4_F4** | 50 | **0.594609** | 0.125 | 0.4432 | 0.43 | 65 | 2.8 |
| **OR4_F5** | 50 | 0.49896 | 0.2984 | 0.2942 | 0.41 | 356.5 | 1.9 |

# Appendix C. Clast Counts

Raw clast counts per lithology group.

| Sample | Shield Granitoid | Paleozoic Platform | Red Paleozoic | Shield Green/Grey | Other |
|---|---|---|---|---|---|
| **AJ119819** | 6 | 57 | 9 | 27 | 1 |
| **AJ119119** | 11 | 58 | 9 | 21 | 1 |
| **AJ123419** | 12 | 54 | 1 | 33 | 1 |
| **AJ120019** | 6 | 51 | 0 | 43 | 1 |
| **AJ115819** | 5 | 65 | 0 | 27 | 3 |
| **AJ118619** | 7 | 49 | 0 | 42 | 1 |
| **AJ121619** | 11 | 54 | 0 | 34 | 2 |
| **AJ121019** | 9 | 49 | 1 | 39 | 2 |
| **AJ117619** | 8 | 66 | 0 | 25 | 1 |
| **AJ115519** | 6 | 67 | 16 | 9 | 1 |
| **AJ119019** | 11 | 62 | 2 | 23 | 2 |
| **AJ119719** | 5 | 66 | 13 | 16 | 0 |
| **AJ120619** | 8 | 55 | 0 | 36 | 2 |
| **AJ119919** | 9 | 63 | 1 | 27 | 1 |
| **AJ121819** | 6 | 62 | 5 | 26 | 1 |
| **AJ120819** | 13 | 55 | 0 | 29 | 3 |
| **AJ119319** | 3 | 56 | 1 | 39 | 1 |
| **AJ120419** | 7 | 46 | 0 | 44 | 3 |
| **AJ123519** | 10 | 45 | 1 | 43 | 1 |
| **AJ121919** | 12 | 60 | 8 | 20 | 0 |
| **AJ123319** | 13 | 52 | 1 | 30 | 4 |
| **AJ118419** | 3 | 61 | 1 | 33 | 2 |
| **AJ118519** | 3 | 53 | 0 | 40 | 4 |
| **AJ122919** | 4 | 54 | 0 | 37 | 5 |
| **AJ123619** | 1 | 60 | 12 | 26 | 1 |
| **AJ119619** | 8 | 58 | 0 | 33 | 1 |
| **AJ120719** | 6 | 63 | 0 | 30 | 2 |
| **AJ116019** | 6 | 63 | 0 | 29 | 3 |
| **AJ122219** | 10 | 44 | 0 | 46 | 0 |
| **AJ119219** | 8 | 57 | 0 | 33 | 2 |
| **AJ120319** | 6 | 62 | 2 | 30 | 0 |
| **AJ121319** | 8 | 56 | 0 | 33 | 3 |
| **AJ122019** | 12 | 44 | 0 | 42 | 2 |
| **AJ122119** | 9 | 47 | 1 | 40 | 2 |
| **AJ121419** | 7 | 57 | 2 | 34 | 0 |
| **AJ123019** | 12 | 65 | 7 | 15 | 1 |
| **AJ121219** | 8 | 63 | 10 | 18 | 1 |

| | | | | | |
|---|---|---|---|---|---|
| **AJ121519** | 13 | 52 | 0 | 34 | 1 |
| **AJ118819** | 10 | 52 | 0 | 37 | 1 |
| **AJ121119** | 17 | 50 | 0 | 30 | 3 |
| **AJ116719** | 6 | 70 | 1 | 23 | 0 |
| **AJ123119** | 5 | 49 | 0 | 39 | 7 |
| **AJ120919** | 13 | 41 | 0 | 41 | 5 |
| **AJ120219** | 14 | 66 | 11 | 8 | 2 |
| **AJ115419** | 10 | 61 | 9 | 19 | 2 |
| **AJ122419** | 5 | 58 | 0 | 32 | 4 |
| **AJ121719** | 11 | 65 | 17 | 6 | 1 |
| **AJ122519** | 16 | 42 | 0 | 38 | 4 |
| **AJ116319** | 3 | 57 | 1 | 33 | 6 |

# Appendix D. Laboratory Results

Till matrix geochemistry and particle size analysis details performed by the SRC and results.

| Analysis | Process | Outputs |
|---|---|---|
| **Particle Size Analysis** | Wt % of dried material | Sand, silt, clay |
| **Ca/Mg** | 0.5 g of pulp digested overnight in 2 ml of HCl at room temperature | Ca, Mg, Dol, Cal, $CO_3$, Dol/Cal, $CO_2$Cal , $CO_2$Dol , $CO_2$Tot |
| **ICP Total Digestion** | 0.125 g of pulp is heated in ultrapure $HF/HNO_3/HClO_4$ until dry and then dissolved in dilute ultrapure $HNO_3$ | Al2O3, Ba, CaO, Ce, Cr, Fe2O3, K2O, La, Li, MgO, MnO, Na2O, $P_2O_5$, S, Sr, TiO2, V, Zr |
| **ICP-MS Total Digestion** | | Ag, Be, Bi, Cd, Co, Cs, Cu, Dy, Er, Eu, Ga, Gd, Hf, Ho, Mo, Nb, Nd, Ni, $^{204}$Pb, $^{206}$Pb, $^{207}$Pb, $^{208}$Pb, SUMPb, Pr, Rb, Sc, Sm, Sn, Ta, Tb, Th, U, W, Y, Yb, Zn |
| **ICP-MS Partial Digestion** | 0.5 g of pulp is digested for 1 hour in 2.25 ml of ultrapure $HNO_3$:HCl (8:1) at 95˚C | Ag, As, Be, Bi, Cd, Co, Cs, Cu, Dy, Er, Eu, Ga, Gd, Ge, Hf, Hg, Ho, Mo, Nb, Nd, Ni, $^{204}$Pb, $^{206}$Pb, $^{207}$Pb, $^{208}$Pb, SUMPb, Pr, Rb, Sb, Sc, Se, Sm, Sn, Ta, Tb, Te, Th, U, V, W, Y, Yb, Zn, Zr |

SRC Geoanalytical Laboratories
125 - 15 Innovation Blvd., Saskatoon, Saskatchewan, S7N 2X8
Tel: (306) 933-8118  Fax: (306) 933-8118  Email: geolab@src.sk.ca

De Beers Canada Exploration Inc.
Attention: Natasha Oviatt
Dispatch:
PO #/Project: CAN190302
Samples: 54

| | | | | Sand Particle Size Analysis | Silt Particle Size Analysis | Clay Particle Size Analysis |
|---|---|---|---|---|---|---|
| | | | | wt % | wt % | wt % |
| Group # | Description | Date | Sample Type | | | |
| G-2019-1868 | SSC0219 | 10-02-2019 | Standard | 25.4 | 45.6 | 29 |
| G-2019-1868 | AJ115419 (-2mm) | 10-02-2019 | Soil | 26.3 | 50.3 | 23.4 |
| G-2019-1868 | AJ115519 (-2mm) | 10-02-2019 | Soil | 26.7 | 53.3 | 20 |
| G-2019-1868 | AJ115819 (-2mm) | 10-02-2019 | Soil | 34 | 52.9 | 13 |
| G-2019-1868 | AJ116019 (-2mm) | 10-02-2019 | Soil | 48.4 | 44.8 | 6.8 |
| G-2019-1868 | AJ116319 (-2mm) | 10-02-2019 | Soil | 32.4 | 52.6 | 15 |
| G-2019-1868 | AJ116719 (-2mm) | 10-02-2019 | Soil | 20.4 | 52.1 | 27.4 |
| G-2019-1868 | AJ117619 (-2mm) | 10-02-2019 | Soil | 30.5 | 55.1 | 14.4 |
| G-2019-1868 | AJ118419 (-2mm) | 10-02-2019 | Soil | 45.3 | 47.2 | 7.5 |
| G-2019-1868 | AJ118519 (-2mm) | 10-02-2019 | Soil | 36.4 | 52.5 | 11.1 |
| G-2019-1868 | AJ118619 (-2mm) | 10-02-2019 | Soil | 42.8 | 47.9 | 9.3 |
| G-2019-1868 | AJ118819 (-2mm) | 10-02-2019 | Soil | 39.9 | 49.6 | 10.6 |
| G-2019-1868 | AJ119019 (-2mm) | 10-02-2019 | Soil | 31.9 | 54.9 | 13.2 |
| G-2019-1868 | AJ119119 (-2mm) | 10-02-2019 | Soil | 23.5 | 52.8 | 23.8 |
| G-2019-1868 | AJ119219 (-2mm) | 10-02-2019 | Soil | 34.4 | 54.1 | 11.4 |
| G-2019-1868 | AJ119319 (-2mm) | 10-02-2019 | Soil | 36.9 | 51.9 | 11.2 |
| G-2019-1868 | AJ119619 (-2mm) | 10-02-2019 | Soil | 42.4 | 47.4 | 10.2 |
| G-2019-1868 | AJ119719 (-2mm) | 10-02-2019 | Soil | 27.9 | 51.2 | 20.9 |
| G-2019-1868 | AJ119819 (-2mm) | 10-02-2019 | Soil | 21.1 | 56 | 23 |
| G-2019-1868 | AJ119919 (-2mm) | 10-02-2019 | Soil | 32.7 | 55.1 | 12.2 |
| G-2019-1868 | SSC0219 | 10-02-2019 | Standard | 25.4 | 45.7 | 28.9 |
| G-2019-1868 | AJ120019 (-2mm) | 10-02-2019 | Soil | 76.1 | 20.4 | 3.6 |
| G-2019-1868 | AJ120219 (-2mm) | 10-02-2019 | Soil | 26.2 | 55.2 | 18.6 |
| G-2019-1868 | AJ120319 (-2mm) | 10-02-2019 | Soil | 37.4 | 56.2 | 6.4 |
| G-2019-1868 | AJ120419 (-2mm) | 10-02-2019 | Soil | 37.4 | 52.5 | 10.2 |
| G-2019-1868 | AJ120619 (-2mm) | 10-02-2019 | Soil | 31.8 | 55.4 | 12.8 |
| G-2019-1868 | AJ120719 (-2mm) | 10-02-2019 | Soil | 64.1 | 31.1 | 4.8 |
| G-2019-1868 | AJ120819 (-2mm) | 10-02-2019 | Soil | 88.6 | 9.5 | 2 |
| G-2019-1868 | AJ120919 (-2mm) | 10-02-2019 | Soil | 42.8 | 45 | 12.2 |
| G-2019-1868 | AJ121019 (-2mm) | 10-02-2019 | Soil | 47.8 | 41.2 | 11 |
| G-2019-1868 | AJ121119 (-2mm) | 10-02-2019 | Soil | 38.5 | 47.7 | 13.8 |
| G-2019-1868 | AJ121219 (-2mm) | 10-02-2019 | Soil | 22.7 | 52.8 | 24.5 |
| G-2019-1868 | AJ121319 (-2mm) | 10-02-2019 | Soil | 44 | 46.4 | 9.6 |
| G-2019-1868 | AJ121419 (-2mm) | 10-02-2019 | Soil | 27.9 | 49.9 | 22.2 |
| G-2019-1868 | AJ121519 (-2mm) | 10-02-2019 | Soil | 35.6 | 55.8 | 8.6 |
| G-2019-1868 | AJ121619 (-2mm) | 10-02-2019 | Soil | 34.7 | 53.4 | 12 |
| G-2019-1868 | AJ121719 (-2mm) | 10-02-2019 | Soil | 26.9 | 53.7 | 19.4 |
| G-2019-1868 | AJ121819 (-2mm) | 10-02-2019 | Soil | 19.9 | 53.1 | 27 |
| G-2019-1868 | AJ121919 (-2mm) | 10-02-2019 | Soil | 23.2 | 57.1 | 19.7 |
| G-2019-1868 | AJ121819 (-2mm) R | 10-02-2019 | Repeat | 19.7 | 53.3 | 27 |
| G-2019-1868 | SSC0219 | 10-02-2019 | Standard | 25.2 | 46 | 28.8 |
| G-2019-1868 | AJ122019 (-2mm) | 10-02-2019 | Soil | 39.3 | 46.3 | 14.4 |
| G-2019-1868 | AJ122119 (-2mm) | 10-02-2019 | Soil | 38.9 | 47.1 | 14 |
| G-2019-1868 | AJ122219 (-2mm) | 10-02-2019 | Soil | 38.7 | 47.8 | 13.5 |
| G-2019-1868 | AJ122419 (-2mm) | 10-02-2019 | Soil | 35 | 53.7 | 11.2 |
| G-2019-1868 | AJ122519 (-2mm) | 10-02-2019 | Soil | 40.1 | 46.6 | 13.2 |
| G-2019-1868 | AJ122919 (-2mm) | 10-02-2019 | Soil | 34.1 | 54.2 | 11.6 |
| G-2019-1868 | AJ123019 (-2mm) | 10-02-2019 | Soil | 23.3 | 52.2 | 24.4 |
| G-2019-1868 | AJ123119 (-2mm) | 10-02-2019 | Soil | 36 | 52.7 | 11.3 |
| G-2019-1868 | AJ123319 (-2mm) | 10-02-2019 | Soil | 35.5 | 53.7 | 10.8 |
| G-2019-1868 | AJ123419 (-2mm) | 10-02-2019 | Soil | 35.1 | 53.4 | 11.4 |
| G-2019-1868 | AJ123519 (-2mm) | 10-02-2019 | Soil | 34.4 | 49.8 | 15.8 |
| G-2019-1868 | AJ123619 (-2mm) | 10-02-2019 | Soil | 24 | 55 | 21 |
| G-2019-1868 | AJ123619 (-2mm) R | 10-02-2019 | Repeat | 23.2 | 55 | 21.8 |

| | | | | Al2O3 ICP Total Digestion | Ba ICP Total Digestion | CaO ICP Total Digestion | Ce ICP Total Digestion | Cr ICP Total Digestion | Fe2O3 ICP Total Digestion | K2O ICP Total Digestion | La ICP Total Digestion | Li ICP Total Digestion | MgO ICP Total Digestion | MnO ICP Total Digestion | Na2O ICP Total Digestion | P2O5 ICP Total Digestion |
|---|---|---|---|---|---|---|---|---|---|---|---|---|---|---|---|---|
| | | | | wt % | ppm | wt % | ppm | ppm | wt % | wt % | ppm | ppm | wt % | wt % | wt % | wt % |
| Group # | Description | Date | Sample Type | | | | | | | | | | | | | |
| G-2019-1869 | DCB01/BR2 | 10-04-2019 | Standard | 11.1 | 382 | 1.51 | 126 | 258 | 3.35 | 2.41 | 64 | 43 | 1.7 | 0.036 | 0.56 | 0.208 |
| G-2019-1869 | AJ115419 (-63µm) | 10-04-2019 | Basement | 10.5 | 449 | 17.8 | 59 | 51 | 3.8 | 2.67 | 30 | 39 | 5.31 | 0.056 | 1.35 | 0.127 |
| G-2019-1869 | AJ115519 (-63µm) | 10-04-2019 | Basement | 9.92 | 435 | 18.3 | 58 | 44 | 3.4 | 2.69 | 29 | 37 | 5.87 | 0.053 | 1.24 | 0.136 |
| G-2019-1869 | AJ115819 (-63µm) | 10-04-2019 | Basement | 8.15 | 383 | 22.8 | 41 | 35 | 2.61 | 2.09 | 21 | 24 | 6.23 | 0.045 | 1.44 | 0.118 |
| G-2019-1869 | AJ116019 (-63µm) | 10-04-2019 | Basement | 7.75 | 390 | 19.2 | 37 | 30 | 2.27 | 2.07 | 20 | 16 | 6.68 | 0.044 | 1.5 | 0.115 |
| G-2019-1869 | AJ116319 (-63µm) | 10-04-2019 | Basement | 8.41 | 383 | 22.6 | 44 | 35 | 2.77 | 2.06 | 23 | 23 | 6.21 | 0.044 | 1.47 | 0.114 |
| G-2019-1869 | AJ116719 (-63µm) | 10-04-2019 | Basement | 11.4 | 492 | 16.4 | 58 | 60 | 4.19 | 2.62 | 32 | 40 | 5.09 | 0.055 | 1.73 | 0.143 |
| G-2019-1869 | AJ117619 (-63µm) | 10-04-2019 | Basement | 8.95 | 395 | 19.4 | 50 | 40 | 3 | 2.22 | 25 | 27 | 5.86 | 0.054 | 1.41 | 0.126 |
| G-2019-1869 | AJ118419 (-63µm) | 10-04-2019 | Basement | 7.74 | 382 | 19.6 | 41 | 31 | 2.3 | 2.05 | 21 | 17 | 6.63 | 0.044 | 1.5 | 0.119 |
| G-2019-1869 | AJ118519 (-63µm) | 10-04-2019 | Basement | 8.17 | 389 | 22 | 41 | 33 | 2.52 | 2.02 | 21 | 23 | 6.71 | 0.05 | 1.55 | 0.113 |
| G-2019-1869 | AJ118619 (-63µm) | 10-04-2019 | Basement | 8.86 | 437 | 18 | 45 | 37 | 2.49 | 2.1 | 23 | 18 | 5.31 | 0.048 | 1.76 | 0.13 |
| G-2019-1869 | AJ118819 (-63µm) | 10-04-2019 | Basement | 7.94 | 380 | 19.1 | 39 | 34 | 2.51 | 1.95 | 21 | 19 | 6.17 | 0.049 | 1.56 | 0.13 |
| G-2019-1869 | AJ119019 (-63µm) | 10-04-2019 | Basement | 8.34 | 387 | 22.2 | 45 | 35 | 2.67 | 2.15 | 24 | 25 | 6.04 | 0.044 | 1.42 | 0.118 |
| G-2019-1869 | AJ119119 (-63µm) | 10-04-2019 | Basement | 10.3 | 442 | 18.5 | 61 | 50 | 3.59 | 2.63 | 32 | 38 | 5.27 | 0.052 | 1.38 | 0.13 |
| G-2019-1869 | AJ119219 (-63µm) | 10-04-2019 | Basement | 7.77 | 358 | 22.2 | 39 | 33 | 2.43 | 1.96 | 20 | 23 | 6.45 | 0.043 | 1.39 | 0.117 |
| G-2019-1869 | AJ119319 (-63µm) | 10-04-2019 | Basement | 7.76 | 358 | 21.7 | 40 | 33 | 2.51 | 1.88 | 21 | 23 | 6.42 | 0.043 | 1.35 | 0.108 |
| G-2019-1869 | AJ119619 (-63µm) | 10-04-2019 | Basement | 8.52 | 406 | 21.4 | 45 | 34 | 2.66 | 2.09 | 23 | 23 | 6.38 | 0.051 | 1.6 | 0.123 |
| G-2019-1869 | AJ119719 (-63µm) | 10-04-2019 | Basement | 10.1 | 438 | 18.8 | 54 | 46 | 3.49 | 2.63 | 29 | 37 | 5.66 | 0.053 | 1.35 | 0.129 |
| G-2019-1869 | AJ119819 (-63µm) | 10-04-2019 | Basement | 9.79 | 427 | 20 | 58 | 43 | 3.27 | 2.45 | 29 | 31 | 5.46 | 0.056 | 1.44 | 0.132 |
| G-2019-1869 | AJ119919 (-63µm) | 10-04-2019 | Basement | 8.41 | 388 | 22 | 44 | 36 | 2.69 | 2.17 | 22 | 25 | 6.09 | 0.045 | 1.42 | 0.121 |
| G-2019-1869 | DCB01/BR2 | 10-04-2019 | Standard | 11 | 384 | 1.51 | 130 | 264 | 3.35 | 2.44 | 63 | 43 | 1.7 | 0.036 | 0.57 | 0.211 |
| G-2019-1869 | AJ120019 (-63µm) | 10-04-2019 | Basement | 8.62 | 411 | 21.1 | 49 | 35 | 2.98 | 2.13 | 25 | 22 | 6.18 | 0.084 | 1.55 | 0.13 |
| G-2019-1869 | AJ120219 (-63µm) | 10-04-2019 | Basement | 10.5 | 440 | 18.5 | 59 | 50 | 3.66 | 2.87 | 31 | 39 | 6.13 | 0.056 | 1.34 | 0.13 |
| G-2019-1869 | AJ120319 (-63µm) | 10-04-2019 | Basement | 7.62 | 379 | 22 | 41 | 29 | 2.11 | 2.01 | 21 | 18 | 5.97 | 0.042 | 1.51 | 0.115 |
| G-2019-1869 | AJ120419 (-63µm) | 10-04-2019 | Basement | 8.17 | 381 | 22.3 | 42 | 33 | 2.52 | 2.02 | 22 | 24 | 6.91 | 0.051 | 1.54 | 0.119 |
| G-2019-1869 | AJ120619 (-63µm) | 10-04-2019 | Basement | 8.07 | 369 | 24.1 | 41 | 32 | 2.54 | 2.05 | 22 | 22 | 6.36 | 0.043 | 1.48 | 0.116 |
| G-2019-1869 | AJ120719 (-63µm) | 10-04-2019 | Basement | 8.78 | 417 | 19.8 | 43 | 33 | 2.52 | 2.16 | 22 | 21 | 7.02 | 0.046 | 1.69 | 0.122 |
| G-2019-1869 | AJ120819 (-63µm) | 10-04-2019 | Basement | 8.75 | 400 | 20.5 | 44 | 34 | 2.54 | 2.08 | 23 | 22 | 6.93 | 0.048 | 1.58 | 0.124 |
| G-2019-1869 | AJ120919 (-63µm) | 10-04-2019 | Basement | 10.8 | 501 | 14.1 | 57 | 53 | 3.6 | 2.4 | 29 | 30 | 4.44 | 0.062 | 1.76 | 0.141 |
| G-2019-1869 | AJ121019 (-63µm) | 10-04-2019 | Basement | 10.1 | 462 | 16.4 | 50 | 44 | 3 | 2.34 | 26 | 25 | 5.75 | 0.047 | 1.77 | 0.131 |
| G-2019-1869 | AJ121119 (-63µm) | 10-04-2019 | Basement | 10.4 | 501 | 16.3 | 52 | 45 | 3.3 | 2.46 | 27 | 27 | 5.75 | 0.06 | 1.97 | 0.138 |
| G-2019-1869 | AJ121219 (-63µm) | 10-04-2019 | Basement | 11.3 | 465 | 19.1 | 64 | 53 | 4 | 2.85 | 33 | 43 | 5.6 | 0.063 | 1.45 | 0.134 |
| G-2019-1869 | AJ121319 (-63µm) | 10-04-2019 | Basement | 8.75 | 406 | 18.5 | 45 | 38 | 2.83 | 2.16 | 23 | 22 | 6.27 | 0.052 | 1.54 | 0.119 |
| G-2019-1869 | AJ121419 (-63µm) | 10-04-2019 | Basement | 11.7 | 501 | 14.2 | 66 | 63 | 4.3 | 2.6 | 34 | 38 | 4.76 | 0.059 | 1.86 | 0.142 |
| G-2019-1869 | AJ121519 (-63µm) | 10-04-2019 | Basement | 8.23 | 398 | 21.2 | 41 | 32 | 2.34 | 2.09 | 21 | 20 | 6.71 | 0.046 | 1.66 | 0.118 |
| G-2019-1869 | AJ121619 (-63µm) | 10-04-2019 | Basement | 8.33 | 374 | 23.1 | 43 | 37 | 2.7 | 2.04 | 22 | 26 | 7.18 | 0.05 | 1.47 | 0.119 |
| G-2019-1869 | AJ121719 (-63µm) | 10-04-2019 | Basement | 10.7 | 442 | 18.3 | 57 | 49 | 3.68 | 2.93 | 31 | 41 | 5.98 | 0.056 | 1.34 | 0.128 |
| G-2019-1869 | AJ121819 (-63µm) | 10-04-2019 | Basement | 11.9 | 491 | 17.3 | 69 | 57 | 4.23 | 2.96 | 34 | 43 | 5.2 | 0.067 | 1.58 | 0.14 |
| G-2019-1869 | AJ121919 (-63µm) | 10-04-2019 | Basement | 10 | 428 | 19.7 | 58 | 44 | 3.25 | 2.64 | 30 | 34 | 5.81 | 0.052 | 1.45 | 0.131 |
| G-2019-1869 | AJ121819 (-63µm) R | 10-04-2019 | Repeat | 11.7 | 490 | 17.1 | 67 | 55 | 4.2 | 2.94 | 33 | 41 | 5.18 | 0.066 | 1.5 | 0.138 |
| G-2019-1869 | DCB01/BR2 | 10-04-2019 | Standard | 11.1 | 387 | 1.5 | 130 | 250 | 3.31 | 2.46 | 64 | 43 | 1.7 | 0.035 | 0.58 | 0.211 |
| G-2019-1869 | AJ122019 (-63µm) | 10-04-2019 | Basement | 11.3 | 512 | 14.1 | 59 | 54 | 3.76 | 2.49 | 30 | 31 | 4.54 | 0.07 | 1.82 | 0.141 |
| G-2019-1869 | AJ122119 (-63µm) | 10-04-2019 | Basement | 11.1 | 502 | 14 | 59 | 52 | 3.69 | 2.45 | 31 | 31 | 4.48 | 0.064 | 1.8 | 0.143 |
| G-2019-1869 | AJ122219 (-63µm) | 10-04-2019 | Basement | 11.1 | 510 | 13.7 | 59 | 55 | 3.71 | 2.41 | 30 | 30 | 4.44 | 0.063 | 1.78 | 0.145 |
| G-2019-1869 | AJ122419 (-63µm) | 10-04-2019 | Basement | 8.05 | 373 | 24 | 42 | 34 | 2.55 | 2 | 22 | 22 | 6.52 | 0.045 | 1.46 | 0.115 |
| G-2019-1869 | AJ122519 (-63µm) | 10-04-2019 | Basement | 10.9 | 505 | 13.7 | 58 | 52 | 3.62 | 2.42 | 30 | 30 | 4.39 | 0.064 | 1.79 | 0.145 |
| G-2019-1869 | AJ122919 (-63µm) | 10-04-2019 | Basement | 7.68 | 349 | 21.9 | 42 | 31 | 2.5 | 1.89 | 22 | 22 | 6.35 | 0.044 | 1.33 | 0.112 |
| G-2019-1869 | AJ123019 (-63µm) | 10-04-2019 | Basement | 10.4 | 441 | 18.6 | 61 | 52 | 3.58 | 2.68 | 30 | 39 | 5.46 | 0.052 | 1.38 | 0.132 |
| G-2019-1869 | AJ123119 (-63µm) | 10-04-2019 | Basement | 7.72 | 352 | 22 | 42 | 33 | 2.47 | 1.92 | 22 | 23 | 6.31 | 0.043 | 1.34 | 0.112 |
| G-2019-1869 | AJ123319 (-63µm) | 10-04-2019 | Basement | 8.32 | 380 | 23.3 | 44 | 36 | 2.54 | 2.15 | 23 | 24 | 6.48 | 0.048 | 1.51 | 0.118 |
| G-2019-1869 | AJ123419 (-63µm) | 10-04-2019 | Basement | 8.29 | 373 | 22.1 | 45 | 35 | 2.49 | 2.14 | 24 | 24 | 6.1 | 0.043 | 1.48 | 0.115 |
| G-2019-1869 | AJ123519 (-63µm) | 10-04-2019 | Basement | 10.4 | 477 | 15.6 | 51 | 48 | 3.33 | 2.47 | 27 | 29 | 5.66 | 0.058 | 1.88 | 0.132 |
| G-2019-1869 | AJ123619 (-63µm) | 10-04-2019 | Basement | 10.3 | 449 | 18.7 | 57 | 48 | 3.4 | 2.58 | 29 | 35 | 5.65 | 0.049 | 1.56 | 0.127 |
| G-2019-1869 | AJ123619 (-63µm) R | 10-04-2019 | Repeat | 10.4 | 452 | 18.8 | 58 | 49 | 3.42 | 2.62 | 30 | 36 | 5.69 | 0.05 | 1.57 | 0.131 |

| | S ICP Total Digestion | Sr ICP Total Digestion | TiO2 ICP Total Digestion | V ICP Total Digestion | Zr ICP Total Digestion | Ag ICP MS Partial Digestion | As ICP MS Partial Digestion | Be ICP MS Partial Digestion | Bi ICP MS Partial Digestion | Cd ICP MS Partial Digestion | Co ICP MS Partial Digestion | Cs ICP MS Partial Digestion | Cu ICP MS Partial Digestion | Dy ICP MS Partial Digestion | Er ICP MS Partial Digestion | Eu ICP MS Partial Digestion |
|---|---|---|---|---|---|---|---|---|---|---|---|---|---|---|---|---|
| | ppm | ppm | wt % | ppm | ppm | ppm | ppm | ppm | ppm | ppm | ppm | ppm | ppm | ppm | ppm | ppm |
| Description | | | | | | | | | | | | | | | | |
| DCB01/BR2 | 3970 | 404 | 0.786 | 102 | 399 | 2.42 | 30.3 | 0.42 | 6.48 | 0.42 | 13.8 | 0.4 | 269 | 1.64 | 0.75 | 0.49 |
| AJ115419 (-63µm) | <10 | 211 | 0.5 | 65.3 | 123 | 0.02 | 3.08 | 0.49 | 0.14 | 0.07 | 6.97 | 0.92 | 15 | 1.62 | 0.79 | 0.53 |
| AJ115519 (-63µm) | <10 | 198 | 0.486 | 58.8 | 132 | 0.01 | 2.45 | 0.43 | 0.11 | 0.06 | 5.46 | 0.84 | 11.9 | 1.62 | 0.77 | 0.52 |
| AJ115819 (-63µm) | <10 | 217 | 0.408 | 46.2 | 122 | 0.02 | 1.85 | 0.3 | 0.07 | 0.07 | 3.78 | 0.49 | 10.1 | 1.26 | 0.61 | 0.4 |
| AJ116019 (-63µm) | 42 | 210 | 0.376 | 40.1 | 133 | 0.02 | 1.7 | 0.23 | 0.05 | 0.09 | 3.1 | 0.33 | 10.6 | 1.3 | 0.67 | 0.39 |
| AJ116319 (-63µm) | 14 | 215 | 0.41 | 48.2 | 124 | 0.02 | 1.97 | 0.32 | 0.06 | 0.07 | 4.28 | 0.49 | 11.2 | 1.28 | 0.64 | 0.4 |
| AJ116719 (-63µm) | <10 | 231 | 0.516 | 69.4 | 126 | 0.02 | 2.43 | 0.47 | 0.11 | 0.08 | 6.65 | 1.06 | 17.4 | 1.7 | 0.86 | 0.56 |
| AJ117619 (-63µm) | <10 | 206 | 0.446 | 51.8 | 120 | 0.03 | 2.11 | 0.38 | 0.08 | 0.07 | 5.16 | 0.6 | 11.8 | 1.51 | 0.74 | 0.47 |
| AJ118419 (-63µm) | 40 | 210 | 0.381 | 41.7 | 120 | 0.02 | 1.67 | 0.2 | 0.04 | 0.09 | 3.14 | 0.35 | 9.57 | 1.32 | 0.67 | 0.39 |
| AJ118519 (-63µm) | 50 | 219 | 0.398 | 45.3 | 126 | 0.03 | 1.73 | 0.29 | 0.06 | 0.08 | 3.75 | 0.43 | 9.89 | 1.29 | 0.65 | 0.4 |
| AJ118619 (-63µm) | 215 | 239 | 0.409 | 46.8 | 166 | 0.03 | 1.49 | 0.26 | 0.05 | 0.1 | 3.81 | 0.41 | 9.66 | 1.27 | 0.65 | 0.38 |
| AJ118819 (-63µm) | 264 | 223 | 0.407 | 44.4 | 155 | 0.03 | 1.59 | 0.19 | 0.05 | 0.07 | 3.79 | 0.37 | 9.48 | 1.16 | 0.58 | 0.36 |
| AJ119019 (-63µm) | <10 | 216 | 0.418 | 47.1 | 116 | 0.01 | 1.99 | 0.26 | 0.07 | 0.07 | 3.6 | 0.59 | 9.65 | 1.35 | 0.65 | 0.44 |
| AJ119119 (-63µm) | 46 | 215 | 0.503 | 62.3 | 121 | 0.02 | 2.38 | 0.38 | 0.11 | 0.07 | 5.42 | 1 | 12 | 1.7 | 0.82 | 0.58 |
| AJ119219 (-63µm) | 232 | 208 | 0.392 | 44.1 | 114 | 0.03 | 1.66 | 0.26 | 0.06 | 0.08 | 3.61 | 0.52 | 10.2 | 1.3 | 0.65 | 0.42 |
| AJ119319 (-63µm) | <10 | 200 | 0.375 | 45 | 111 | 0.03 | 1.86 | 0.29 | 0.06 | 0.08 | 3.36 | 0.49 | 9.93 | 1.37 | 0.68 | 0.44 |
| AJ119619 (-63µm) | 175 | 226 | 0.414 | 48.9 | 122 | 0.03 | 1.7 | 0.3 | 0.05 | 0.08 | 3.74 | 0.5 | 10.2 | 1.38 | 0.7 | 0.44 |
| AJ119719 (-63µm) | <10 | 212 | 0.498 | 61.4 | 121 | 0.01 | 2.56 | 0.43 | 0.1 | 0.07 | 5.28 | 0.97 | 11.3 | 1.68 | 0.81 | 0.57 |
| AJ119819 (-63µm) | <10 | 218 | 0.488 | 57.8 | 119 | 0.02 | 2.17 | 0.38 | 0.09 | 0.07 | 5.03 | 0.9 | 11.5 | 1.67 | 0.82 | 0.57 |
| AJ119919 (-63µm) | <10 | 217 | 0.423 | 47.9 | 115 | 0.02 | 1.93 | 0.27 | 0.06 | 0.07 | 3.58 | 0.62 | 9.52 | 1.41 | 0.7 | 0.46 |
| DCB01/BR2 | 3980 | 409 | 0.796 | 101 | 410 | 2.47 | 30.6 | 0.45 | 6.78 | 0.44 | 13.4 | 0.42 | 267 | 1.73 | 0.79 | 0.52 |
| AJ120019 (-63µm) | 69 | 225 | 0.44 | 49 | 155 | 0.02 | 4.42 | 0.31 | 0.08 | 0.1 | 7.15 | 0.58 | 18.4 | 1.3 | 0.66 | 0.42 |
| AJ120219 (-63µm) | 93 | 207 | 0.52 | 62.6 | 120 | 0.03 | 2.64 | 0.37 | 0.11 | 0.09 | 5.55 | 0.91 | 11.8 | 1.73 | 0.83 | 0.58 |
| AJ120319 (-63µm) | <10 | 222 | 0.4 | 39 | 124 | 0.01 | 1.32 | 0.21 | 0.05 | 0.06 | 3.25 | 0.47 | 8.27 | 1.24 | 0.62 | 0.4 |
| AJ120419 (-63µm) | 35 | 219 | 0.4 | 45.9 | 124 | 0.03 | 1.62 | 0.3 | 0.06 | 0.08 | 3.82 | 0.45 | 9.87 | 1.36 | 0.68 | 0.42 |
| AJ120619 (-63µm) | <10 | 221 | 0.399 | 46.1 | 108 | 0.02 | 2.1 | 0.24 | 0.05 | 0.07 | 3.34 | 0.49 | 9.26 | 1.29 | 0.64 | 0.41 |
| AJ120719 (-63µm) | 14 | 230 | 0.412 | 46 | 127 | 0.02 | 1.38 | 0.21 | 0.04 | 0.06 | 2.8 | 0.44 | 8.89 | 1.26 | 0.64 | 0.4 |
| AJ120819 (-63µm) | <10 | 223 | 0.374 | 45.3 | 113 | 0.02 | 1.74 | 0.29 | 0.05 | 0.08 | 3.14 | 0.45 | 11.1 | 1.51 | 0.76 | 0.49 |
| AJ120919 (-63µm) | 203 | 226 | 0.515 | 66.3 | 152 | 0.04 | 1.87 | 0.38 | 0.08 | 0.12 | 5.68 | 0.68 | 13.8 | 1.67 | 0.87 | 0.53 |
| AJ121019 (-63µm) | 80 | 235 | 0.449 | 56.4 | 135 | 0.03 | 1.53 | 0.31 | 0.06 | 0.08 | 4.48 | 0.65 | 13.2 | 1.5 | 0.75 | 0.48 |
| AJ121119 (-63µm) | 291 | 260 | 0.436 | 57.4 | 144 | 0.03 | 1.45 | 0.32 | 0.06 | 0.09 | 4.86 | 0.68 | 12.2 | 1.4 | 0.7 | 0.46 |
| AJ121219 (-63µm) | <10 | 222 | 0.532 | 69 | 128 | 0.02 | 2.52 | 0.52 | 0.11 | 0.08 | 6.48 | 1.03 | 13.6 | 1.78 | 0.86 | 0.6 |
| AJ121319 (-63µm) | 12 | 211 | 0.414 | 50.3 | 134 | 0.03 | 1.74 | 0.32 | 0.05 | 0.1 | 3.85 | 0.48 | 10.6 | 1.49 | 0.76 | 0.46 |
| AJ121419 (-63µm) | <10 | 228 | 0.534 | 72.7 | 133 | 0.03 | 2.41 | 0.58 | 0.11 | 0.08 | 6.95 | 1.13 | 17.3 | 1.94 | 0.99 | 0.64 |
| AJ121519 (-63µm) | 158 | 230 | 0.4 | 44.3 | 131 | 0.03 | 1.4 | 0.2 | 0.05 | 0.07 | 3.15 | 0.42 | 8.17 | 1.25 | 0.63 | 0.41 |
| AJ121619 (-63µm) | <10 | 214 | 0.402 | 48.8 | 113 | 0.03 | 1.77 | 0.29 | 0.06 | 0.08 | 3.5 | 0.52 | 9.72 | 1.41 | 0.68 | 0.44 |
| AJ121719 (-63µm) | <10 | 209 | 0.516 | 64 | 123 | 0.02 | 2.65 | 0.43 | 0.1 | 0.08 | 5.26 | 1.03 | 11 | 1.76 | 0.85 | 0.61 |
| AJ121819 (-63µm) | <10 | 227 | 0.562 | 73.9 | 127 | 0.02 | 2.49 | 0.47 | 0.11 | 0.06 | 6.47 | 1.11 | 14.2 | 1.82 | 0.89 | 0.63 |
| AJ121919 (-63µm) | <10 | 221 | 0.513 | 58.4 | 131 | 0.01 | 2.16 | 0.3 | 0.09 | 0.07 | 4.48 | 0.92 | 9.86 | 1.62 | 0.76 | 0.54 |
| AJ121819 (-63µm) R | <10 | 221 | 0.557 | 72.9 | 125 | 0.02 | 2.56 | 0.51 | 0.12 | 0.07 | 6.57 | 1.15 | 14.1 | 1.89 | 0.92 | 0.66 |
| DCB01/BR2 | 3920 | 409 | 0.79 | 101 | 411 | 2.42 | 30.1 | 0.46 | 6.71 | 0.45 | 13.6 | 0.43 | 268 | 1.7 | 0.79 | 0.51 |
| AJ122019 (-63µm) | 203 | 231 | 0.529 | 69.5 | 154 | 0.04 | 2 | 0.47 | 0.1 | 0.13 | 6.33 | 0.68 | 15.3 | 1.66 | 0.85 | 0.54 |
| AJ122119 (-63µm) | 177 | 230 | 0.53 | 68.5 | 155 | 0.04 | 2.01 | 0.34 | 0.09 | 0.11 | 5.85 | 0.66 | 14.1 | 1.63 | 0.82 | 0.51 |
| AJ122219 (-63µm) | 183 | 229 | 0.517 | 68.7 | 159 | 0.04 | 1.87 | 0.41 | 0.09 | 0.1 | 5.91 | 0.69 | 14.4 | 1.69 | 0.86 | 0.54 |
| AJ122419 (-63µm) | <10 | 217 | 0.391 | 45.6 | 121 | 0.02 | 1.63 | 0.17 | 0.06 | 0.08 | 3.4 | 0.49 | 9.92 | 1.26 | 0.63 | 0.41 |
| AJ122519 (-63µm) | 214 | 229 | 0.522 | 65.8 | 152 | 0.04 | 1.95 | 0.38 | 0.08 | 0.12 | 5.68 | 0.7 | 13.9 | 1.68 | 0.84 | 0.54 |
| AJ122919 (-63µm) | <10 | 198 | 0.371 | 43.9 | 108 | 0.02 | 1.74 | 0.25 | 0.05 | 0.07 | 3.32 | 0.52 | 9.62 | 1.34 | 0.65 | 0.43 |
| AJ123019 (-63µm) | <10 | 214 | 0.505 | 62.2 | 121 | 0.02 | 2.14 | 0.44 | 0.1 | 0.07 | 5.27 | 1.01 | 12.5 | 1.74 | 0.84 | 0.6 |
| AJ123119 (-63µm) | <10 | 202 | 0.38 | 44.3 | 111 | 0.02 | 1.57 | 0.22 | 0.06 | 0.08 | 3.1 | 0.51 | 9.3 | 1.36 | 0.67 | 0.43 |
| AJ123319 (-63µm) | 221 | 225 | 0.414 | 46.2 | 120 | 0.03 | 1.52 | 0.27 | 0.06 | 0.07 | 3.38 | 0.52 | 9.04 | 1.32 | 0.64 | 0.43 |
| AJ123419 (-63µm) | <10 | 222 | 0.416 | 46.2 | 114 | 0.02 | 1.48 | 0.2 | 0.06 | 0.07 | 3.19 | 0.58 | 9.96 | 1.35 | 0.66 | 0.46 |
| AJ123519 (-63µm) | 210 | 248 | 0.44 | 59.9 | 140 | 0.03 | 1.58 | 0.3 | 0.07 | 0.08 | 4.82 | 0.75 | 14.1 | 1.47 | 0.74 | 0.5 |
| AJ123619 (-63µm) | 27 | 224 | 0.491 | 60.6 | 125 | 0.02 | 1.98 | 0.32 | 0.09 | 0.07 | 4.62 | 0.95 | 11.4 | 1.65 | 0.77 | 0.54 |
| AJ123619 (-63µm) R | 24 | 228 | 0.502 | 61 | 127 | 0.02 | 1.9 | 0.34 | 0.09 | 0.07 | 4.61 | 0.96 | 11.2 | 1.59 | 0.79 | 0.54 |

| | Ga ICP MS Partial Digestion | Gd ICP MS Partial Digestion | Ge ICP MS Partial Digestion | Hf ICP MS Partial Digestion | Hg ICP MS Partial Digestion | Ho ICP MS Partial Digestion | Mo ICP MS Partial Digestion | Nb ICP MS Partial Digestion | Nd ICP MS Partial Digestion | Ni ICP MS Partial Digestion | Pb204 ICP MS Partial Digestion | Pb206 ICP MS Partial Digestion | Pb207 ICP MS Partial Digestion | Pb208 ICP MS Partial Digestion | PbSUM ICP MS Partial Digestion | Pr ICP MS Partial Digestion |
|---|---|---|---|---|---|---|---|---|---|---|---|---|---|---|---|---|
| | ppm | ppm | ppm | ppm | ppm | ppm | ppm | ppm | ppm | ppm | ppm | ppm | ppm | ppm | ppm | ppm |
| Description | | | | | | | | | | | | | | | | |
| DCB01/BR2 | 2.08 | 2.33 | <0.01 | 0.72 | 0.1 | 0.29 | 10.5 | 0.09 | 15.7 | 52.2 | 1.2 | 29.4 | 18.3 | 41.6 | 91.5 | 4.27 |
| AJ115419 (-63µm) | 3.12 | 2.55 | <0.01 | 0.39 | 0.03 | 0.28 | 0.25 | 0.06 | 17.2 | 22.5 | 0.107 | 2.09 | 1.64 | 4.09 | 7.93 | 4.78 |
| AJ115519 (-63µm) | 2.62 | 2.46 | <0.01 | 0.34 | 0.02 | 0.28 | 0.23 | 0.06 | 16.2 | 19.6 | 0.085 | 1.78 | 1.32 | 3.32 | 6.51 | 4.5 |
| AJ115819 (-63µm) | 1.82 | 1.87 | <0.01 | 0.27 | 0.02 | 0.22 | 0.15 | 0.07 | 12.2 | 13.5 | 0.059 | 1.49 | 0.934 | 2.34 | 4.82 | 3.39 |
| AJ116019 (-63µm) | 1.38 | 1.85 | <0.01 | 0.41 | 0.03 | 0.23 | 0.19 | 0.07 | 11.6 | 11.2 | 0.052 | 1.05 | 0.786 | 1.96 | 3.85 | 3.13 |
| AJ116319 (-63µm) | 1.95 | 1.96 | <0.01 | 0.28 | 0.02 | 0.22 | 0.14 | 0.06 | 12.7 | 14.4 | 0.063 | 1.24 | 0.935 | 2.4 | 4.64 | 3.51 |
| AJ116719 (-63µm) | 3.84 | 2.75 | <0.01 | 0.41 | 0.02 | 0.3 | 0.24 | 0.07 | 18.9 | 22.8 | 0.094 | 1.91 | 1.46 | 3.73 | 7.19 | 5.32 |
| AJ117619 (-63µm) | 2.36 | 2.27 | <0.01 | 0.2 | 0.04 | 0.26 | 0.12 | 0.18 | 14.7 | 16.8 | 0.073 | 1.4 | 1.12 | 2.81 | 5.41 | 4.09 |
| AJ118419 (-63µm) | 1.45 | 1.89 | <0.01 | 0.4 | 0.02 | 0.23 | 0.2 | 0.07 | 12 | 11.4 | 0.055 | 1.09 | 0.861 | 2.17 | 4.17 | 3.28 |
| AJ118519 (-63µm) | 1.67 | 1.94 | <0.01 | 0.28 | 0.02 | 0.22 | 0.22 | 0.1 | 12.4 | 13.4 | 0.063 | 1.7 | 1.02 | 2.48 | 5.26 | 3.4 |
| AJ118619 (-63µm) | 1.59 | 1.95 | <0.01 | 0.37 | 0.02 | 0.23 | 0.2 | 0.1 | 12.3 | 12.4 | 0.057 | 1.35 | 0.884 | 2.2 | 4.49 | 3.35 |
| AJ118819 (-63µm) | 1.57 | 1.73 | <0.01 | 0.22 | 0.02 | 0.2 | 0.15 | 0.1 | 11.4 | 12.9 | 0.051 | 1.16 | 0.788 | 2.01 | 4 | 3.17 |
| AJ119019 (-63µm) | 1.86 | 2.12 | <0.01 | 0.28 | 0.02 | 0.23 | 0.14 | 0.07 | 13.8 | 13.4 | 0.061 | 1.24 | 0.933 | 2.38 | 4.61 | 3.86 |
| AJ119119 (-63µm) | 2.88 | 2.67 | <0.01 | 0.36 | 0.02 | 0.29 | 0.17 | 0.07 | 18.8 | 18.5 | 0.097 | 1.84 | 1.44 | 3.68 | 7.07 | 5.25 |
| AJ119219 (-63µm) | 1.68 | 1.97 | <0.01 | 0.27 | 0.02 | 0.23 | 0.15 | 0.1 | 13.2 | 13.2 | 0.061 | 1.31 | 0.956 | 2.4 | 4.73 | 3.63 |
| AJ119319 (-63µm) | 1.72 | 2.06 | <0.01 | 0.31 | 0.02 | 0.24 | 0.14 | 0.07 | 13.8 | 12.4 | 0.064 | 1.34 | 0.977 | 2.46 | 4.84 | 3.82 |
| AJ119619 (-63µm) | 1.75 | 2.08 | <0.01 | 0.29 | 0.02 | 0.24 | 0.18 | 0.1 | 13.9 | 13 | 0.065 | 1.32 | 0.974 | 2.48 | 4.84 | 3.81 |
| AJ119719 (-63µm) | 2.78 | 2.67 | <0.01 | 0.35 | 0.01 | 0.28 | 0.17 | 0.07 | 18.2 | 17.2 | 0.086 | 1.68 | 1.3 | 3.3 | 6.37 | 5.12 |
| AJ119819 (-63µm) | 2.54 | 2.65 | <0.01 | 0.29 | 0.02 | 0.29 | 0.12 | 0.12 | 18.1 | 16.6 | 0.078 | 1.54 | 1.2 | 3.07 | 5.89 | 5.09 |
| AJ119919 (-63µm) | 1.77 | 2.2 | <0.01 | 0.29 | 0.02 | 0.24 | 0.15 | 0.07 | 14.6 | 12.7 | 0.061 | 1.2 | 0.92 | 2.34 | 4.52 | 4.09 |
| DCB01/BR2 | 2.07 | 2.36 | <0.01 | 0.71 | 0.1 | 0.29 | 11.1 | 0.1 | 16.2 | 53.2 | 1.19 | 29.5 | 18.2 | 42.3 | 91.2 | 4.37 |
| AJ120019 (-63µm) | 1.82 | 1.96 | <0.01 | 0.47 | 0.04 | 0.22 | 0.28 | 0.06 | 13.4 | 15.3 | 0.087 | 1.71 | 1.34 | 3.33 | 6.46 | 3.72 |
| AJ120219 (-63µm) | 2.7 | 2.7 | <0.01 | 0.35 | 0.02 | 0.29 | 0.2 | 0.19 | 18.4 | 19 | 0.085 | 1.63 | 1.28 | 3.27 | 6.27 | 5.16 |
| AJ120319 (-63µm) | 1.38 | 1.89 | <0.01 | 0.23 | 0.02 | 0.22 | 0.18 | 0.08 | 12.4 | 11.2 | 0.048 | 0.964 | 0.727 | 1.86 | 3.6 | 3.46 |
| AJ120419 (-63µm) | 1.64 | 1.98 | <0.01 | 0.3 | 0.02 | 0.24 | 0.16 | 0.16 | 12.8 | 12.9 | 0.062 | 1.27 | 0.968 | 2.48 | 4.77 | 3.54 |
| AJ120619 (-63µm) | 1.69 | 1.92 | <0.01 | 0.27 | 0.02 | 0.22 | 0.15 | 0.08 | 12.9 | 12.3 | 0.054 | 1.05 | 0.811 | 2.07 | 3.99 | 3.6 |
| AJ120719 (-63µm) | 1.44 | 1.84 | <0.01 | 0.26 | 0.03 | 0.22 | 0.06 | 0.04 | 12.2 | 9.77 | 0.051 | 1.09 | 0.82 | 2.04 | 4 | 3.37 |
| AJ120819 (-63µm) | 1.62 | 2.23 | <0.01 | 0.21 | 0.03 | 0.26 | 0.07 | 0.06 | 15.1 | 10.5 | 0.068 | 1.38 | 1.03 | 2.57 | 5.05 | 4.18 |
| AJ120919 (-63µm) | 2.66 | 2.55 | <0.01 | 0.47 | 0.03 | 0.3 | 0.19 | 0.15 | 17.1 | 18 | 0.082 | 1.61 | 1.27 | 3.21 | 6.17 | 4.76 |
| AJ121019 (-63µm) | 2.32 | 2.27 | <0.01 | 0.31 | 0.02 | 0.26 | 0.12 | 0.09 | 15.4 | 14.9 | 0.064 | 1.3 | 0.995 | 2.54 | 4.9 | 4.26 |
| AJ121119 (-63µm) | 2.26 | 2.15 | <0.01 | 0.3 | 0.02 | 0.24 | 0.19 | 0.12 | 14.9 | 15 | 0.063 | 1.28 | 0.976 | 2.5 | 4.81 | 4.16 |
| AJ121219 (-63µm) | 3.2 | 2.84 | <0.01 | 0.37 | 0.02 | 0.3 | 0.22 | 0.07 | 19.7 | 21.2 | 0.093 | 1.86 | 1.44 | 3.66 | 7.05 | 5.55 |
| AJ121319 (-63µm) | 1.76 | 2.18 | <0.01 | 0.42 | 0.02 | 0.26 | 0.19 | 0.08 | 14.2 | 12.8 | 0.064 | 1.25 | 0.978 | 2.44 | 4.74 | 3.94 |
| AJ121419 (-63µm) | 4.1 | 3.12 | <0.01 | 0.44 | 0.02 | 0.34 | 0.2 | 0.29 | 21.9 | 23.3 | 0.096 | 1.96 | 1.48 | 3.8 | 7.34 | 6.26 |
| AJ121519 (-63µm) | 1.46 | 1.88 | <0.01 | 0.23 | 0.02 | 0.22 | 0.14 | 0.12 | 12.3 | 10.9 | 0.054 | 1.1 | 0.842 | 2.16 | 4.16 | 3.4 |
| AJ121619 (-63µm) | 1.71 | 2.08 | <0.01 | 0.27 | 0.03 | 0.24 | 0.16 | 0.09 | 14.1 | 12.6 | 0.066 | 1.3 | 0.989 | 2.55 | 4.9 | 3.89 |
| AJ121719 (-63µm) | 2.7 | 2.78 | <0.01 | 0.36 | 0.02 | 0.29 | 0.19 | 0.16 | 19.3 | 18 | 0.084 | 1.64 | 1.28 | 3.31 | 6.32 | 5.39 |
| AJ121819 (-63µm) | 3.38 | 2.88 | <0.01 | 0.33 | 0.02 | 0.31 | 0.15 | 0.07 | 20.5 | 20.4 | 0.097 | 1.93 | 1.51 | 3.85 | 7.38 | 5.83 |
| AJ121919 (-63µm) | 2.44 | 2.54 | <0.01 | 0.31 | <0.01 | 0.27 | 0.18 | 0.07 | 17.5 | 15.4 | 0.073 | 1.41 | 1.1 | 2.85 | 5.44 | 4.93 |
| AJ121819 (-63µm) R | 3.38 | 3.04 | <0.01 | 0.35 | <0.01 | 0.32 | 0.16 | 0.08 | 21.6 | 21.2 | 0.094 | 1.96 | 1.5 | 3.88 | 7.44 | 5.9 |
| DCB01/BR2 | 2.02 | 2.32 | <0.01 | 0.71 | 0.09 | 0.29 | 11 | 0.1 | 15.9 | 51.3 | 1.18 | 29.2 | 18.5 | 42 | 90.9 | 4.3 |
| AJ122019 (-63µm) | 2.67 | 2.55 | <0.01 | 0.47 | 0.03 | 0.29 | 0.24 | 0.14 | 17.1 | 18.8 | 0.085 | 1.74 | 1.31 | 3.31 | 6.45 | 4.76 |
| AJ122119 (-63µm) | 2.62 | 2.48 | <0.01 | 0.44 | 0.02 | 0.29 | 0.2 | 0.14 | 16.7 | 17.9 | 0.082 | 1.67 | 1.25 | 3.18 | 6.19 | 4.67 |
| AJ122219 (-63µm) | 2.64 | 2.55 | <0.01 | 0.47 | 0.02 | 0.3 | 0.18 | 0.14 | 17.4 | 17.9 | 0.085 | 1.68 | 1.28 | 3.28 | 6.32 | 4.83 |
| AJ122419 (-63µm) | 1.64 | 1.9 | <0.01 | 0.26 | 0.02 | 0.21 | 0.14 | 0.07 | 12.8 | 12.3 | 0.055 | 1.1 | 0.85 | 2.18 | 4.19 | 3.58 |
| AJ122519 (-63µm) | 2.56 | 2.54 | <0.01 | 0.48 | 0.02 | 0.29 | 0.18 | 0.15 | 17.1 | 17.8 | 0.081 | 1.62 | 1.25 | 3.15 | 6.1 | 4.74 |
| AJ122919 (-63µm) | 1.68 | 2 | <0.01 | 0.27 | 0.03 | 0.23 | 0.13 | 0.06 | 13.8 | 12.2 | 0.058 | 1.27 | 0.903 | 2.24 | 4.47 | 3.79 |
| AJ123019 (-63µm) | 2.82 | 2.79 | <0.01 | 0.38 | 0.02 | 0.3 | 0.2 | 0.09 | 19.7 | 18.2 | 0.088 | 1.7 | 1.34 | 3.41 | 6.54 | 5.53 |
| AJ123119 (-63µm) | 1.6 | 2 | <0.01 | 0.27 | 0.02 | 0.23 | 0.15 | 0.08 | 13.8 | 11.4 | 0.057 | 1.13 | 0.878 | 2.25 | 4.32 | 3.82 |
| AJ123319 (-63µm) | 1.57 | 1.98 | <0.01 | 0.26 | 0.02 | 0.23 | 0.16 | 0.1 | 13.6 | 12.1 | 0.057 | 1.12 | 0.866 | 2.19 | 4.24 | 3.77 |
| AJ123419 (-63µm) | 1.65 | 2.1 | <0.01 | 0.28 | 0.01 | 0.24 | 0.15 | 0.08 | 14.5 | 11.4 | 0.058 | 1.17 | 0.892 | 2.26 | 4.38 | 4.05 |
| AJ123519 (-63µm) | 2.37 | 2.29 | <0.01 | 0.33 | 0.02 | 0.26 | 0.16 | 0.1 | 16.1 | 15.4 | 0.067 | 1.37 | 1.04 | 2.66 | 5.13 | 4.49 |
| AJ123619 (-63µm) | 2.7 | 2.55 | <0.01 | 0.31 | 0.02 | 0.27 | 0.17 | 0.06 | 18 | 16.5 | 0.074 | 1.49 | 1.14 | 2.89 | 5.59 | 5.11 |
| AJ123619 (-63µm) R | 2.68 | 2.54 | <0.01 | 0.32 | 0.02 | 0.27 | 0.17 | 0.07 | 18 | 16.4 | 0.074 | 1.48 | 1.15 | 2.93 | 5.64 | 5.1 |

| | Rb ICP MS Partial Digestion | Sb ICP MS Partial Digestion | Sc ICP MS Partial Digestion | Se ICP MS Partial Digestion | Sm ICP MS Partial Digestion | Sn ICP MS Partial Digestion | Ta ICP MS Partial Digestion | Tb ICP MS Partial Digestion | Te ICP MS Partial Digestion | Th ICP MS Partial Digestion | U ICP MS Partial Digestion | V ICP MS Partial Digestion | W ICP MS Partial Digestion | Y ICP MS Partial Digestion | Yb ICP MS Partial Digestion | Zn ICP MS Partial Digestion |
|---|---|---|---|---|---|---|---|---|---|---|---|---|---|---|---|---|
| | ppm | ppm | ppm | ppm | ppm | ppm | ppm | ppm | ppm | ppm | ppm | ppm | ppm | ppm | ppm | ppm |
| Description | | | | | | | | | | | | | | | | |
| DCB01/BR2 | 9.96 | 0.31 | 2 | 0.6 | 2.73 | 1.04 | <0.01 | 0.28 | 0.13 | 13.8 | 112 | 28.3 | 4.8 | 6.77 | 0.56 | 120 |
| AJ115419 (-63µm) | 20.1 | 0.05 | 3.2 | <0.1 | 2.77 | 0.63 | <0.01 | 0.28 | 0.01 | 7.77 | 0.72 | 26.7 | 0.6 | 7.18 | 0.6 | 37.8 |
| AJ115519 (-63µm) | 17.1 | 0.04 | 2.7 | 0.2 | 2.72 | 0.37 | <0.01 | 0.28 | <0.01 | 6.62 | 1.76 | 21.3 | 0.4 | 6.87 | 0.59 | 31.3 |
| AJ115819 (-63µm) | 9 | 0.03 | 1.9 | 0.3 | 2.04 | 0.28 | <0.01 | 0.21 | 0.01 | 4.11 | 1.06 | 15.3 | 0.3 | 5.44 | 0.48 | 22.1 |
| AJ116019 (-63µm) | 5.7 | 0.04 | 1.7 | <0.1 | 1.99 | 0.18 | <0.01 | 0.22 | <0.01 | 3.3 | 0.69 | 13.3 | 0.2 | 5.82 | 0.53 | 19.4 |
| AJ116319 (-63µm) | 8 | 0.04 | 2.1 | 0.3 | 2.12 | 0.24 | <0.01 | 0.22 | 0.01 | 4.2 | 0.42 | 17.3 | 0.2 | 5.68 | 0.5 | 22.8 |
| AJ116719 (-63µm) | 21.2 | 0.04 | 3.5 | 0.3 | 3.04 | 0.37 | <0.01 | 0.3 | 0.01 | 7.9 | 0.92 | 29.6 | 0.2 | 7.59 | 0.68 | 43 |
| AJ117619 (-63µm) | 11.1 | 0.03 | 2.3 | 0.4 | 2.45 | 0.36 | <0.01 | 0.26 | 0.01 | 5.03 | 0.4 | 18.4 | 0.2 | 6.72 | 0.6 | 23.2 |
| AJ118419 (-63µm) | 6.04 | 0.04 | 1.7 | 0.2 | 2.06 | 0.18 | <0.01 | 0.22 | 0.01 | 3.4 | 0.5 | 13.8 | 0.2 | 5.97 | 0.53 | 19.9 |
| AJ118519 (-63µm) | 7.15 | 0.04 | 1.7 | 0.2 | 2.1 | 0.21 | <0.01 | 0.22 | 0.01 | 3.81 | 0.61 | 14.4 | 0.2 | 5.71 | 0.51 | 20.6 |
| AJ118619 (-63µm) | 7.21 | 0.04 | 1.6 | 0.4 | 2.05 | 0.2 | <0.01 | 0.21 | 0.01 | 3.66 | 0.87 | 13.8 | 0.2 | 5.69 | 0.51 | 20.7 |
| AJ118819 (-63µm) | 6.59 | 0.03 | 1.5 | <0.1 | 1.92 | 0.19 | <0.01 | 0.2 | <0.01 | 3.21 | 0.56 | 13.8 | 0.2 | 5.14 | 0.46 | 18.4 |
| AJ119019 (-63µm) | 10.2 | 0.04 | 1.9 | 0.3 | 2.28 | 0.23 | <0.01 | 0.24 | 0.01 | 4.53 | 0.6 | 14.8 | 0.2 | 5.74 | 0.49 | 22.3 |
| AJ119119 (-63µm) | 18.5 | 0.03 | 2.7 | 0.4 | 3.09 | 0.36 | <0.01 | 0.3 | 0.02 | 7.1 | 0.82 | 20.8 | 0.2 | 7.05 | 0.61 | 33.1 |
| AJ119219 (-63µm) | 8.06 | 0.03 | 1.7 | 0.3 | 2.19 | 0.21 | <0.01 | 0.22 | <0.01 | 3.74 | 0.55 | 14.2 | 0.2 | 5.54 | 0.51 | 20.8 |
| AJ119319 (-63µm) | 8.01 | 0.04 | 1.8 | 0.3 | 2.31 | 0.2 | <0.01 | 0.23 | <0.01 | 3.92 | 0.46 | 14.6 | 0.2 | 5.9 | 0.53 | 20.7 |
| AJ119619 (-63µm) | 8.18 | 0.04 | 1.7 | 0.1 | 2.32 | 0.21 | <0.01 | 0.23 | 0.01 | 4.05 | 0.69 | 14.2 | 0.1 | 5.88 | 0.54 | 21 |
| AJ119719 (-63µm) | 17.5 | 0.04 | 2.4 | 0.3 | 2.98 | 0.32 | <0.01 | 0.3 | 0.01 | 6.75 | 0.46 | 19.8 | 0.2 | 6.82 | 0.61 | 30.8 |
| AJ119819 (-63µm) | 13.4 | 0.02 | 2.2 | 0.4 | 2.95 | 0.28 | <0.01 | 0.3 | 0.01 | 6.18 | 0.44 | 18.3 | 0.2 | 6.72 | 0.6 | 25.2 |
| AJ119919 (-63µm) | 9.84 | 0.03 | 1.8 | 0.3 | 2.43 | 0.23 | <0.01 | 0.25 | <0.01 | 4.56 | 0.39 | 14.6 | 0.1 | 5.72 | 0.51 | 21 |
| DCB01/BR2 | 10.2 | 0.3 | 1.9 | 0.6 | 2.75 | 1.07 | <0.01 | 0.29 | 0.12 | 14.2 | 114 | 29 | 4.6 | 6.85 | 0.59 | 121 |
| AJ120019 (-63µm) | 9.09 | 0.06 | 2.1 | 0.3 | 2.17 | 0.24 | <0.01 | 0.22 | 0.01 | 4.53 | 0.54 | 16.2 | 0.4 | 5.54 | 0.53 | 31.8 |
| AJ120219 (-63µm) | 18 | 0.04 | 2.7 | 0.3 | 3.03 | 0.32 | <0.01 | 0.3 | 0.01 | 7.02 | 0.46 | 20.5 | 0.3 | 7.18 | 0.62 | 31 |
| AJ120319 (-63µm) | 7.3 | 0.03 | 1.6 | 0.3 | 2.11 | 0.17 | <0.01 | 0.22 | 0.01 | 3.67 | 0.58 | 12.3 | 0.2 | 5.17 | 0.47 | 17.4 |
| AJ120419 (-63µm) | 7.37 | 0.04 | 1.8 | 0.2 | 2.19 | 0.2 | <0.01 | 0.22 | 0.01 | 3.8 | 0.56 | 15.4 | 0.2 | 5.88 | 0.52 | 20.5 |
| AJ120619 (-63µm) | 8.16 | 0.04 | 1.7 | 0.3 | 2.14 | 0.18 | <0.01 | 0.22 | <0.01 | 3.98 | 0.36 | 14.3 | 0.2 | 5.63 | 0.49 | 19.2 |
| AJ120719 (-63µm) | 7 | <0.01 | 1.5 | 0.4 | 2.09 | 0.07 | <0.01 | 0.21 | <0.01 | 3.45 | 0.52 | 10.2 | 0.2 | 5.25 | 0.48 | 17.9 |
| AJ120819 (-63µm) | 7.45 | <0.01 | 1.7 | 0.5 | 2.5 | 0.07 | <0.01 | 0.25 | 0.01 | 3.76 | 0.5 | 11.1 | 0.4 | 6.53 | 0.59 | 19.6 |
| AJ120919 (-63µm) | 12.8 | 0.04 | 2.5 | 0.2 | 2.83 | 0.26 | <0.01 | 0.29 | 0.01 | 5.97 | 0.78 | 20.2 | 0.3 | 7.63 | 0.68 | 32.3 |
| AJ121019 (-63µm) | 11.2 | 0.03 | 2.1 | 0.2 | 2.54 | 0.27 | <0.01 | 0.26 | <0.01 | 4.91 | 0.5 | 17.1 | 0.2 | 6.59 | 0.58 | 26.9 |
| AJ121119 (-63µm) | 12.1 | 0.03 | 2 | <0.1 | 2.46 | 0.22 | <0.01 | 0.24 | <0.01 | 4.99 | 0.6 | 18.6 | 0.2 | 6.1 | 0.56 | 25.1 |
| AJ121219 (-63µm) | 19.1 | 0.04 | 2.8 | 0.3 | 3.2 | 0.35 | <0.01 | 0.31 | 0.02 | 7.43 | 0.81 | 22.7 | 0.2 | 7.51 | 0.65 | 33.4 |
| AJ121319 (-63µm) | 8.32 | 0.04 | 1.8 | 0.4 | 2.4 | 0.2 | <0.01 | 0.25 | 0.01 | 4.22 | 0.87 | 15 | 0.2 | 6.63 | 0.59 | 23 |
| AJ121419 (-63µm) | 21.8 | 0.04 | 3.5 | 0.3 | 3.49 | 0.39 | <0.01 | 0.34 | 0.01 | 8.84 | 0.46 | 29.5 | 0.2 | 8.44 | 0.76 | 40.9 |
| AJ121519 (-63µm) | 6.7 | 0.03 | 1.5 | 0.2 | 2.08 | 0.17 | <0.01 | 0.21 | 0.01 | 3.41 | 0.57 | 12.4 | 0.1 | 5.49 | 0.49 | 16.8 |
| AJ121619 (-63µm) | 8.16 | 0.04 | 1.7 | 0.3 | 2.37 | 0.21 | <0.01 | 0.24 | 0.01 | 4.06 | 0.54 | 14 | 0.2 | 5.88 | 0.52 | 19.9 |
| AJ121719 (-63µm) | 18.9 | 0.04 | 2.5 | 0.4 | 3.16 | 0.32 | <0.01 | 0.3 | 0.02 | 7.08 | 0.46 | 18.8 | 0.2 | 7.16 | 0.63 | 30.3 |
| AJ121819 (-63µm) | 18.9 | 0.03 | 2.8 | 0.4 | 3.32 | 0.37 | <0.01 | 0.31 | 0.02 | 8.11 | 0.54 | 23 | 0.2 | 7.36 | 0.66 | 32.3 |
| AJ121919 (-63µm) | 15.2 | 0.04 | 2.2 | 0.2 | 2.9 | 0.29 | <0.01 | 0.28 | 0.02 | 6.13 | 0.51 | 16.7 | 0.2 | 6.49 | 0.56 | 26.2 |
| AJ121819 (-63µm) R | 18.9 | 0.03 | 2.8 | 0.2 | 3.35 | 0.38 | <0.01 | 0.33 | 0.02 | 8.13 | 0.56 | 23.4 | 0.2 | 7.41 | 0.67 | 32.6 |
| DCB01/BR2 | 10 | 0.34 | 1.9 | 0.7 | 2.66 | 1.11 | <0.01 | 0.29 | 0.13 | 14.1 | 113 | 28.4 | 4.7 | 6.96 | 0.59 | 122 |
| AJ122019 (-63µm) | 12.5 | 0.05 | 2.5 | <0.1 | 2.82 | 0.3 | <0.01 | 0.29 | 0.01 | 5.93 | 0.78 | 20.3 | 0.3 | 7.54 | 0.68 | 34.1 |
| AJ122119 (-63µm) | 12.4 | 0.04 | 2.4 | 0.1 | 2.74 | 0.3 | <0.01 | 0.28 | 0.01 | 5.69 | 0.82 | 19.3 | 0.3 | 7.33 | 0.65 | 32.3 |
| AJ122219 (-63µm) | 12.6 | 0.04 | 2.5 | <0.1 | 2.86 | 0.28 | <0.01 | 0.29 | 0.01 | 5.92 | 0.76 | 20.1 | 0.3 | 7.34 | 0.69 | 33.8 |
| AJ122419 (-63µm) | 7.7 | 0.04 | 1.6 | 0.2 | 2.14 | 0.18 | <0.01 | 0.22 | <0.01 | 3.83 | 0.44 | 13.4 | 0.2 | 5.28 | 0.48 | 19.9 |
| AJ122519 (-63µm) | 12.2 | 0.04 | 2.4 | <0.1 | 2.82 | 0.3 | <0.01 | 0.29 | <0.01 | 5.82 | 0.76 | 18.9 | 0.2 | 7.3 | 0.65 | 31.5 |
| AJ122919 (-63µm) | 7.63 | 0.04 | 1.6 | 0.2 | 2.32 | 0.2 | <0.01 | 0.23 | 0.01 | 3.76 | 0.36 | 13.5 | 0.2 | 5.39 | 0.51 | 19.7 |
| AJ123019 (-63µm) | 18.2 | 0.05 | 2.4 | 0.2 | 3.18 | 0.35 | <0.01 | 0.3 | 0.01 | 7.28 | 0.64 | 19.7 | 0.2 | 6.88 | 0.62 | 32.4 |
| AJ123119 (-63µm) | 7.93 | 0.04 | 1.6 | 0.3 | 2.25 | 0.18 | <0.01 | 0.23 | 0.01 | 3.98 | 0.43 | 12.9 | 0.2 | 5.47 | 0.5 | 18.8 |
| AJ123319 (-63µm) | 8.21 | 0.04 | 1.5 | 0.2 | 2.24 | 0.18 | <0.01 | 0.23 | 0.01 | 3.78 | 0.66 | 12.7 | 0.2 | 5.31 | 0.49 | 18.5 |
| AJ123419 (-63µm) | 8.83 | 0.03 | 1.6 | 0.3 | 2.41 | 0.22 | <0.01 | 0.24 | 0.01 | 4.31 | 0.56 | 12.6 | 0.2 | 5.32 | 0.5 | 19.1 |
| AJ123519 (-63µm) | 12.9 | 0.04 | 2 | 0.2 | 2.63 | 0.26 | <0.01 | 0.25 | <0.01 | 5.28 | 0.68 | 18.3 | 0.2 | 6.31 | 0.56 | 27.1 |
| AJ123619 (-63µm) | 16.6 | 0.04 | 2.3 | 0.3 | 2.92 | 0.33 | <0.01 | 0.28 | 0.01 | 6.51 | 0.68 | 19 | 0.3 | 6.57 | 0.58 | 29.6 |
| AJ123619 (-63µm) R | 16.8 | 0.04 | 2.3 | 0.3 | 2.93 | 0.34 | <0.01 | 0.28 | 0.01 | 6.58 | 0.7 | 18.2 | 0.3 | 6.52 | 0.58 | 29.5 |

| | Zr ICP MS Partial Digestion | Ag ICP MS Total Digestion | Be ICP MS Total Digestion | Bi ICP MS Total Digestion | Cd ICP MS Total Digestion | Co ICP MS Total Digestion | Cs ICP MS Total Digestion | Cu ICP MS Total Digestion | Dy ICP MS Total Digestion | Er ICP MS Total Digestion | Eu ICP MS Total Digestion | Ga ICP MS Total Digestion | Gd ICP MS Total Digestion | Hf ICP MS Total Digestion | Ho ICP MS Total Digestion | Mo ICP MS Total Digestion |
|---|---|---|---|---|---|---|---|---|---|---|---|---|---|---|---|---|
| | ppm | ppm | ppm | ppm | ppm | ppm | ppm | ppm | ppm | ppm | ppm | ppm | ppm | ppm | ppm | ppm |
| Description | | | | | | | | | | | | | | | | |
| DCB01/BR2 | 30.9 | 2.68 | 1.9 | 7.8 | 0.8 | 17.9 | 1 | 274 | 4.46 | 2.2 | 1.28 | 14.1 | 5.6 | 11 | 0.77 | 12.1 |
| AJ115419 (-63µm) | 15.3 | 0.21 | 1.5 | 0.6 | 0.3 | 10.8 | 3.1 | 22.1 | 2.74 | 1.46 | 0.96 | 12.1 | 3.2 | 3.4 | 0.48 | 0.49 |
| AJ115519 (-63µm) | 13.5 | 0.18 | 1.4 | 0.4 | 0.3 | 9.33 | 2.8 | 18.6 | 2.72 | 1.49 | 0.94 | 11 | 3 | 3.5 | 0.5 | 0.4 |
| AJ115819 (-63µm) | 10.6 | 0.15 | 0.9 | 0.3 | 0.3 | 6.9 | 1.6 | 16.3 | 2.2 | 1.22 | 0.81 | 8.4 | 2.4 | 3.2 | 0.4 | 0.24 |
| AJ116019 (-63µm) | 19 | 0.15 | 1 | 0.2 | 0.3 | 5.52 | 1 | 14.8 | 2.17 | 1.18 | 0.8 | 7.4 | 2.3 | 3.4 | 0.4 | 0.31 |
| AJ116319 (-63µm) | 11.8 | 0.15 | 1.1 | 0.2 | 0.3 | 7.3 | 1.6 | 17.3 | 2.24 | 1.2 | 0.8 | 8.7 | 2.6 | 3.3 | 0.41 | 0.25 |
| AJ116719 (-63µm) | 17 | 0.22 | 1.3 | 0.3 | 0.3 | 10.7 | 2.9 | 24.7 | 2.71 | 1.47 | 1.01 | 12.7 | 3.2 | 3.3 | 0.49 | 0.4 |
| AJ117619 (-63µm) | 10.4 | 0.18 | 1.2 | 0.2 | 0.3 | 8.69 | 1.9 | 17.7 | 2.5 | 1.33 | 0.89 | 9.3 | 2.8 | 3.1 | 0.43 | 0.26 |
| AJ118419 (-63µm) | 18.5 | 0.16 | 0.9 | 0.2 | 0.3 | 5.55 | 1.1 | 13.9 | 2.21 | 1.14 | 0.8 | 7.7 | 2.5 | 3.1 | 0.41 | 0.33 |
| AJ118519 (-63µm) | 11.7 | 0.16 | 1.2 | 0.2 | 0.3 | 7.05 | 1.3 | 15.5 | 2.29 | 1.24 | 0.81 | 8.4 | 2.4 | 3.2 | 0.41 | 0.38 |
| AJ118619 (-63µm) | 16.5 | 0.16 | 1.2 | 0.2 | 0.3 | 6.77 | 1.2 | 14 | 2.38 | 1.25 | 0.87 | 9.2 | 2.6 | 4.3 | 0.41 | 0.31 |
| AJ118819 (-63µm) | 9.53 | 0.14 | 1 | 0.2 | 0.3 | 6.41 | 1.1 | 14 | 2.15 | 1.19 | 0.84 | 8 | 2.5 | 4 | 0.39 | 0.27 |
| AJ119019 (-63µm) | 10.8 | 0.15 | 1 | 0.2 | 0.3 | 6.24 | 1.7 | 14.8 | 2.22 | 1.19 | 0.81 | 8.5 | 2.6 | 3 | 0.4 | 0.26 |
| AJ119119 (-63µm) | 14 | 0.19 | 1.4 | 0.3 | 0.3 | 9.4 | 3 | 18.9 | 2.75 | 1.5 | 0.99 | 12 | 3.4 | 3.2 | 0.49 | 0.31 |
| AJ119219 (-63µm) | 10.6 | 0.16 | 0.8 | 0.2 | 0.3 | 6.43 | 1.4 | 15.2 | 2.14 | 1.15 | 0.76 | 8 | 2.4 | 3 | 0.4 | 0.27 |
| AJ119319 (-63µm) | 12 | 0.16 | 1.1 | 0.2 | 0.2 | 6.07 | 1.4 | 15.4 | 2.19 | 1.19 | 0.79 | 8 | 2.5 | 2.9 | 0.4 | 0.27 |
| AJ119619 (-63µm) | 11.6 | 0.17 | 1.1 | 0.2 | 0.3 | 7.14 | 1.4 | 15.5 | 2.3 | 1.21 | 0.84 | 8.5 | 2.6 | 3 | 0.4 | 0.31 |
| AJ119719 (-63µm) | 13.6 | 0.19 | 1.3 | 0.3 | 0.3 | 9.24 | 2.9 | 17.8 | 2.73 | 1.46 | 0.97 | 11 | 3.3 | 3.2 | 0.48 | 0.32 |
| AJ119819 (-63µm) | 12.2 | 0.19 | 1.1 | 0.2 | 0.3 | 9.14 | 2.5 | 19 | 2.66 | 1.41 | 0.97 | 10.4 | 3.1 | 3.1 | 0.53 | 0.34 |
| AJ119919 (-63µm) | 10.7 | 0.16 | 1.1 | 0.2 | 0.3 | 6.68 | 1.8 | 15.4 | 2.26 | 1.25 | 0.83 | 8.8 | 2.6 | 3 | 0.4 | 0.26 |
| DCB01/BR2 | 30.2 | 2.73 | 1.6 | 7.7 | 0.9 | 16.8 | 1.1 | 275 | 4.51 | 2.2 | 1.32 | 14.4 | 5.8 | 10.4 | 0.74 | 12.3 |
| AJ120019 (-63µm) | 20.8 | 0.17 | 1.1 | 0.3 | 0.3 | 11.9 | 1.5 | 28.5 | 2.28 | 1.24 | 0.84 | 9 | 2.7 | 3.8 | 0.42 | 0.4 |
| AJ120219 (-63µm) | 14.4 | 0.21 | 1.4 | 0.3 | 0.3 | 9.72 | 3 | 18.4 | 2.8 | 1.46 | 1 | 11.3 | 3.3 | 3.1 | 0.51 | 0.36 |
| AJ120319 (-63µm) | 8.34 | 0.14 | 0.9 | 0.2 | 0.3 | 5.6 | 1.2 | 12 | 2.13 | 1.17 | 0.8 | 7.2 | 2.5 | 3.1 | 0.39 | 0.28 |
| AJ120419 (-63µm) | 12.4 | 0.16 | 1 | 0.2 | 0.3 | 6.8 | 1.4 | 14.9 | 2.24 | 1.18 | 0.82 | 8 | 2.5 | 3.1 | 0.4 | 0.29 |
| AJ120619 (-63µm) | 11 | 0.15 | 1 | 0.2 | 0.3 | 6.07 | 1.4 | 14.3 | 2.14 | 1.14 | 0.8 | 8 | 2.5 | 2.7 | 0.38 | 0.26 |
| AJ120719 (-63µm) | 9.83 | 0.17 | 1.1 | 0.2 | 0.3 | 5.93 | 1.3 | 14.7 | 2.18 | 1.14 | 0.82 | 8.4 | 2.5 | 3.1 | 0.39 | 0.24 |
| AJ120819 (-63µm) | 9.53 | 0.17 | 1 | 0.2 | 0.3 | 6.01 | 1.3 | 16.8 | 2.25 | 1.21 | 0.85 | 8.4 | 2.6 | 2.7 | 0.39 | 0.24 |
| AJ120919 (-63µm) | 20.8 | 0.22 | 1.3 | 0.2 | 0.4 | 9.99 | 2 | 20.2 | 2.72 | 1.44 | 1.01 | 11.8 | 3.2 | 3.9 | 0.5 | 0.34 |
| AJ121019 (-63µm) | 13.1 | 0.18 | 1.3 | 0.2 | 0.3 | 8.13 | 1.8 | 19.5 | 2.43 | 1.3 | 0.94 | 10.5 | 2.9 | 3.5 | 0.44 | 0.24 |
| AJ121119 (-63µm) | 13.4 | 0.17 | 1.2 | 0.2 | 0.3 | 8.49 | 1.8 | 19 | 2.38 | 1.25 | 0.95 | 10.7 | 2.9 | 3.6 | 0.42 | 0.29 |
| AJ121219 (-63µm) | 15.2 | 0.2 | 1.4 | 0.3 | 0.3 | 10.8 | 3.2 | 21.4 | 2.74 | 1.45 | 0.99 | 12.4 | 3.4 | 3.2 | 0.49 | 0.4 |
| AJ121319 (-63µm) | 18.2 | 0.17 | 1 | 0.2 | 0.3 | 6.91 | 1.5 | 15.7 | 2.36 | 1.27 | 0.89 | 8.6 | 2.7 | 3.3 | 0.42 | 0.33 |
| AJ121419 (-63µm) | 19 | 0.21 | 1.5 | 0.2 | 0.3 | 11.1 | 2.8 | 23.8 | 2.83 | 1.47 | 1.06 | 12.8 | 3.4 | 3.4 | 0.51 | 0.33 |
| AJ121519 (-63µm) | 10.1 | 0.16 | 1 | 0.2 | 0.3 | 5.84 | 1.2 | 12.6 | 2.1 | 1.12 | 0.79 | 7.7 | 2.3 | 3 | 0.38 | 0.3 |
| AJ121619 (-63µm) | 11.2 | 0.17 | 1 | 0.2 | 0.3 | 6.65 | 1.5 | 15.9 | 2.1 | 1.2 | 0.78 | 8.4 | 2.4 | 2.7 | 0.39 | 0.3 |
| AJ121719 (-63µm) | 14.4 | 0.2 | 1.4 | 0.3 | 0.3 | 9.52 | 3.2 | 18.1 | 2.8 | 1.44 | 1 | 11.4 | 3.2 | 3.1 | 0.49 | 0.38 |
| AJ121819 (-63µm) | 14.5 | 0.2 | 1.7 | 0.3 | 0.3 | 11.3 | 3.4 | 23.4 | 2.84 | 1.52 | 1.07 | 13.1 | 3.5 | 3.2 | 0.51 | 0.35 |
| AJ121919 (-63µm) | 11.7 | 0.19 | 1.2 | 0.2 | 0.3 | 8.16 | 2.6 | 15.6 | 2.8 | 1.43 | 0.94 | 10.3 | 3.2 | 3.3 | 0.48 | 0.34 |
| AJ121819 (-63µm) R | 14.7 | 0.2 | 1.3 | 0.3 | 0.3 | 11 | 3.2 | 23.7 | 2.77 | 1.47 | 1.05 | 12.7 | 3.4 | 3 | 0.5 | 0.31 |
| DCB01/BR2 | 29.6 | 2.87 | 1.6 | 7.8 | 0.9 | 17.3 | 1.1 | 278 | 4.63 | 2.26 | 1.31 | 14.6 | 6 | 10.1 | 0.77 | 12.2 |
| AJ122019 (-63µm) | 21.5 | 0.22 | 1.3 | 0.4 | 0.4 | 10.6 | 2.1 | 22.2 | 2.76 | 1.51 | 1.06 | 12.1 | 3.3 | 3.9 | 0.5 | 0.44 |
| AJ122119 (-63µm) | 20.2 | 0.22 | 1.2 | 0.3 | 0.4 | 10.2 | 2.1 | 21.5 | 2.75 | 1.47 | 1 | 11.8 | 3.2 | 3.9 | 0.5 | 0.34 |
| AJ122219 (-63µm) | 20.6 | 0.21 | 1.3 | 0.3 | 0.4 | 9.9 | 2.1 | 21.1 | 2.73 | 1.5 | 1.04 | 12.1 | 3.3 | 4 | 0.51 | 0.34 |
| AJ122419 (-63µm) | 10.5 | 0.14 | 0.9 | 0.2 | 0.2 | 6.12 | 1.4 | 14.8 | 2.03 | 1.11 | 0.75 | 7.7 | 2.4 | 2.9 | 0.39 | 0.24 |
| AJ122519 (-63µm) | 21.1 | 0.21 | 1.2 | 0.2 | 0.4 | 9.93 | 2 | 20.6 | 2.7 | 1.44 | 1.04 | 11.7 | 3.2 | 3.9 | 0.5 | 0.32 |
| AJ122919 (-63µm) | 11 | 0.15 | 0.9 | 0.2 | 0.3 | 5.97 | 1.4 | 14.8 | 2.06 | 1.12 | 0.75 | 7.8 | 2.3 | 2.7 | 0.37 | 0.22 |
| AJ123019 (-63µm) | 14.1 | 0.2 | 1.2 | 0.2 | 0.3 | 9.3 | 3 | 19.5 | 2.76 | 1.43 | 0.97 | 11.7 | 3.2 | 3.1 | 0.48 | 0.32 |
| AJ123119 (-63µm) | 10.7 | 0.17 | 1 | 0.2 | 0.2 | 5.72 | 1.5 | 14.5 | 2.09 | 1.12 | 0.76 | 7.9 | 2.4 | 2.7 | 0.38 | 0.26 |
| AJ123319 (-63µm) | 9.9 | 0.16 | 1.1 | 0.2 | 0.3 | 6.65 | 1.5 | 14.5 | 2.15 | 1.14 | 0.79 | 8.4 | 2.6 | 3 | 0.39 | 0.28 |
| AJ123419 (-63µm) | 10.4 | 0.16 | 0.8 | 0.2 | 0.3 | 6 | 1.6 | 15.5 | 2.17 | 1.13 | 0.8 | 8.2 | 2.6 | 2.8 | 0.38 | 0.28 |
| AJ123519 (-63µm) | 14.1 | 0.18 | 1.2 | 0.2 | 0.3 | 8.55 | 1.9 | 20.1 | 2.33 | 1.22 | 0.93 | 11 | 2.8 | 3.4 | 0.42 | 0.32 |
| AJ123619 (-63µm) | 12.6 | 0.19 | 1.1 | 0.2 | 0.3 | 8.33 | 2.5 | 19.4 | 2.54 | 1.34 | 0.93 | 11 | 3 | 3 | 0.45 | 0.29 |
| AJ123619 (-63µm) R | 12.7 | 0.19 | 1.2 | 0.2 | 0.3 | 8.37 | 2.6 | 19.2 | 2.59 | 1.39 | 0.95 | 11.2 | 3.1 | 3.2 | 0.46 | 0.31 |

| | Nb ICP MS Total Digestion | Nd ICP MS Total Digestion | Ni ICP MS Total Digestion | Pb204 ICP MS Total Digestion | Pb206 ICP MS Total Digestion | Pb207 ICP MS Total Digestion | Pb208 ICP MS Total Digestion | PbSUM ICP MS Total Digestion | Pr ICP MS Total Digestion | Rb ICP MS Total Digestion | Sc ICP MS Total Digestion | Sm ICP MS Total Digestion | Sn ICP MS Total Digestion | Ta ICP MS Total Digestion | Tb ICP MS Total Digestion | Th ICP MS Total Digestion |
|---|---|---|---|---|---|---|---|---|---|---|---|---|---|---|---|---|
| | ppm | ppm | ppm | ppm | ppm | ppm | ppm | ppm | ppm | ppm | ppm | ppm | ppm | ppm | ppm | ppm |
| Description | | | | | | | | | | | | | | | | |
| DCB01/BR2 | 20.1 | 46.9 | 97.5 | 1.32 | 33.3 | 19.8 | 47.4 | 102 | 13.4 | 60.5 | 7.3 | 7.9 | 3.24 | 1.61 | 0.73 | 52.5 |
| AJ115419 (-63µm) | 8.5 | 24.4 | 34 | 0.21 | 3.87 | 3.07 | 7.66 | 14.8 | 6.9 | 85.5 | 8.6 | 4.4 | 1.6 | 0.62 | 0.42 | 11.2 |
| AJ115519 (-63µm) | 7.7 | 23.6 | 29.2 | 0.191 | 3.56 | 2.68 | 6.63 | 13.1 | 6.6 | 78.5 | 7.7 | 4.2 | 1.29 | 0.49 | 0.44 | 9.92 |
| AJ115819 (-63µm) | 6 | 18.4 | 21.5 | 0.145 | 2.66 | 2.16 | 5.25 | 10.2 | 5 | 54.4 | 6.1 | 3.4 | 0.84 | 0.37 | 0.34 | 6.27 |
| AJ116019 (-63µm) | 5.6 | 17.3 | 17.9 | 0.138 | 2.3 | 1.92 | 4.7 | 9.06 | 4.7 | 46.2 | 5.6 | 3.3 | 0.73 | 0.35 | 0.35 | 5.12 |
| AJ116319 (-63µm) | 6.2 | 19.2 | 22.6 | 0.148 | 2.57 | 2.13 | 5.32 | 10.2 | 5.3 | 53.6 | 6.4 | 3.4 | 0.89 | 0.38 | 0.35 | 7.31 |
| AJ116719 (-63µm) | 7.8 | 25.4 | 34.2 | 0.198 | 3.52 | 2.85 | 7.14 | 13.7 | 7.1 | 82.8 | 8.6 | 4.4 | 1.31 | 0.5 | 0.43 | 10.3 |
| AJ117619 (-63µm) | 6.9 | 21.2 | 26.4 | 0.162 | 2.79 | 2.3 | 5.72 | 11 | 5.9 | 61.3 | 6.9 | 3.8 | 0.95 | 0.45 | 0.39 | 7.71 |
| AJ118419 (-63µm) | 5.7 | 18.6 | 17.8 | 0.142 | 2.4 | 2.02 | 5.04 | 9.61 | 5 | 47.7 | 5.6 | 3.4 | 0.71 | 0.36 | 0.34 | 5.82 |
| AJ118519 (-63µm) | 6.1 | 18.2 | 22.3 | 0.147 | 4.49 | 2.35 | 5.57 | 12.6 | 5 | 51.2 | 5.9 | 3.4 | 0.83 | 0.35 | 0.34 | 5.56 |
| AJ118619 (-63µm) | 6 | 19.8 | 20.9 | 0.154 | 3 | 2.28 | 5.65 | 11.1 | 5.4 | 52.8 | 6.1 | 3.6 | 0.82 | 0.36 | 0.36 | 6.62 |
| AJ118819 (-63µm) | 5.7 | 18.3 | 20.7 | 0.136 | 2.54 | 1.97 | 4.89 | 9.54 | 4.9 | 45 | 5.6 | 3.3 | 0.78 | 0.34 | 0.33 | 5.55 |
| AJ119019 (-63µm) | 6.2 | 19.5 | 21.6 | 0.153 | 2.75 | 2.11 | 5.28 | 10.3 | 5.4 | 56.9 | 6.1 | 3.5 | 0.9 | 0.39 | 0.35 | 7.22 |
| AJ119119 (-63µm) | 7.9 | 25.7 | 29.8 | 0.192 | 3.34 | 2.74 | 6.89 | 13.2 | 7.2 | 81.9 | 8 | 4.6 | 1.29 | 0.5 | 0.45 | 10.7 |
| AJ119219 (-63µm) | 5.7 | 17.8 | 20.7 | 0.142 | 2.47 | 2.01 | 5.07 | 9.7 | 4.8 | 48.8 | 5.6 | 3.2 | 0.8 | 0.34 | 0.33 | 5.6 |
| AJ119319 (-63µm) | 5.7 | 18.5 | 19.9 | 0.143 | 2.58 | 2.02 | 5.16 | 9.9 | 5.2 | 48.9 | 5.7 | 3.3 | 0.81 | 0.34 | 0.34 | 6.45 |
| AJ119619 (-63µm) | 6.4 | 19.3 | 21.4 | 0.149 | 2.6 | 2.15 | 5.32 | 10.2 | 5.4 | 52.8 | 5.8 | 3.6 | 0.9 | 0.37 | 0.36 | 6.3 |
| AJ119719 (-63µm) | 7.8 | 24.8 | 28.5 | 0.184 | 3.18 | 2.55 | 6.42 | 12.3 | 6.9 | 78.5 | 7.4 | 4.4 | 1.31 | 0.51 | 0.43 | 9.59 |
| AJ119819 (-63µm) | 7.5 | 24.4 | 28.3 | 0.198 | 3.27 | 2.66 | 6.69 | 12.8 | 6.8 | 69.5 | 7.1 | 4.2 | 1.14 | 0.48 | 0.43 | 9.21 |
| AJ119919 (-63µm) | 6.4 | 19.9 | 21.7 | 0.147 | 2.55 | 2.09 | 5.17 | 9.96 | 5.5 | 56.8 | 6.1 | 3.6 | 0.93 | 0.37 | 0.36 | 6.81 |
| DCB01/BR2 | 20.4 | 47.2 | 96.6 | 1.32 | 33.3 | 19.7 | 47.5 | 102 | 13.6 | 62.8 | 6.8 | 8 | 3.33 | 1.53 | 0.74 | 50.1 |
| AJ120019 (-63µm) | 6.5 | 20.1 | 25.1 | 0.176 | 3.22 | 2.64 | 6.58 | 12.6 | 5.6 | 55 | 6.7 | 3.5 | 0.89 | 0.4 | 0.36 | 7.06 |
| AJ120219 (-63µm) | 8.1 | 25.1 | 31.3 | 0.179 | 3.1 | 2.53 | 6.45 | 12.3 | 7.1 | 81.4 | 7.8 | 4.5 | 1.28 | 0.53 | 0.44 | 9.93 |
| AJ120319 (-63µm) | 5.9 | 18.3 | 18 | 0.129 | 2.23 | 1.85 | 4.57 | 8.78 | 5 | 47.4 | 4.9 | 3.3 | 0.78 | 0.36 | 0.34 | 5.7 |
| AJ120419 (-63µm) | 6.1 | 18.8 | 20.7 | 0.156 | 2.63 | 2.14 | 5.29 | 10.2 | 5.2 | 50.7 | 5.5 | 3.4 | 0.82 | 0.37 | 0.34 | 5.89 |
| AJ120619 (-63µm) | 5.8 | 18.3 | 20.6 | 0.133 | 2.27 | 1.91 | 4.72 | 9.03 | 5.1 | 49.8 | 5.4 | 3.4 | 0.78 | 0.35 | 0.34 | 5.82 |
| AJ120719 (-63µm) | 6.2 | 18.8 | 18.5 | 0.155 | 2.58 | 2.16 | 5.3 | 10.2 | 5.2 | 50.9 | 5.6 | 3.4 | 0.86 | 0.38 | 0.34 | 5.77 |
| AJ120819 (-63µm) | 5.6 | 20 | 19.5 | 0.159 | 2.74 | 2.26 | 5.55 | 10.7 | 5.6 | 49.8 | 5.4 | 3.5 | 0.78 | 0.34 | 0.36 | 6.34 |
| AJ120919 (-63µm) | 7.6 | 24.4 | 29.2 | 0.182 | 3.16 | 2.62 | 6.58 | 12.5 | 6.7 | 69.5 | 7.7 | 4.4 | 1.09 | 0.46 | 0.43 | 8.3 |
| AJ121019 (-63µm) | 6.9 | 22 | 24.1 | 0.167 | 2.72 | 2.36 | 5.82 | 11.1 | 6.2 | 63.4 | 6.8 | 3.9 | 1.02 | 0.41 | 0.38 | 7.25 |
| AJ121119 (-63µm) | 6.4 | 21.7 | 25.4 | 0.175 | 2.86 | 2.46 | 6.08 | 11.6 | 6 | 66.4 | 6.6 | 3.8 | 0.96 | 0.39 | 0.37 | 7.25 |
| AJ121219 (-63µm) | 8 | 25.9 | 33.4 | 0.19 | 3.23 | 2.65 | 6.78 | 12.8 | 7.2 | 85.7 | 8 | 4.6 | 1.33 | 0.49 | 0.43 | 10.4 |
| AJ121319 (-63µm) | 6.3 | 20.7 | 21.4 | 0.151 | 2.5 | 2.09 | 5.23 | 9.97 | 5.7 | 53.6 | 5.8 | 3.8 | 0.87 | 0.37 | 0.37 | 6.47 |
| AJ121419 (-63µm) | 7.8 | 26.6 | 34 | 0.181 | 3.36 | 2.71 | 6.81 | 13.1 | 7.4 | 86.7 | 8.9 | 4.6 | 1.23 | 0.47 | 0.45 | 10.6 |
| AJ121519 (-63µm) | 5.8 | 17.8 | 18.7 | 0.133 | 2.33 | 1.99 | 4.89 | 9.34 | 4.9 | 46.8 | 5.2 | 3.2 | 0.76 | 0.34 | 0.33 | 5.61 |
| AJ121619 (-63µm) | 6.2 | 18.4 | 21.5 | 0.146 | 2.49 | 2.07 | 5.12 | 9.83 | 5.1 | 54 | 5.9 | 3.3 | 0.86 | 0.35 | 0.33 | 5.88 |
| AJ121719 (-63µm) | 8 | 24.8 | 29.3 | 0.188 | 3.17 | 2.56 | 6.38 | 12.3 | 6.9 | 83.8 | 7.2 | 4.3 | 1.36 | 0.5 | 0.42 | 9.81 |
| AJ121819 (-63µm) | 8.5 | 27 | 34.6 | 0.209 | 3.66 | 3 | 7.5 | 14.4 | 7.7 | 90.2 | 8.3 | 4.8 | 1.46 | 0.51 | 0.46 | 10.7 |
| AJ121919 (-63µm) | 7.8 | 24.9 | 25.6 | 0.171 | 2.86 | 2.41 | 6.04 | 11.5 | 7 | 74.8 | 6.9 | 4.3 | 1.21 | 0.47 | 0.43 | 9.42 |
| AJ121819 (-63µm) R | 8.1 | 27.3 | 33.4 | 0.204 | 3.67 | 3.05 | 7.41 | 14.3 | 7.4 | 91.2 | 8 | 4.7 | 1.36 | 0.51 | 0.45 | 10.5 |
| DCB01/BR2 | 19.8 | 49.1 | 97.6 | 1.31 | 33.3 | 19.7 | 47.8 | 102 | 14.2 | 61.6 | 6.8 | 8 | 3.45 | 1.67 | 0.81 | 51.2 |
| AJ122019 (-63µm) | 8.1 | 24.6 | 30.7 | 0.191 | 3.27 | 2.72 | 6.7 | 12.9 | 7 | 71 | 8 | 4.3 | 1.18 | 0.48 | 0.43 | 8.54 |
| AJ122119 (-63µm) | 7.9 | 24.4 | 29.9 | 0.192 | 3.24 | 2.67 | 6.66 | 12.8 | 6.8 | 70.3 | 7.7 | 4.4 | 1.1 | 0.46 | 0.45 | 8.59 |
| AJ122219 (-63µm) | 8 | 25 | 29.8 | 0.188 | 3.15 | 2.64 | 6.66 | 12.6 | 7 | 71.8 | 8 | 4.4 | 1.12 | 0.47 | 0.43 | 8.85 |
| AJ122419 (-63µm) | 5.6 | 17.8 | 20.5 | 0.129 | 2.22 | 1.84 | 4.59 | 8.78 | 5 | 48.7 | 5.3 | 3.2 | 0.76 | 0.32 | 0.34 | 5.68 |
| AJ122519 (-63µm) | 7.8 | 24.4 | 28.3 | 0.183 | 3.12 | 2.59 | 6.52 | 12.4 | 6.8 | 69.9 | 7.4 | 4.3 | 1.19 | 0.48 | 0.43 | 8.95 |
| AJ122919 (-63µm) | 5.6 | 17.6 | 20.2 | 0.126 | 2.35 | 1.83 | 4.6 | 8.91 | 5 | 48.3 | 5.1 | 3.2 | 1.22 | 0.32 | 0.32 | 5.62 |
| AJ123019 (-63µm) | 7.8 | 24.9 | 30 | 0.178 | 3 | 2.48 | 6.31 | 12 | 6.9 | 81.2 | 7.2 | 4.4 | 1.36 | 0.48 | 0.42 | 9.72 |
| AJ123119 (-63µm) | 5.8 | 18.1 | 20.2 | 0.132 | 2.22 | 1.85 | 4.6 | 8.8 | 4.9 | 49.6 | 5.3 | 3.2 | 0.88 | 0.33 | 0.33 | 5.75 |
| AJ123319 (-63µm) | 6 | 18.7 | 21.8 | 0.131 | 2.35 | 1.94 | 4.87 | 9.29 | 5.1 | 52.5 | 5.4 | 3.4 | 0.8 | 0.37 | 0.34 | 5.98 |
| AJ123419 (-63µm) | 6.3 | 18.8 | 20 | 0.136 | 2.32 | 1.97 | 4.8 | 9.23 | 5.3 | 54 | 5.4 | 3.4 | 0.84 | 0.35 | 0.35 | 6.38 |
| AJ123519 (-63µm) | 6.6 | 21.2 | 25.7 | 0.167 | 2.76 | 2.33 | 5.79 | 11 | 5.9 | 65.3 | 6.6 | 3.8 | 0.96 | 0.4 | 0.37 | 7.16 |
| AJ123619 (-63µm) | 7.5 | 23 | 26.5 | 0.166 | 2.85 | 2.37 | 5.91 | 11.3 | 6.5 | 75.1 | 6.8 | 4 | 1.23 | 0.45 | 0.4 | 9.41 |
| AJ123619 (-63µm) R | 7.6 | 24.1 | 26.7 | 0.174 | 2.88 | 2.4 | 6.11 | 11.6 | 6.7 | 78 | 7.1 | 4.2 | 1.24 | 0.46 | 0.41 | 9.53 |

| | U ICP MS Total Digestion | W ICP MS Total Digestion | Y ICP MS Total Digestion | Yb ICP MS Total Digestion | Zn ICP MS Total Digestion | Ca Calcium Magnesium | Mg Calcium Magnesium | Dol Calcium Magnesium | Cal Calcium Magnesium | CO3 Calcium Magnesium | Dol/Cal Calcium Magnesium | CO2Cal Calcium Magnesium | CO2Dol Calcium Magnesium | CO2Tot Calcium Magnesium |
|---|---|---|---|---|---|---|---|---|---|---|---|---|---|---|
| | ppm | ppm | ppm | ppm | ppm | wt % | wt % | wt% | wt% | wt% | ml | ml | ml | ml |
| Description | | | | | | | | | | | | | | |
| DCB01/BR2 | 126 | 10.4 | 21.4 | 1.95 | 128 | 5.13 | 1.6 | 12.14 | 6.22 | 18.36 | 1.95 | 13.93 | 29.48 | 43.41 |
| AJ115419 (-63µm) | 2.96 | 1.4 | 13.1 | 1.36 | 58 | 12.2 | 2.64 | 20.02 | 19.6 | 39.62 | 1.02 | 43.86 | 48.64 | 92.5 |
| AJ115519 (-63µm) | 4.35 | 1.2 | 13.7 | 1.36 | 51 | 12.8 | 2.93 | 22.22 | 19.9 | 42.13 | 1.12 | 44.54 | 53.98 | 98.53 |
| AJ115819 (-63µm) | 2.38 | 0.8 | 11.3 | 1.1 | 38 | 15.9 | 3.55 | 26.93 | 25.09 | 52.02 | 1.07 | 56.15 | 65.41 | 121.56 |
| AJ116019 (-63µm) | 1.28 | 0.7 | 10.9 | 1.05 | 32 | 14 | 3.81 | 28.9 | 19.28 | 48.18 | 1.5 | 43.14 | 70.2 | 113.34 |
| AJ116319 (-63µm) | 1.43 | 0.8 | 11.7 | 1.14 | 39 | 15.8 | 3.39 | 25.71 | 25.5 | 51.21 | 1.01 | 57.07 | 62.46 | 119.53 |
| AJ116719 (-63µm) | 2.1 | 1 | 13.6 | 1.32 | 62 | 11.5 | 2.56 | 19.42 | 18.18 | 37.6 | 1.07 | 40.69 | 47.17 | 87.85 |
| AJ117619 (-63µm) | 1.79 | 0.8 | 12.7 | 1.22 | 40 | 13.8 | 3.22 | 24.42 | 21.21 | 45.63 | 1.15 | 47.46 | 59.33 | 106.79 |
| AJ118419 (-63µm) | 1.39 | 0.8 | 11.4 | 1.04 | 35 | 14.2 | 3.84 | 29.13 | 19.65 | 48.78 | 1.48 | 43.98 | 70.75 | 114.73 |
| AJ118519 (-63µm) | 1.84 | 0.8 | 11.5 | 1.08 | 38 | 15.4 | 3.74 | 28.37 | 23.06 | 51.43 | 1.23 | 51.61 | 68.91 | 120.52 |
| AJ118619 (-63µm) | 1.87 | 0.7 | 11.7 | 1.12 | 36 | 13 | 2.84 | 21.54 | 20.77 | 42.31 | 1.04 | 46.49 | 52.33 | 98.81 |
| AJ118819 (-63µm) | 1.46 | 0.6 | 11.3 | 1.07 | 33 | 14.7 | 3.44 | 26.09 | 22.55 | 48.64 | 1.16 | 50.46 | 63.38 | 113.84 |
| AJ119019 (-63µm) | 1.62 | 1 | 11.6 | 1.11 | 43 | 15.7 | 3.32 | 25.18 | 25.54 | 50.72 | 0.99 | 57.16 | 61.17 | 118.33 |
| AJ119119 (-63µm) | 1.73 | 1 | 13.8 | 1.29 | 55 | 13.4 | 2.79 | 21.16 | 21.98 | 43.14 | 0.96 | 49.19 | 51.4 | 100.59 |
| AJ119219 (-63µm) | 1.4 | 0.7 | 10.5 | 1.05 | 36 | 16.5 | 3.68 | 27.91 | 26.05 | 53.97 | 1.07 | 58.31 | 67.8 | 126.11 |
| AJ119319 (-63µm) | 1.35 | 0.6 | 11.1 | 1.04 | 36 | 16.2 | 3.72 | 28.22 | 25.14 | 53.36 | 1.12 | 56.27 | 68.54 | 124.8 |
| AJ119619 (-63µm) | 1.46 | 0.7 | 11.5 | 1.1 | 38 | 14.8 | 3.41 | 25.87 | 22.92 | 48.79 | 1.13 | 51.3 | 62.83 | 114.12 |
| AJ119719 (-63µm) | 1.54 | 1 | 13.3 | 1.32 | 52 | 13.7 | 3.09 | 23.44 | 21.49 | 44.93 | 1.09 | 48.1 | 56.93 | 105.03 |
| AJ119819 (-63µm) | 2.1 | 1.1 | 13.3 | 1.28 | 51 | 14.1 | 2.92 | 22.15 | 23.19 | 45.34 | 0.96 | 51.9 | 53.8 | 105.7 |
| AJ119919 (-63µm) | 1.44 | 0.8 | 11.7 | 1.09 | 39 | 15.6 | 3.34 | 25.33 | 25.21 | 50.54 | 1.01 | 56.41 | 61.54 | 117.95 |
| DCB01/BR2 | 126 | 10.4 | 21.6 | 1.97 | 130 | 5.26 | 1.64 | 12.44 | 6.38 | 18.82 | 1.95 | 14.29 | 30.22 | 44.5 |
| AJ120019 (-63µm) | 1.45 | 0.8 | 11.9 | 1.12 | 55 | 14.6 | 3.41 | 25.87 | 22.42 | 48.29 | 1.15 | 50.18 | 62.83 | 113.01 |
| AJ120219 (-63µm) | 1.57 | 1.1 | 16 | 1.34 | 53 | 12.8 | 3.13 | 23.74 | 19.08 | 42.82 | 1.24 | 42.7 | 57.67 | 100.37 |
| AJ120319 (-63µm) | 1.19 | 0.8 | 10.9 | 1.06 | 30 | 15.9 | 3.38 | 25.64 | 25.79 | 51.43 | 0.99 | 57.72 | 62.27 | 120 |
| AJ120419 (-63µm) | 1.63 | 0.7 | 11 | 1.06 | 44 | 15.7 | 3.84 | 29.13 | 23.4 | 52.53 | 1.24 | 52.37 | 70.75 | 123.11 |
| AJ120619 (-63µm) | 1.15 | 0.7 | 11.1 | 1.03 | 57 | 17.6 | 3.52 | 26.7 | 29.46 | 56.16 | 0.91 | 65.93 | 64.85 | 130.79 |
| AJ120719 (-63µm) | 1.21 | 0.8 | 10.9 | 1.03 | 40 | 14 | 3.8 | 28.82 | 19.32 | 48.14 | 1.49 | 43.23 | 70.01 | 113.25 |
| AJ120819 (-63µm) | 1.55 | 1.3 | 11.5 | 1.07 | 41 | 14.1 | 3.85 | 29.2 | 19.36 | 48.56 | 1.51 | 43.33 | 70.93 | 114.26 |
| AJ120919 (-63µm) | 1.81 | 1.1 | 14 | 1.35 | 54 | 9.95 | 2.3 | 17.45 | 15.38 | 32.82 | 1.13 | 34.42 | 42.38 | 76.79 |
| AJ121019 (-63µm) | 1.39 | 0.8 | 12.5 | 1.17 | 48 | 11.4 | 3 | 22.76 | 16.12 | 38.87 | 1.41 | 36.07 | 55.27 | 91.35 |
| AJ121119 (-63µm) | 1.57 | 0.7 | 12.1 | 1.13 | 45 | 11.2 | 3.01 | 22.83 | 15.58 | 38.41 | 1.47 | 34.86 | 55.46 | 90.32 |
| AJ121219 (-63µm) | 1.58 | 1 | 14.2 | 1.31 | 61 | 13.2 | 2.84 | 21.54 | 21.27 | 42.81 | 1.01 | 47.61 | 52.33 | 99.93 |
| AJ121319 (-63µm) | 1.56 | 0.7 | 12.5 | 1.14 | 41 | 13.5 | 3.41 | 25.87 | 19.67 | 45.54 | 1.31 | 44.03 | 62.83 | 106.86 |
| AJ121419 (-63µm) | 1.39 | 0.9 | 14.5 | 1.37 | 62 | 9.94 | 2.43 | 18.43 | 14.82 | 33.25 | 1.24 | 33.16 | 44.77 | 77.94 |
| AJ121519 (-63µm) | 1.24 | 0.6 | 10.8 | 0.99 | 33 | 14.7 | 3.64 | 27.61 | 21.72 | 49.33 | 1.27 | 48.62 | 67.07 | 115.68 |
| AJ121619 (-63µm) | 1.51 | 0.7 | 11.3 | 1.08 | 41 | 16.4 | 3.91 | 29.66 | 24.86 | 54.52 | 1.19 | 55.63 | 72.04 | 127.67 |
| AJ121719 (-63µm) | 1.89 | 1 | 13.5 | 1.32 | 53 | 12.8 | 2.97 | 22.53 | 19.74 | 42.27 | 1.14 | 44.17 | 54.72 | 98.89 |
| AJ121819 (-63µm) | 1.55 | 1.8 | 14.5 | 1.36 | 64 | 12 | 2.52 | 19.11 | 19.59 | 38.71 | 0.98 | 43.85 | 46.43 | 90.28 |
| AJ121919 (-63µm) | 1.69 | 0.9 | 13.4 | 1.42 | 51 | 13.9 | 2.99 | 22.68 | 22.4 | 45.08 | 1.01 | 50.14 | 55.09 | 105.23 |
| AJ121819 (-63µm) R | 1.51 | 1.1 | 14.2 | 1.32 | 62 | 12.1 | 2.51 | 19.04 | 19.88 | 38.92 | 0.96 | 44.5 | 46.25 | 90.74 |
| DCB01/BR2 | 123 | 10.9 | 21.3 | 1.93 | 126 | 5.21 | 1.6 | 12.14 | 6.42 | 18.56 | 1.89 | 14.38 | 29.48 | 43.86 |
| AJ122019 (-63µm) | 2.02 | 1 | 14.3 | 1.36 | 55 | 9.8 | 2.22 | 16.84 | 15.33 | 32.17 | 1.1 | 34.32 | 40.9 | 75.22 |
| AJ122119 (-63µm) | 1.98 | 1 | 14.6 | 1.33 | 54 | 9.96 | 2.27 | 17.22 | 15.53 | 32.75 | 1.11 | 34.75 | 41.82 | 76.57 |
| AJ122219 (-63µm) | 1.86 | 0.9 | 14.6 | 1.35 | 54 | 9.68 | 2.25 | 17.07 | 14.91 | 31.98 | 1.14 | 33.37 | 41.46 | 74.82 |
| AJ122419 (-63µm) | 1.26 | 0.6 | 10.6 | 0.99 | 36 | 17.1 | 3.55 | 26.93 | 28.09 | 55.02 | 0.96 | 62.86 | 65.41 | 128.27 |
| AJ122519 (-63µm) | 1.72 | 0.9 | 14.2 | 1.3 | 52 | 9.83 | 2.29 | 17.37 | 15.12 | 32.49 | 1.15 | 33.84 | 42.19 | 76.03 |
| AJ122919 (-63µm) | 1.08 | 0.6 | 10.6 | 0.96 | 37 | 16.6 | 3.69 | 27.99 | 26.26 | 54.25 | 1.07 | 58.78 | 67.99 | 126.76 |
| AJ123019 (-63µm) | 1.55 | 0.9 | 13.8 | 1.27 | 54 | 13.6 | 2.88 | 21.85 | 22.11 | 43.95 | 0.99 | 49.47 | 53.06 | 102.54 |
| AJ123119 (-63µm) | 1.28 | 0.6 | 11.1 | 1.01 | 36 | 16.4 | 3.6 | 27.31 | 26.13 | 53.44 | 1.04 | 58.49 | 66.33 | 124.82 |
| AJ123319 (-63µm) | 1.46 | 0.7 | 11.3 | 1.04 | 37 | 16.2 | 3.43 | 26.02 | 26.33 | 52.35 | 0.99 | 58.94 | 63.2 | 122.13 |
| AJ123419 (-63µm) | 1.39 | 0.7 | 11.3 | 1.03 | 39 | 15.7 | 3.25 | 24.65 | 25.83 | 50.48 | 0.95 | 57.8 | 59.88 | 117.68 |
| AJ123519 (-63µm) | 1.78 | 0.8 | 12 | 1.12 | 47 | 11.1 | 2.89 | 21.92 | 15.82 | 37.74 | 1.39 | 35.41 | 53.25 | 88.66 |
| AJ123619 (-63µm) | 1.69 | 1 | 12.9 | 1.22 | 51 | 13.4 | 2.98 | 22.6 | 21.2 | 43.8 | 1.07 | 47.43 | 54.9 | 102.34 |
| AJ123619 (-63µm) R | 1.71 | 1 | 13.4 | 1.27 | 52 | 13.2 | 2.92 | 22.15 | 20.94 | 43.09 | 1.06 | 46.87 | 53.8 | 100.67 |

# Appendix E. Geochemistry QAQC

| PSA Standards | | | | | |
|---|---|---|---|---|---|
| Description | Date | Sample Type | Sand PSA wt% | Silt PSA wt% | Clay PSA wt% |
| SSC0219 | 10-02-2019 | Standard | 25.4 | 45.6 | 29 |
| SSC0219 | 10-02-2019 | Standard | 25.4 | 45.7 | 28.9 |
| SSC0219 | 10-02-2019 | Standard | 25.2 | 46 | 28.8 |
| | | Average: | 25.3 | 45.8 | 28.9 |
| | | Standard Dev: | 0.1 | 0.2 | 0.1 |
| | | **%RSD:** | **0.46** | **0.45** | **0.35** |
| | | SSC0219 certified value: | 25.7 | 45.2 | 29.1 |
| | | **%RD** | **1.4** | **1.3** | **0.7** |

| PSA Duplicates | | | | | |
|---|---|---|---|---|---|
| Description | Date | Sample Type | Sand PSA wt% | Silt PSA wt% | Clay PSA wt% |
| AJ121819 (-2mm) | 10-02-2019 | Soil | 19.9 | 53.1 | 27 |
| AJ121819 (-2mm) R | 10-02-2019 | Repeat | 19.7 | 53.3 | 27 |
| AJ123619 (-2mm) | 10-02-2019 | Soil | 24 | 55 | 21 |
| AJ123619 (-2mm) R | 10-02-2019 | Repeat | 23.2 | 55 | 21.8 |
| | | **CVavg%** | **1.8** | **0.2** | **1.9** |

| Geochemistry Standards | | | | | | | | | | |
|---|---|---|---|---|---|---|---|---|---|---|
| | Description: | DCB01/BR2 | DCB01/BR2 | DCB01/BR2 | | | | Certified Value | |
| | Date: | 10-04-2019 | 10-04-2019 | 10-04-2019 | | | | DCB01 | |
| | Sample Type: | Standard | Standard | Standard | Average | Standard Dev | **%RSD** | Standard | **%RD** |
| Al2O3 ICP Total Digestion | wt % | 11.1 | 11 | 11.1 | 11.07 | 0.06 | 0.52 | 11.10 | 0.00 |
| Ba ICP Total Digestion | ppm | 382 | 384 | 387 | 384.33 | 2.52 | 0.65 | 387.00 | 0.00 |
| CaO ICP Total Digestion | wt % | 1.51 | 1.51 | 1.5 | 1.51 | 0.01 | 0.38 | 1.50 | 0.00 |
| Ce ICP Total Digestion | ppm | 126 | 130 | 130 | 128.67 | 2.31 | 1.79 | 128.00 | 1.56 |
| Cr ICP Total Digestion | ppm | 258 | 264 | 250 | 257.33 | 7.02 | 2.73 | 270.00 | 7.41 |
| Fe2O3 ICP Total Digestion | wt % | 3.35 | 3.35 | 3.31 | 3.34 | 0.02 | 0.69 | 3.36 | 1.49 |
| K2O ICP Total Digestion | wt % | 2.41 | 2.44 | 2.46 | 2.44 | 0.03 | 1.03 | 2.46 | 0.00 |
| La ICP Total Digestion | ppm | 64 | 63 | 64 | 63.67 | 0.58 | 0.91 | 66.00 | 3.03 |
| Li ICP Total Digestion | ppm | 43 | 43 | 43 | 43.00 | 0.00 | 0.00 | 43.00 | 0.00 |
| MgO ICP Total Digestion | wt % | 1.7 | 1.7 | 1.7 | 1.70 | 0.00 | 0.00 | 1.70 | 0.00 |
| MnO ICP Total Digestion | wt % | 0.036 | 0.036 | 0.035 | 0.035667 | 0.000577 | 1.62 | 0.03 | ***16.67*** |
| Na2O ICP Total Digestion | wt % | 0.56 | 0.57 | 0.58 | 0.57 | 0.01 | 1.75 | 0.58 | 0.00 |
| P2O5 ICP Total Digestion | wt % | 0.208 | 0.211 | 0.211 | 0.21 | 0.00 | 0.82 | 0.21 | 0.48 |
| S ICP Total Digestion | ppm | 3970 | 3980 | 3920 | 3956.67 | 32.15 | 0.81 | 3849.00 | 1.84 |
| Sr ICP Total Digestion | ppm | 404 | 409 | 409 | 407.33 | 2.89 | 0.71 | 401.00 | 2.00 |
| TiO2 ICP Total Digestion | wt % | 0.786 | 0.796 | 0.79 | 0.79 | 0.01 | 0.64 | 0.79 | 0.00 |
| V ICP Total Digestion | ppm | 102 | 101 | 101 | 101.33 | 0.58 | 0.57 | 101.00 | 0.00 |
| Zr ICP Total Digestion | ppm | 399 | 410 | 411 | 406.67 | 6.66 | 1.64 | 419.00 | 1.91 |
| Ag ICP MS Partial Digestion | ppm | 2.42 | 2.47 | 2.42 | 2.44 | 0.03 | 1.18 | 2.59 | 6.56 |
| As ICP MS Partial Digestion | ppm | 30.3 | 30.6 | 30.1 | 30.33 | 0.25 | 0.83 | 28.60 | 5.24 |
| Be ICP MS Partial Digestion | ppm | 0.42 | 0.45 | 0.46 | 0.44 | 0.02 | 4.70 | 0.52 | ***11.54*** |
| Bi ICP MS Partial Digestion | ppm | 6.48 | 6.78 | 6.71 | 6.66 | 0.16 | 2.36 | 6.71 | 0.00 |
| Cd ICP MS Partial Digestion | ppm | 0.42 | 0.44 | 0.45 | 0.44 | 0.02 | 3.50 | 0.51 | ***11.76*** |
| Co ICP MS Partial Digestion | ppm | 13.8 | 13.4 | 13.6 | 13.60 | 0.20 | 1.47 | 14.30 | 4.90 |
| Cs ICP MS Partial Digestion | ppm | 0.4 | 0.42 | 0.43 | 0.42 | 0.02 | 3.67 | 0.40 | 7.50 |
| Cu ICP MS Partial Digestion | ppm | 269 | 267 | 268 | 268.00 | 1.00 | 0.37 | 270.00 | 0.74 |
| Dy ICP MS Partial Digestion | ppm | 1.64 | 1.73 | 1.7 | 1.69 | 0.05 | 2.71 | 1.65 | 3.03 |
| Er ICP MS Partial Digestion | ppm | 0.75 | 0.79 | 0.79 | 0.78 | 0.02 | 2.97 | 0.79 | 0.00 |
| Eu ICP MS Partial Digestion | ppm | 0.49 | 0.52 | 0.51 | 0.51 | 0.02 | 3.01 | 0.51 | 0.00 |
| Ga ICP MS Partial Digestion | ppm | 2.08 | 2.07 | 2.02 | 2.06 | 0.03 | 1.56 | 2.04 | 0.98 |
| Gd ICP MS Partial Digestion | ppm | 2.33 | 2.36 | 2.32 | 2.34 | 0.02 | 0.89 | 2.28 | 1.75 |
| Ge ICP MS Partial Digestion | ppm | <0.01 | <0.01 | <0.01 | | | | 0.02 | |
| Hf ICP MS Partial Digestion | ppm | 0.72 | 0.71 | 0.71 | 0.71 | 0.01 | 0.81 | 0.71 | 0.00 |
| Hg ICP MS Partial Digestion | ppm | 0.1 | 0.1 | 0.09 | 0.10 | 0.01 | 5.97 | 0.35 | ***74.29*** |
| Ho ICP MS Partial Digestion | ppm | 0.29 | 0.29 | 0.29 | 0.29 | 0.00 | 0.00 | 0.29 | 0.00 |
| Mo ICP MS Partial Digestion | ppm | 10.5 | 11.1 | 11 | 10.87 | 0.32 | 2.96 | 10.70 | 2.80 |
| Nb ICP MS Partial Digestion | ppm | 0.09 | 0.1 | 0.1 | 0.10 | 0.01 | 5.97 | 0.09 | ***11.11*** |
| Nd ICP MS Partial Digestion | ppm | 15.7 | 16.2 | 15.9 | 15.93 | 0.25 | 1.58 | 15.90 | 0.00 |
| Ni ICP MS Partial Digestion | ppm | 52.2 | 53.2 | 51.3 | 52.23 | 0.95 | 1.82 | 52.30 | 1.91 |
| Pb204 ICP MS Partial Digestion | ppm | 1.2 | 1.19 | 1.18 | 1.19 | 0.01 | 0.84 | 1.18 | 0.00 |
| Pb206 ICP MS Partial Digestion | ppm | 29.4 | 29.5 | 29.2 | 29.37 | 0.15 | 0.52 | 29.80 | 2.01 |
| Pb207 ICP MS Partial Digestion | ppm | 18.3 | 18.2 | 18.5 | 18.33 | 0.15 | 0.83 | 18.10 | 2.21 |
| Pb208 ICP MS Partial Digestion | ppm | 41.6 | 42.3 | 42 | 41.97 | 0.35 | 0.84 | 42.50 | 1.18 |
| PbSUM ICP MS Partial Digestion | ppm | 91.5 | 91.2 | 90.9 | 91.20 | 0.30 | 0.33 | 91.50 | 0.66 |
| Pr ICP MS Partial Digestion | ppm | 4.27 | 4.37 | 4.3 | 4.31 | 0.05 | 1.19 | 4.32 | 0.46 |
| Rb ICP MS Partial Digestion | ppm | 9.96 | 10.2 | 10 | 10.05 | 0.13 | 1.28 | 9.85 | 1.52 |
| Sb ICP MS Partial Digestion | ppm | 0.31 | 0.3 | 0.34 | 0.32 | 0.02 | 6.57 | 0.31 | 9.68 |
| Sc ICP MS Partial Digestion | ppm | 2 | 1.9 | 1.9 | 1.93 | 0.06 | 2.99 | 1.90 | 0.00 |
| Se ICP MS Partial Digestion | ppm | 0.6 | 0.6 | 0.7 | 0.63 | 0.06 | 9.12 | 0.70 | 0.00 |
| Sm ICP MS Partial Digestion | ppm | 2.73 | 2.75 | 2.66 | 2.71 | 0.05 | 1.74 | 2.78 | 4.32 |
| Sn ICP MS Partial Digestion | ppm | 1.04 | 1.07 | 1.11 | 1.07 | 0.04 | 3.27 | 1.07 | 3.74 |
| Ta ICP MS Partial Digestion | ppm | <0.01 | <0.01 | <0.01 | | | | 0.01 | |
| Tb ICP MS Partial Digestion | ppm | 0.28 | 0.29 | 0.29 | 0.29 | 0.01 | 2.01 | 0.29 | 0.00 |
| Te ICP MS Partial Digestion | ppm | 0.13 | 0.12 | 0.13 | 0.13 | 0.01 | 4.56 | 0.12 | 8.33 |

| | | | | | | | | | |
|---|---|---|---|---|---|---|---|---|---|
| Th ICP MS Partial Digestion | ppm | 13.8 | 14.2 | 14.1 | 14.03 | 0.21 | 1.48 | 13.90 | 1.44 |
| U ICP MS Partial Digestion | ppm | 112 | 114 | 113 | 113.00 | 1.00 | 0.88 | 111.00 | 1.80 |
| V ICP MS Partial Digestion | ppm | 28.3 | 29 | 28.4 | 28.57 | 0.38 | 1.33 | 27.80 | 2.16 |
| W ICP MS Partial Digestion | ppm | 4.8 | 4.6 | 4.7 | 4.70 | 0.10 | 2.13 | 4.80 | 2.08 |
| Y ICP MS Partial Digestion | ppm | 6.77 | 6.85 | 6.96 | 6.86 | 0.10 | 1.39 | 7.04 | 1.14 |
| Yb ICP MS Partial Digestion | ppm | 0.56 | 0.59 | 0.59 | 0.58 | 0.02 | 2.99 | 0.61 | 3.28 |
| Zn ICP MS Partial Digestion | ppm | 120 | 121 | 122 | 121.00 | 1.00 | 0.83 | 121.00 | 0.83 |
| Zr ICP MS Partial Digestion | ppm | 30.9 | 30.2 | 29.6 | 30.23 | 0.65 | 2.15 | 29.10 | 1.72 |
| Ag ICP MS Total Digestion | ppm | 2.68 | 2.73 | 2.87 | 2.76 | 0.10 | 3.57 | 2.82 | 1.77 |
| Be ICP MS Total Digestion | ppm | 1.9 | 1.6 | 1.6 | 1.70 | 0.17 | ***10.19*** | 1.50 | 6.67 |
| Bi ICP MS Total Digestion | ppm | 7.8 | 7.7 | 7.8 | 7.77 | 0.06 | 0.74 | 8.30 | 6.02 |
| Cd ICP MS Total Digestion | ppm | 0.8 | 0.9 | 0.9 | 0.87 | 0.06 | 6.66 | 0.70 | ***28.57*** |
| Co ICP MS Total Digestion | ppm | 17.9 | 16.8 | 17.3 | 17.33 | 0.55 | 3.18 | 17.20 | 0.58 |
| Cs ICP MS Total Digestion | ppm | 1 | 1.1 | 1.1 | 1.07 | 0.06 | 5.41 | 1.10 | 0.00 |
| Cu ICP MS Total Digestion | ppm | 274 | 275 | 278 | 275.67 | 2.08 | 0.76 | 275.00 | 1.09 |
| Dy ICP MS Total Digestion | ppm | 4.46 | 4.51 | 4.63 | 4.53 | 0.09 | 1.93 | 4.16 | ***11.30*** |
| Er ICP MS Total Digestion | ppm | 2.2 | 2.2 | 2.26 | 2.22 | 0.03 | 1.56 | 2.14 | 5.61 |
| Eu ICP MS Total Digestion | ppm | 1.28 | 1.32 | 1.31 | 1.30 | 0.02 | 1.60 | 1.23 | 6.50 |
| Ga ICP MS Total Digestion | ppm | 14.1 | 14.4 | 14.6 | 14.37 | 0.25 | 1.75 | 15.00 | 2.67 |
| Gd ICP MS Total Digestion | ppm | 5.6 | 5.8 | 6 | 5.80 | 0.20 | 3.45 | 5.80 | 3.45 |
| Hf ICP MS Total Digestion | ppm | 11 | 10.4 | 10.1 | 10.50 | 0.46 | 4.36 | 11.10 | 9.01 |
| Ho ICP MS Total Digestion | ppm | 0.77 | 0.74 | 0.77 | 0.76 | 0.02 | 2.28 | 0.77 | 0.00 |
| Mo ICP MS Total Digestion | ppm | 12.1 | 12.3 | 12.2 | 12.20 | 0.10 | 0.82 | 12.40 | 1.61 |
| Nb ICP MS Total Digestion | ppm | 20.1 | 20.4 | 19.8 | 20.10 | 0.30 | 1.49 | 19.50 | 1.54 |
| Nd ICP MS Total Digestion | ppm | 46.9 | 47.2 | 49.1 | 47.73 | 1.19 | 2.50 | 48.40 | 1.45 |
| Ni ICP MS Total Digestion | ppm | 97.5 | 96.6 | 97.6 | 97.23 | 0.55 | 0.57 | 101.00 | 3.37 |
| Pb204 ICP MS Total Digestion | ppm | 1.32 | 1.32 | 1.31 | 1.32 | 0.01 | 0.44 | 1.23 | 6.50 |
| Pb206 ICP MS Total Digestion | ppm | 33.3 | 33.3 | 33.3 | 33.30 | 0.00 | 0.00 | 33.63 | 0.98 |
| Pb207 ICP MS Total Digestion | ppm | 19.8 | 19.7 | 19.7 | 19.73 | 0.06 | 0.29 | 19.12 | 3.03 |
| Pb208 ICP MS Total Digestion | ppm | 47.4 | 47.5 | 47.8 | 47.57 | 0.21 | 0.44 | 47.42 | 0.80 |
| PbSUM ICP MS Total Digestion | ppm | 102 | 102 | 102 | 102.00 | 0.00 | 0.00 | 103.20 | 1.16 |
| Pr ICP MS Total Digestion | ppm | 13.4 | 13.6 | 14.2 | 13.73 | 0.42 | 3.03 | 13.30 | 6.77 |
| Rb ICP MS Total Digestion | ppm | 60.5 | 62.8 | 61.6 | 61.63 | 1.15 | 1.87 | 61.40 | 0.33 |
| Sc ICP MS Total Digestion | ppm | 7.3 | 6.8 | 6.8 | 6.97 | 0.29 | 4.14 | 6.90 | 1.45 |
| Sm ICP MS Total Digestion | ppm | 7.9 | 8 | 8 | 7.97 | 0.06 | 0.72 | 7.70 | 3.90 |
| Sn ICP MS Total Digestion | ppm | 3.24 | 3.33 | 3.45 | 3.34 | 0.11 | 3.15 | 3.01 | ***14.62*** |
| Ta ICP MS Total Digestion | ppm | 1.61 | 1.53 | 1.67 | 1.60 | 0.07 | 4.38 | 1.65 | 1.21 |
| Tb ICP MS Total Digestion | ppm | 0.73 | 0.74 | 0.81 | 0.76 | 0.04 | 5.74 | 0.76 | 6.58 |
| Th ICP MS Total Digestion | ppm | 52.5 | 50.1 | 51.2 | 51.27 | 1.20 | 2.34 | 51.90 | 1.35 |
| U ICP MS Total Digestion | ppm | 126 | 126 | 123 | 125.00 | 1.73 | 1.39 | 124.00 | 0.81 |
| W ICP MS Total Digestion | ppm | 10.4 | 10.4 | 10.9 | 10.57 | 0.29 | 2.73 | 11.60 | 6.03 |
| Y ICP MS Total Digestion | ppm | 21.4 | 21.6 | 21.3 | 21.43 | 0.15 | 0.71 | 21.50 | 0.93 |
| Yb ICP MS Total Digestion | ppm | 1.95 | 1.97 | 1.93 | 1.95 | 0.02 | 1.03 | 1.90 | 1.58 |
| Zn ICP MS Total Digestion | ppm | 128 | 130 | 126 | 128.00 | 2.00 | 1.56 | 126.00 | 0.00 |
| Ca Calcium Magnesium | wt % | 5.13 | 5.26 | 5.21 | 5.20 | 0.07 | 1.26 | 4.96 | 5.04 |
| Mg Calcium Magnesium | wt % | 1.6 | 1.64 | 1.6 | 1.61 | 0.02 | 1.43 | 1.54 | 3.90 |
| Dol Calcium Magnesium | wt% | 12.14 | 12.44 | 12.14 | 12.24 | 0.17 | 1.42 | N/A | |
| Cal Calcium Magnesium | wt% | 6.22 | 6.38 | 6.42 | 6.34 | 0.11 | 1.67 | N/A | |
| CO3 Calcium Magnesium | wt% | 18.36 | 18.82 | 18.56 | 18.58 | 0.23 | 1.24 | N/A | |
| Dol/Cal Calcium Magnesium | ml | 1.95 | 1.95 | 1.89 | 1.93 | 0.03 | 1.79 | N/A | |
| CO2Cal Calcium Magnesium | ml | 13.93 | 14.29 | 14.38 | 14.20 | 0.24 | 1.68 | N/A | |
| CO2Dol Calcium Magnesium | ml | 29.48 | 30.22 | 29.48 | 29.73 | 0.43 | 1.44 | N/A | |
| CO2Tot Calcium Magnesium | ml | 43.41 | 44.5 | 43.86 | 43.92 | 0.55 | 1.25 | N/A | |

**Geochemistry Duplicates**

| | Description: | AJ121819 | AJ121819 R | AJ123619 | AJ123619 R | |
|---|---|---|---|---|---|---|
| | Size: | -63µm | -63µm | -63µm | -63µm | |
| | Date: | 10-04-2019 | 10-04-2019 | 10-04-2019 | 10-04-2019 | |
| | Sample Type: | Basement | Repeat | Basement | Repeat | CVavg% |
| Al2O3 ICP Total Digestion | wt % | 11.9 | 11.7 | 10.3 | 10.4 | 1.0 |
| Ba ICP Total Digestion | ppm | 491 | 490 | 449 | 452 | 0.3 |
| CaO ICP Total Digestion | wt % | 17.3 | 17.1 | 18.7 | 18.8 | 0.6 |
| Ce ICP Total Digestion | ppm | 69 | 67 | 57 | 58 | 1.7 |
| Cr ICP Total Digestion | ppm | 57 | 55 | 48 | 49 | 2.1 |
| Fe2O3 ICP Total Digestion | wt % | 4.23 | 4.2 | 3.4 | 3.42 | 0.5 |
| K2O ICP Total Digestion | wt % | 2.96 | 2.94 | 2.58 | 2.62 | 0.8 |
| La ICP Total Digestion | ppm | 34 | 33 | 29 | 30 | 2.3 |
| Li ICP Total Digestion | ppm | 43 | 41 | 35 | 36 | 2.8 |
| MgO ICP Total Digestion | wt % | 5.2 | 5.18 | 5.65 | 5.69 | 0.4 |
| MnO ICP Total Digestion | wt % | 0.067 | 0.066 | 0.049 | 0.05 | 1.3 |
| Na2O ICP Total Digestion | wt % | 1.58 | 1.5 | 1.56 | 1.57 | 2.6 |
| P2O5 ICP Total Digestion | wt % | 0.14 | 0.138 | 0.127 | 0.131 | 1.7 |
| S ICP Total Digestion | ppm | <10 | <10 | 27 | 24 | |
| Sr ICP Total Digestion | ppm | 227 | 221 | 224 | 228 | 1.6 |
| TiO2 ICP Total Digestion | wt % | 0.562 | 0.557 | 0.491 | 0.502 | 1.2 |
| V ICP Total Digestion | ppm | 73.9 | 72.9 | 60.6 | 61 | 0.8 |
| Zr ICP Total Digestion | ppm | 127 | 125 | 125 | 127 | 1.1 |

| | | | | | | | |
|---|---|---|---|---|---|---|---|
| Ag ICP MS Partial Digestion | ppm | | 0.02 | | 0.02 | 0.02 | 0.0 |
| As ICP MS Partial Digestion | ppm | | 2.49 | | 2.56 | 1.98 | 1.9 | 2.5 |
| Be ICP MS Partial Digestion | ppm | | 0.47 | | 0.51 | 0.32 | 0.34 | 5.1 |
| Bi ICP MS Partial Digestion | ppm | | 0.11 | | 0.12 | 0.09 | 0.09 | 4.3 |
| Cd ICP MS Partial Digestion | ppm | | 0.06 | | 0.07 | 0.07 | 0.07 | ***7.7*** |
| Co ICP MS Partial Digestion | ppm | | 6.47 | | 6.57 | 4.62 | 4.61 | 0.8 |
| Cs ICP MS Partial Digestion | ppm | | 1.11 | | 1.15 | 0.95 | 0.96 | 1.8 |
| Cu ICP MS Partial Digestion | ppm | | 14.2 | | 14.1 | 11.4 | 11.2 | 1.0 |
| Dy ICP MS Partial Digestion | ppm | | 1.82 | | 1.89 | 1.65 | 1.59 | 2.6 |
| Er ICP MS Partial Digestion | ppm | | 0.89 | | 0.92 | 0.77 | 0.79 | 2.1 |
| Eu ICP MS Partial Digestion | ppm | | 0.63 | | 0.66 | 0.54 | 0.54 | 2.3 |
| Ga ICP MS Partial Digestion | ppm | | 3.38 | | 3.38 | 2.7 | 2.68 | 0.4 |
| Gd ICP MS Partial Digestion | ppm | | 2.88 | | 3.04 | 2.55 | 2.54 | 2.7 |
| Ge ICP MS Partial Digestion | ppm | <0.01 | | <0.01 | | <0.01 | <0.01 | |
| Hf ICP MS Partial Digestion | ppm | | 0.33 | | 0.35 | 0.31 | 0.32 | 3.3 |
| Hg ICP MS Partial Digestion | ppm | | 0.02 | <0.01 | | 0.02 | 0.02 | |
| Ho ICP MS Partial Digestion | ppm | | 0.31 | | 0.32 | 0.27 | 0.27 | 1.6 |
| Mo ICP MS Partial Digestion | ppm | | 0.15 | | 0.16 | 0.17 | 0.17 | 3.2 |
| Nb ICP MS Partial Digestion | ppm | | 0.07 | | 0.08 | 0.06 | 0.07 | ***10.2*** |
| Nd ICP MS Partial Digestion | ppm | | 20.5 | | 21.6 | 18 | 18 | 2.6 |
| Ni ICP MS Partial Digestion | ppm | | 20.4 | | 21.2 | 16.5 | 16.4 | 1.9 |
| Pb204 ICP MS Partial Digestion | ppm | | 0.097 | | 0.094 | 0.074 | 0.074 | 1.6 |
| Pb206 ICP MS Partial Digestion | ppm | | 1.93 | | 1.96 | 1.49 | 1.48 | 0.8 |
| Pb207 ICP MS Partial Digestion | ppm | | 1.51 | | 1.5 | 1.14 | 1.15 | 0.5 |
| Pb208 ICP MS Partial Digestion | ppm | | 3.85 | | 3.88 | 2.89 | 2.93 | 0.8 |
| PbSUM ICP MS Partial Digestion | ppm | | 7.38 | | 7.44 | 5.59 | 5.64 | 0.6 |
| Pr ICP MS Partial Digestion | ppm | | 5.83 | | 5.9 | 5.11 | 5.1 | 0.6 |
| Rb ICP MS Partial Digestion | ppm | | 18.9 | | 18.9 | 16.6 | 16.8 | 0.6 |
| Sb ICP MS Partial Digestion | ppm | | 0.03 | | 0.03 | 0.04 | 0.04 | 0.0 |
| Sc ICP MS Partial Digestion | ppm | | 2.8 | | 2.8 | 2.3 | 2.3 | 0.0 |
| Se ICP MS Partial Digestion | ppm | | 0.4 | | 0.2 | 0.3 | 0.3 | ***33.3*** |
| Sm ICP MS Partial Digestion | ppm | | 3.32 | | 3.35 | 2.92 | 2.93 | 0.5 |
| Sn ICP MS Partial Digestion | ppm | | 0.37 | | 0.38 | 0.33 | 0.34 | 2.0 |
| Ta ICP MS Partial Digestion | ppm | <0.01 | | <0.01 | | <0.01 | <0.01 | |
| Tb ICP MS Partial Digestion | ppm | | 0.31 | | 0.33 | 0.28 | 0.28 | 3.1 |
| Te ICP MS Partial Digestion | ppm | | 0.02 | | 0.02 | 0.01 | 0.01 | 0.0 |
| Th ICP MS Partial Digestion | ppm | | 8.11 | | 8.13 | 6.51 | 6.58 | 0.5 |
| U ICP MS Partial Digestion | ppm | | 0.54 | | 0.56 | 0.68 | 0.7 | 2.3 |
| V ICP MS Partial Digestion | ppm | | 23 | | 23.4 | 19 | 18.2 | 2.3 |
| W ICP MS Partial Digestion | ppm | | 0.2 | | 0.2 | 0.3 | 0.3 | 0.0 |
| Y ICP MS Partial Digestion | ppm | | 7.36 | | 7.41 | 6.57 | 6.52 | 0.5 |
| Yb ICP MS Partial Digestion | ppm | | 0.66 | | 0.67 | 0.58 | 0.58 | 0.8 |
| Zn ICP MS Partial Digestion | ppm | | 32.3 | | 32.6 | 29.6 | 29.5 | 0.5 |
| Zr ICP MS Partial Digestion | ppm | | 14.5 | | 14.7 | 12.6 | 12.7 | 0.8 |
| Ag ICP MS Total Digestion | ppm | | 0.2 | | 0.2 | 0.19 | 0.19 | 0.0 |
| Be ICP MS Total Digestion | ppm | | 1.7 | | 1.3 | 1.1 | 1.2 | ***14.0*** |
| Bi ICP MS Total Digestion | ppm | | 0.3 | | 0.3 | 0.2 | 0.2 | 0.0 |
| Cd ICP MS Total Digestion | ppm | | 0.3 | | 0.3 | 0.3 | 0.3 | 0.0 |
| Co ICP MS Total Digestion | ppm | | 11.3 | | 11 | 8.33 | 8.37 | 1.4 |
| Cs ICP MS Total Digestion | ppm | | 3.4 | | 3.2 | 2.5 | 2.6 | 3.6 |
| Cu ICP MS Total Digestion | ppm | | 23.4 | | 23.7 | 19.4 | 19.2 | 0.8 |
| Dy ICP MS Total Digestion | ppm | | 2.84 | | 2.77 | 2.54 | 2.59 | 1.6 |
| Er ICP MS Total Digestion | ppm | | 1.52 | | 1.47 | 1.34 | 1.39 | 2.5 |
| Eu ICP MS Total Digestion | ppm | | 1.07 | | 1.05 | 0.93 | 0.95 | 1.4 |
| Ga ICP MS Total Digestion | ppm | | 13.1 | | 12.7 | 11 | 11.2 | 1.8 |
| Gd ICP MS Total Digestion | ppm | | 3.5 | | 3.4 | 3 | 3.1 | 2.2 |
| Hf ICP MS Total Digestion | ppm | | 3.2 | | 3 | 3 | 3.2 | 4.6 |
| Ho ICP MS Total Digestion | ppm | | 0.51 | | 0.5 | 0.45 | 0.46 | 1.5 |
| Mo ICP MS Total Digestion | ppm | | 0.35 | | 0.31 | 0.29 | 0.31 | 6.9 |
| Nb ICP MS Total Digestion | ppm | | 8.5 | | 8.1 | 7.5 | 7.6 | 2.5 |
| Nd ICP MS Total Digestion | ppm | | 27 | | 27.3 | 23 | 24.1 | 2.4 |
| Ni ICP MS Total Digestion | ppm | | 34.6 | | 33.4 | 26.5 | 26.7 | 1.8 |
| Pb204 ICP MS Total Digestion | ppm | | 0.209 | | 0.204 | 0.166 | 0.174 | 2.6 |
| Pb206 ICP MS Total Digestion | ppm | | 3.66 | | 3.67 | 2.85 | 2.88 | 0.5 |
| Pb207 ICP MS Total Digestion | ppm | | 3 | | 3.05 | 2.37 | 2.4 | 1.0 |
| Pb208 ICP MS Total Digestion | ppm | | 7.5 | | 7.41 | 5.91 | 6.11 | 1.8 |
| PbSUM ICP MS Total Digestion | ppm | | 14.4 | | 14.3 | 11.3 | 11.6 | 1.4 |
| Pr ICP MS Total Digestion | ppm | | 7.7 | | 7.4 | 6.5 | 6.7 | 2.5 |
| Rb ICP MS Total Digestion | ppm | | 90.2 | | 91.2 | 75.1 | 78 | 2.0 |
| Sc ICP MS Total Digestion | ppm | | 8.3 | | 8 | 6.8 | 7.1 | 2.8 |
| Sm ICP MS Total Digestion | ppm | | 4.8 | | 4.7 | 4 | 4.2 | 2.7 |
| Sn ICP MS Total Digestion | ppm | | 1.46 | | 1.36 | 1.23 | 1.24 | 3.6 |
| Ta ICP MS Total Digestion | ppm | | 0.51 | | 0.51 | 0.45 | 0.46 | 1.1 |
| Tb ICP MS Total Digestion | ppm | | 0.46 | | 0.45 | 0.4 | 0.41 | 1.7 |
| Th ICP MS Total Digestion | ppm | | 10.7 | | 10.5 | 9.41 | 9.53 | 1.1 |
| U ICP MS Total Digestion | ppm | | 1.55 | | 1.51 | 1.69 | 1.71 | 1.4 |
| W ICP MS Total Digestion | ppm | | 1.8 | | 1.1 | 1 | 1 | ***24.1*** |
| Y ICP MS Total Digestion | ppm | | 14.5 | | 14.2 | 12.9 | 13.4 | 2.2 |

| | | | | | | |
|---|---|---|---|---|---|---|
| Yb ICP MS Total Digestion | ppm | 1.36 | 1.32 | 1.22 | 1.27 | 2.5 |
| Zn ICP MS Total Digestion | ppm | 64 | 62 | 51 | 52 | 1.9 |
| Ca Calcium Magnesium | wt % | 12 | 12.1 | 13.4 | 13.2 | 0.9 |
| Mg Calcium Magnesium | wt % | 2.52 | 2.51 | 2.98 | 2.92 | 1.0 |
| Dol Calcium Magnesium | wt% | 19.11 | 19.04 | 22.6 | 22.15 | 1.0 |
| Cal Calcium Magnesium | wt% | 19.59 | 19.88 | 21.2 | 20.94 | 1.0 |
| CO3 Calcium Magnesium | wt% | 38.71 | 38.92 | 43.8 | 43.09 | 0.9 |
| Dol/Cal Calcium Magnesium | ml | 0.98 | 0.96 | 1.07 | 1.06 | 1.1 |
| CO2Cal Calcium Magnesium | ml | 43.85 | 44.5 | 47.43 | 46.87 | 0.9 |
| CO2Dol Calcium Magnesium | ml | 46.43 | 46.25 | 54.9 | 53.8 | 1.0 |
| CO2Tot Calcium Magnesium | ml | 90.28 | 90.74 | 102.34 | 100.67 | 0.9 |

# Appendix F. A-Axis Clast Fabric Script

The script for plotting and analyzing clast fabrics was developed by Martin Ross (Ross, 2022) and modified by the author in late 2022 for project specific requirements.

In [ ]:
```
import os
import glob
import numpy as np
import pandas as pd
import matplotlib.pyplot as plt
import mplstereonet               #stereonet package
import ternary as te              #python-ternary diagram package
from numpy.linalg import eigh
from matplotlib.backends.backend_pdf import PdfPages #This is to generate a multipage pdf for all the figures
```

In [ ]:
```
os.chdir(r'C:\Users\ttaves\OneDrive - Anglo American\Desktop\Fabrics - new\CSV_Files')
```

In [ ]:
```
pwd
```

In [ ]:
```
os.listdir()
```

In [ ]:
```
filelist=glob.glob('*.csv') #creates a list of all csv files
```

In [ ]:
```
for index, file in enumerate(filelist):
    print(index, file)
#This can be useful if working with a large number of files
```

In [ ]:
```
value=filelist[0]   #This is to show that a list can be sliced by index
print(value)
```

In [ ]:
```
print(value[:-4]) #And this shows that the string of filename can also be sliced.
#This will be useful for labels on figures
```

## 1.0 Data

In [ ]:
```
#Import the csv files

index=int(input("What is the index number of the file?"))
```

In [ ]:
```
df=[pd.read_csv(file) for file in filelist][index]   #This will read the chosen csv file
```

In [ ]:
```
df
```

In [ ]:
```
#Create an array from the 'trend' column of the dataframe and display horizontally (one line)
Trend=df.loc[:,'Trend']
Trend=np.hstack(Trend)
```

In [ ]:
```
#Do the same for the plunge data

Plunge=df.loc[:,'Plunge']
Plunge=np.hstack(Plunge)
```

## 2.0 Data projections

In [ ]:
```
#Let's prepare the data to build a rose diagram

#Calculate the number of directions (bins) every 10° using numpy.histogram.

bin_edges = np.arange(-5, 366, 10)                              #numpy.arange(start, stop, step)
trends_in_bins, bin_edges = np.histogram(Trend, bin_edges)
```

In [ ]:
```
Trends=trends_in_bins[0:-1]                 #37 bins
```

In [ ]:
```
#Initialize the pdf file that will contain all the figures
pp = PdfPages(f'{filelist[index][:-4]}_Figures.pdf')


#Create the rose diagram and the stereonets.

fig = plt.figure(figsize=(12, 12))         #creates an empty figure with no Axes

ax1 = fig.add_subplot(221, projection='stereonet')
ax1.line(Plunge, Trend, 'o', color='blue')
ax1.set_title(f'a-axis on stereonet from {filelist[index][:-4]}', y=1.10, fontsize=15)

#Rose diagram
ax2 = fig.add_subplot(222, projection='polar')
ax2.set_title('a-axis on rose diagram', y=1.10, fontsize=15)

ax2.bar(np.deg2rad(np.arange(0, 360, 10)), Trends,
       width=np.deg2rad(10), bottom=0.0, color='.8', edgecolor='k')
ax2.set_theta_zero_location('N')
ax2.set_theta_direction(-1)
ax2.set_thetagrids(np.arange(0, 360, 30), labels=np.arange(0, 360, 30))
```

```
ax2.set_rgrids(np.arange(1, Trends.max() + 4, 3), angle=0, weight= 'black')

ax3 = fig.add_subplot(223, projection='stereonet')
ax3.line(Plunge, Trend, 'o', color='blue')
m=ax3.density_contourf(Plunge, Trend, measurement='lines', cmap='Reds')
#exponential_kamb is the default method
ax3.set_title('with kamb density contours', y=1.05, fontsize=15)
fig.colorbar(m)


# Plot these things on the two stereonets
for ax in [ax1, ax3]:
    ax.grid()
    ax.set_azimuth_ticks([]) #This is to hide the azimuth labels

for ax in [ax1]:
    note = f"n={Plunge.size} \nMean Plunge: {Plunge.mean():.1f}"
    ax.annotate(note, xy=(5*60, -30), xycoords='axes points')

plt.show()
#fig.savefig(f'Stereonets_Rose_{filelist[index]}.svg', bbox_inches = 'tight', format='svg')
pp.savefig(fig)
```

## 3.0 Orientation tensors

In [ ]:
```
#Calculate direction cosines...
def get_dir_cosines(Trend, Plunge):
    a=np.cos(Trend*np.pi/180)
    b=np.cos(Plunge*np.pi/180)
    c=np.sin(Trend*np.pi/180)
    xi=(a*b).round(4) #first direction cosines.
    yi=(c*b).round(4) #second direction cosines
    zi=np.sin(Plunge*np.pi/180).round(4) #third direction cosines
    return xi, yi, zi

X=np.concatenate(get_dir_cosines(Trend, Plunge)).reshape(3,Trend.shape[0])
#Brings the three direction cosines (xi, yi, zi) together in a single 3XN array/matrix
#(N=nb# of measurements)
```

In [ ]:
```
XT=X.T              #Transpose matrix X
print(XT)
```

In [ ]:
```
A=np.dot(X,XT).round(4)    #3X3 matrix of the sums of cross products of the direction cosines
print(A)
```

In [ ]:
```
#Get the eigenvalues and eigenvectors using mplstereonet

plu, azi, vals = mplstereonet.eigenvectors(Plunge, Trend, measurement='lines')
#This returns 1-D arrays for plunge and azimuth (eigenvectors converted to spherical coordinates),
#and normalized eigenvalues
print(plu,azi,vals)
```

In [ ]:
```
#Extract the normalized eigenvalues
S1=vals[0].round(4)
S2=vals[1].round(4)
S3=vals[2].round(4)
print(S1,S2,S3)
#The eigenvalues are slightly different with mplstereonet than with Stereonet 11
```

In [ ]:
```
Ei=eigh(A)  #This returns a 1-D array (eigenvalues) and a 2-D array (eigenvectors)
```

In [ ]:
```
Eighv=Ei[0] #Extract the eigenvalues
print(Eighv)
```

In [ ]:
```
#The sum of eigenvalues equals to the nb# of measurements.
#Normalized eigenvalues (divided by number of measurements) sum to 1.

S1=Eighv[2]/Trend.shape
S2=Eighv[1]/Trend.shape
S3=Eighv[0]/Trend.shape
print(S1, S2, S3)
#normalized eigenvalues; the values obtained with eigh are the same as those obtained using Stereonet 11
```

In [ ]:
```
#Make a biplot of S3 and S1

fig = plt.figure(figsize=(10,8))
ax = fig.add_subplot(1,1,1) # row-col-num

# Hide the right and top lines of the default box
ax.spines['right'].set_visible(False)
ax.spines['top'].set_visible(False)

#ax.set_xlim((0.4, 1.0,))
#ax.set_ylim((0.0, 0.3))
```

```
xticks = np.arange(0.4, 1.0, 0.1).round(2)
yticks = np.arange(0.0, 0.3, 0.05).round(2)

xtickLocations=np.arange(0.4, 1.0, 0.1).round(2)
yticklocations=np.arange(0.0, 0.3, 0.05).round(2)


ax.scatter(S1,S3, c='green', s=100)
ax.set_xlabel('S1', fontsize=18)
ax.set_ylabel('S3', fontsize=18)
ax.set_xticks(ticks=xtickLocations)
ax.set_yticks(ticks=yticklocations)
ax.set_xticklabels(xticks, fontsize=16)
ax.set_yticklabels(yticks, fontsize=16)

ax.grid(True, linestyle='--')
plt.show()
#fig.savefig(f'S3_S1plot_{filelist[index]}.svg', bbox_inches = 'tight', format='svg')
pp.savefig(fig)
```

In [ ]:
```
#Extract V1, V2, and V3

V1_azi=azi[0].round(1)
V1_plunge=plu[0].round(1)
V2_azi=azi[1].round(1)
V2_plunge=plu[1].round(1)
V3_azi=azi[2].round(1)
V3_plunge=plu[2].round(1)
print("V1 is", V1_plunge, "\u2192", V1_azi)
print("V2 is", V2_plunge, "\u2192", V2_azi)
print("V3 is", V3_plunge, "\u2192", V3_azi)
```

In [ ]:
```
E=(1-(S2/S1)).round(4)     #Elongation index
```

In [ ]:
```
I=(S3/S1).round(4)        #Isotropy index
```

In [ ]:
```
R=(1-(E+I)).round(4)    #A residual value to allow plotting the indices correctly on a ternary diagram
```

In [ ]:
```
df=pd.DataFrame(columns=['V1_trend', 'V1_plunge', 'E','I', 'R'])
```

In [ ]:
```
df.loc[0]=[V1_azi, V1_plunge, E,I,R]
df
```

In [ ]:
```
df["E"]=df['E'].astype('float')      #To specify the Dtype is 'float'
df["I"]=df['I'].astype('float')
df["R"]=df['R'].astype('float')
df.dtypes
```

In [ ]:
```
df.info()
```

In [ ]:
```
df
```

In [ ]:
```
df.to_csv(f'{filelist[index][:-4]}_Data_Output.csv', index=False)
```

In [ ]:
```
#Let's plot the results on a ternary diagram!

scale = 1.0
figure, fabric = te.figure(scale=scale)
figure.set_size_inches(12,10)

#PLot the data
fabric.scatter(df[['E','I','R']].values, marker='D', color='green', label="Green Diamonds")

# Draw Boundary and Gridlines
fabric.boundary(linewidth=2.0)
fabric.gridlines(color="blue", multiple=0.2)

# Set Axis labels
fontsize = 12
offset = 0.2
fabric.left_axis_label("I=S3/S1", fontsize=fontsize, offset=0.2)
fabric.right_axis_label("E=1-(S2/S1)", fontsize=fontsize, offset=0.2)
fabric.top_corner_label("Isotropic", fontsize=fontsize, offset=0.25)
fabric.right_corner_label("Cluster", fontsize=fontsize, offset=-0.05)
fabric.left_corner_label("Girdle", fontsize=fontsize, offset=-0.05)

#This is to configure the style of the axes and ticks and specify their orientation/sense
fabric.ticks(axis='lbr', multiple=0.2, linewidth=1, offset=0.025, tick_formats="%.1f", clockwise=True)
fabric.get_axes().axis('off')
fabric.clear_matplotlib_ticks()

fabric.show()
#fabric.savefig(f'Ternary_Diagram_{filelist[index]}.svg', bbox_inches = 'tight', format='svg')
pp.savefig(figure)
```

In [ ]:
```
#Now V1 can be added to the data points on the stereonet

fig = plt.figure(figsize=(8,8))
ax = fig.add_subplot(111, projection='stereonet')
ax.line(Plunge, Trend, 'o', color='blue', label='a-axis')
m=ax.density_contourf(Plunge, Trend, measurement='lines', cmap='Reds') #exponential_kamb is the default method
fig.colorbar(m)
plunge=V1_plunge
bearing=V1_azi
ax.line(plunge, bearing, 'X', color='green', markersize=12, label="V1")
ax.set_title(f'{filelist[index][:-4]} a-axis with V1 and kamb density contours', y=1.10, fontsize=15)

#Another approach to avoid repetition of labels in the legend:
from collections import OrderedDict

handles, labels = ax.get_legend_handles_labels()
by_label = OrderedDict(zip(labels, handles))

#This is to display the legend in the upper right corner without overlapping the stereonet, no duplicates
ax.legend(by_label.values(), by_label.keys(), loc='upper right', bbox_to_anchor=(1.05, 1.1), fontsize=14)

#Add some notes and values beside the plot
note = f"n={Plunge.size} \nS1={S1} \nV1 azimuth={V1_azi}"
ax.annotate(note, xy=(5*0, -30), xycoords='axes points',fontsize=15)

ax.grid()
ax.set_azimuth_ticks([])
plt.show()
#fig.savefig(f'Stereonet_w_V1_{filelist[index]}.svg', bbox_inches = 'tight', format='svg')
pp.savefig(fig)
```

In [ ]:
```
pp.close()
```